Advances and Applications in High-Definition Simulation of Packed Bed Liquid Chromatography

Weiterentwicklung und Anwendungen der Hochauflösenden Simulation der Festbett-Flüssigchromatographie

Von der Fakultät für Maschinenwesen der Rheinisch-Westfälischen Technischen Hochschule Aachen zur Erlangung des akademischen Grades eines Doktors der Ingenieurwissenschaften genehmigte Dissertation

vorgelegt von

Jayghosh Subodh Rao

Berichter: Universitätsprofessor Marek Behr, Ph. D.
Honorarprofessor Dr.-Ing. Eric von Lieres und Wilkau

Tag der mündlichen Prüfung: 15. September 2025

Acknowledgements

First and foremost, I would like to express my deepest gratitude to my supervisors, Hon.-Prof. Dr.-Ing. Eric von Lieres und Wilkau, and Univ.-Prof. Dr. Marek Behr, Ph.D. Their guidance, invaluable advice, and patience have been instrumental throughout my doctoral journey. Special thanks go to Prof. Dr. Wolfgang Wiechert for reviewing the project on a quarterly basis.

I would also like to extend my heartfelt thanks to the teams at both CATS and ModSim. Working alongside so many dedicated and talented colleagues has been an irreplaceable source of inspiration and motivation. Special thanks to Dr. Martin Beyss, who, in addition to his research duties, excellently and reliably maintained the workstation cluster at ModSim, which has been absolutely crucial for this work.

My sincere thanks go to Xiang Xu, for her support and excellent work as my Master's student. I have no doubt that the project is in good hands now that she has taken up the mantle.

I would like to thank the VSR Committee for their yearly reviews and generous allocation of compute resources, which were critical to the success of this work. I am also grateful to the Jülich Supercomputing Centre for providing access to the JURECA supercomputer and for their continued efforts in maintaining a reliable and high-performance computing environment.

A special thanks to my mother, who has always, at every step, sacrificed so much of her life for my betterment. Thanks are also due to my in-laws, who held me accountable in the final years of the project.

Finally, I owe my deepest gratitude to my wonderful wife. Without her unwavering patience, understanding, and immense support, this journey would not have been possible.

Kurzfassung

In dieser Dissertation werden Fortschritte bei hochauflösenden (engl. high definition, HD) Simulationsmethoden für die Festbettchromatographie vorgestellt. Dabei liegen die Schwerpunkte auf der Simulationsgenauigkeit, effizienten Workflows und der Anwendbarkeit zur Kalibrierung von Modellen mit reduzierter Ordnung (engl. reduced order models, ROMs). Ein umfassendes Framework wird vorgestellt, das die Simulationsgüte durch gezielte Verbesserungen bei der Geometriedarstellung, der Gittergenerierung und der numerischen Stabilisierung erhöht. Es wurden lokale und globale Strategien für die Kontaktpunktmodellierung untersucht, wobei sich zeigte, dass eine geringfügige globale Reduktion der Partikelgröße den besten Kompromiss zwischen erfolgreicher Gittergenerierung und Verlässlichkeit der Simulationen bot. Ein neuartiges Verfahren zur Gittergenerierung, das die geometrische Ähnlichkeit zwischen den Partikeln nutzt, führte zu einer Beschleunigung um den Faktor 10 im Vergleich zu allgemeinen Verfahren. Eine neue Stabilisierungsmethode, die auf dem kontravarianten metrischen Tensor basiert, wurde angewendet, um den relativen Holdup-Volumenfehler um bis zu den Faktor drei zu reduzieren. Die anisotrope Gitterverfeinerung in der Nähe von Partikel- und Wandgrenzflächen führte zu einer erheblichen Verringerung der Elementanzahl bei gleichbleibender oder verbesserter Genauigkeit.

Ein wesentlicher Beitrag dieser Arbeit besteht in der Entwicklung und Anwendung eines Kalibrierungsworkflows für ROMs, insbesondere für allgemeine 1D- und 2D-Ratenmodelle. HD-Simulationsdaten für dünne Säulen wurden räumlich gemittelt und zur Bestimmung von Dispersions- und Stoffübergangskoeffizienten verwendet. Die Ergebnisse zeigen hervorragende Anpassungen für polydisperse Packungen, während Diskrepanzen bei monodispersen Packungen die Grenzen der ROM-Annahmen bei ausgeprägten geometrischen Wandeffekten aufzeigen. Die Ergebnisse verdeutlichen die Notwendigkeit der Verwendung interner Zustandsvariablen wie Massenverteilungen der gelösten Stoffe für eine robuste Parameterschätzung, insbesondere in Modellen mit radialer Auflösung der Säule. Damit wird eine Grundlage für die ROM-Kalibrierung mit hochauflösenden Simulationen für verschiedene Geometrien geschaffen.

Die Simulationsinfrastruktur wurde erweitert, um lateral periodische (unbegrenzte) Geometrien zu unterstützen, mit neuen Vernetzungsmöglichkeiten und Aktualisierungen der Codebasis des numerischen Solvers, XNS. Vorläufige Ergebnisse aus periodischen HD-Simulationen zeigen, dass es keine Artefakte durch Wandeffekte gibt. Es wurde jedoch beobachtet, dass die Partikelbeladung aufgrund lokaler Nichtlinearitäten in der Strömung und im Transport innerhalb des beobachteten Bereichs asymmetrisch ist. Während die vollständige Implementierung doppelt-periodischer Randbedingungen noch nicht abgeschlossen ist, weist das aktuelle System das Potenzial auf, die Lücke zwischen HD-Modellen und ROM für realistische, große chromatographische Systeme zu schließen. Diese Arbeit legt den Grundstein für zukünftige Bemühungen, Dispersionsphänomene mittels kalibrierter ROMs und skalierbarer HD-Simulationen lateral begrenzter und unbegrenzter Säulen genau abzubilden.

Abstract

This dissertation presents advancements in high-definition (HD) simulation methods for packed-bed chromatography, focusing on simulation accuracy, workflow efficiency, and applicability to calibration of reduced-order models. Comprehensive updates to simulation infrastructure enhance simulation accuracy through targeted improvements in geometry representation, mesh generation, and numerical stabilization. Local and global strategies for contact-point modeling were explored, revealing that minimal global particle size reduction offered the best trade-off between mesh generation success and simulation reliability. A novel mesh generation technique leveraging geometric similarity among particles achieved an order-of-magnitude speedup with respect to generic techniques. A new stabilization method based on the contravariant metric tensor was applied to reduce relative holdup volume error by up to a factor of three. Anisotropic mesh refinement near particle and wall interfaces yielded significant reductions in element count while maintaining or improving accuracy.

A key contribution is the development and application of a calibration framework for reduced-order models (ROMs), specifically 1D and 2D general rate models. HD simulation data for thin columns were spatially averaged and used to estimate dispersion and mass transfer coefficients. Results demonstrate excellent fits for polydisperse packings, while discrepancies in monodisperse packings highlight the limitations of ROM assumptions under strong geometric wall effects. The framework underscores the necessity of using internal state variables such as solute mass distributions for robust parameter estimation, especially in models with radial resolution. This establishes a foundation for ROM calibration using high-resolution simulations across diverse geometries.

The simulation infrastructure was extended to support laterally periodic (unconfined) geometries, with new meshing capabilities and updates to the codebase of the numerical solver, XNS. Preliminary results from periodic HD simulations show a lack of wall-effect artifacts. However, particle loading was observed to be asymmetric owing to local nonlinearities in flow and transport within the interstitial domain. While full implementation of double-periodic boundary conditions remains ongoing, the current system demonstrates the potential to bridge the gap between HD and reduced-order modeling for realistic, large-scale chromatographic systems. This work lays the foundation for future efforts to accurately resolve dispersion phenomena via calibrated ROMs and scalable HD simulations of confined and unconfined columns.

Contents

List of Figures

List of Tables

List of publications

The work done during this project is published in the following journal articles. This dissertation reuses content from these articles for online publishing in the RWTH University Library as allowed by the Elsevier policy.

- Jayghosh Subodh Rao, Andreas Püttmann, Siarhei Khirevich, Ulrich Tallarek, Christophe Geuzaine, Marek Behr, and Eric von Lieres. 'High-definition simulation of packed-bed liquid chromatography'. In: *Computers & Chemical Engineering* 178 (2023). DOI: `https://doi.org/10.1016/j.compchemeng.2023.108355`

Contributions include scaling up HD geometry, contact-point handling, mesh generation, solver code development, improved finite element stabilization, performing simulations, visualization, analysis, calibration of 1D general rate model, and writing.

- Jayghosh Subodh Rao, Samuel Leweke, Jan Michael Breuer, Stephan Menzel, Marek Behr, and Eric von Lieres. 'Two-dimensional general rate model with particle size distribution in CADET calibrated with high-definition CFD simulated intra-column data'. In: *Separation and Purification Technology* 379 (2025). DOI: `https://doi.org/10.1016/j.seppur.2025.134409`

Contributions include development of novel multi-objective calibration workflow based on solute masses in each phase, calibration tool development, generation and preparation of high-definition reference data, performing calibrations, visualization, analysis, and writing.

Software publications

- Jayghosh Rao. *cadet/CADET-HD-pymesh: v1.0.0*. Version v1.0.0. June 2025. DOI: `10.5281/zenodo.15579995`
- Jayghosh Rao. *cadet/CADET-HD-chromoo: v1.0.0*. Version v1.0.0. June 2025. DOI: `10.5281/zenodo.15580015`
- Jayghosh Rao. *cadet/CADET-HD-paravision: v1.0.0*. Version v1.0.0. June 2025. DOI: `10.5281/zenodo.15580000`
- Jayghosh Rao. *cadet/CADET-HD-mixdtools: v1.0.0*. Version v1.0.0. June 2025. DOI: `10.5281/zenodo.15579993`
- Jayghosh Rao. *cadet/CADET-HD-genmesh: v1.0.0*. Version v1.0.0. June 2025. DOI: `10.5281/zenodo.15579985`
- Jayghosh Rao. *cadet/CADET-HD-scripts: v1.0.0*. Version v1.0.0. June 2025. DOI: `10.5281/zenodo.15580004`

Introduction 1

1.1 Chromatography

Chromatography is a process of separation of chemical components from mixtures and solutions. It is extensively used in the biotechnology, pharmaceutical, food, and forensic science industries amongst many others. The term encompasses several methods of separation with different fundamental principles, scales of application, and operating conditions, e.g., paper chromatography uses capillary action to move solvents up a paper strip, while membrane chromatography uses functionally active membranes to separate components from a solution flowing in a simple column. Nonetheless, these methods typically involve fluid flow, mass transport in and across multiple domains, and adsorption.

The most widely applied conventional form of chromatography is packed-bed column liquid chromatography, in which the solution (mobile phase) is pumped through a cylindrical column filled with a random close-packed bed of functionally active and porous spherical particles (stationary phase). The solution is advected through the complex and tortuous volumes that form the interstices of the packed-bed, allowing target components to diffuse into the particle pores through their surfaces, where they adsorb onto functionalized inner surfaces. Solution components can be selectively targeted based on the material and pore-structure properties of the stationary phase. This selective interactivity between the stationary phase and components in the mobile phase can be used to either modulate the residence times of such components, or completely filter them out of the input solutions based on their adsorption strengths, local concentrations, and other environmental factors such as temperature and pH. The desired ultimate effect is the separation of solute components at the column outlet in the form of distinct, non-overlapping bands that are separated in time. This is depicted in Figure 1.1.

The solute flux at the column outlet (chromatogram) is the primary measured output of the column. Apart from generally being used to visualize separation in experiments, chromatograms are extremely useful in characterizing the performance, efficiency, and adsorption capacity of a column. This is done using breakthrough experiments, where the column is continuously loaded with the solute until saturation, leading to the so-called breakthrough curve. Separation efficiency is affected by every aspect of the column, from macro- and micro-geometry of the stationary phase to the complex, competitive

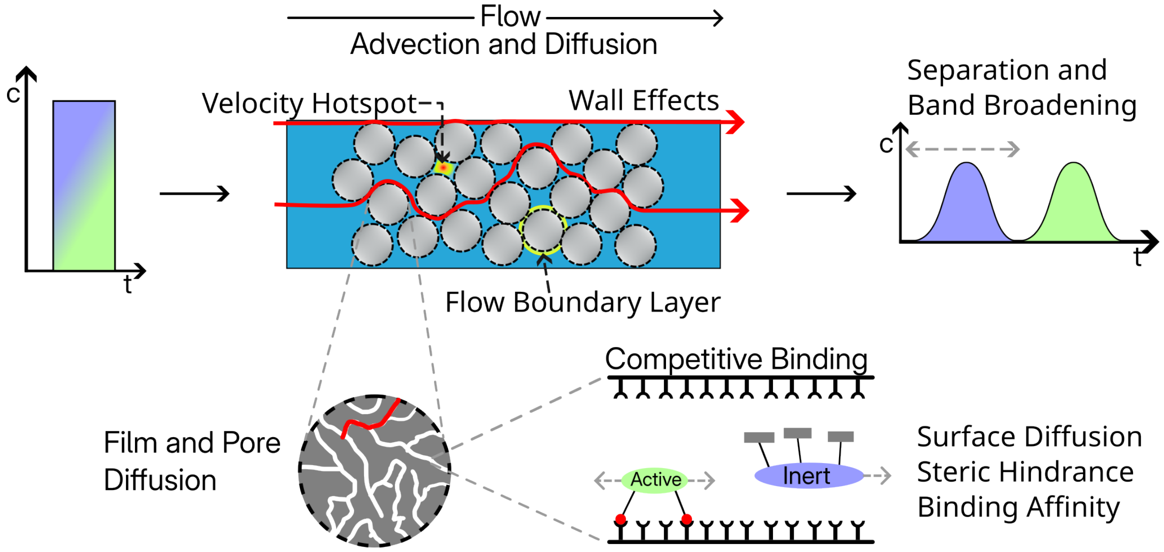

Figure 1.1: Illustration of transport and separation mechanisms in a packed-bed chromatography process.

mechanisms involved in multi-component adsorption. Column geometry and packed-bed morphology have a strong effect on flow in the interstitial region, thereby affecting solute transport and residence times. Dispersive phenomena within the interstitial region such as molecular diffusion, eddy dispersion, and turbulence degrade the resolution of components at the outlet by resulting in band-broadening. An illustration of this process is provided in Figure 1.2, which shows the broadening of an injected single-component pulse due to axial (and radial) dispersion. Channeling near walls (wall effects), caused by an increase in porosity at and near column walls due to geometric constraints, also leads to a loss in performance. This is especially significant in thin columns with larger particles. Band-broadening affects column performance adversely as wider component profiles at the column outlet lead to overlaps between components, resulting in insufficient resolution and ineffective separation. Thin-film boundary layers in the flow field at particle surfaces add to column dispersion and apply a resistance to mass transfer across the two regions. Adsorption mechanisms themselves can be complex, involving molecular attractions, bond formation, ion exchange, or other driving forces. Material properties of the stationary phase have a direct effect on adsorption behavior. In multi-component solutions, component-component interactions and competition at binding sites can additionally strongly affect adsorption performance.

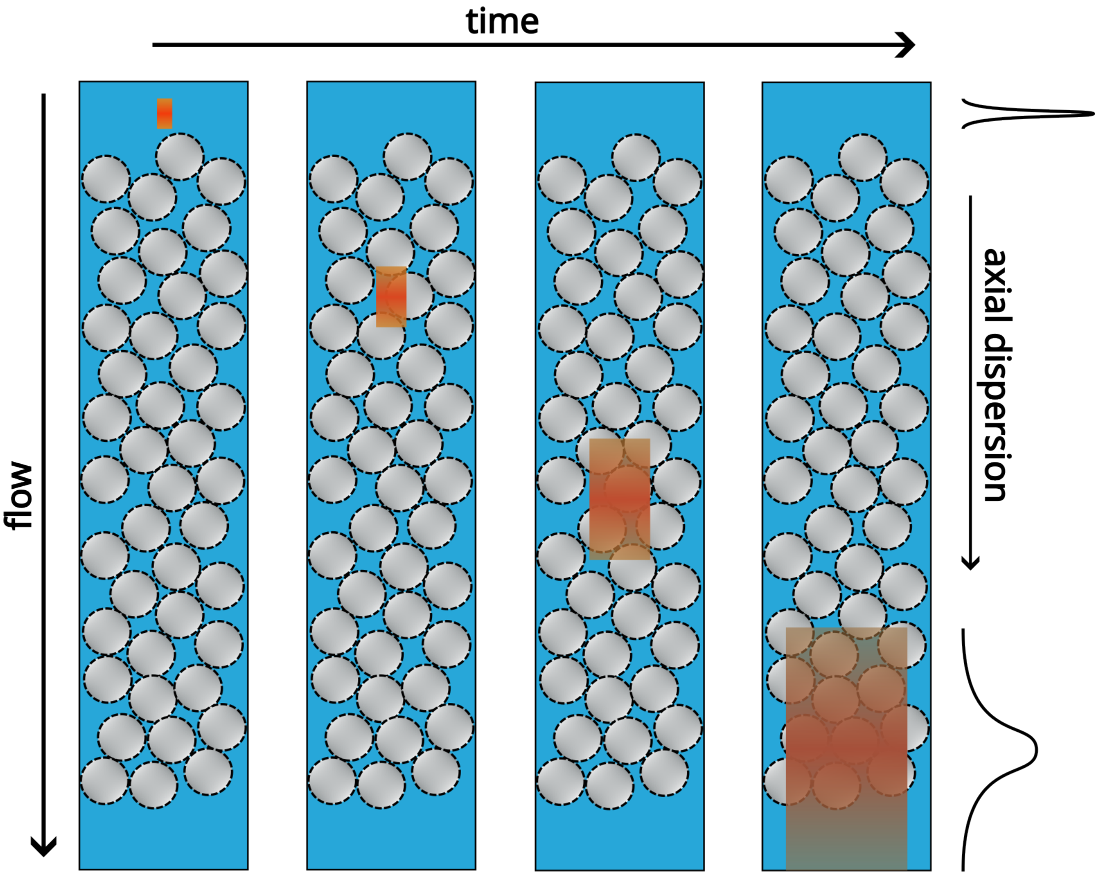

Figure 1.2: Illustration of band broadening of an injected pulse due to axial and radial dispersion in a packed-bed column over time.

1.2 Models of packed-bed chromatography

Numerical modeling and simulations can be beneficial in both analytical and preparative chromatography by providing insight into the complex interactions that take place within the column, improving performance, accelerating process design and optimization, and assisting in scale-up. Models can be constructed at different levels of fidelities with respect to column and bed geometry, flow, transport, and adsorption.

Reduced-order models

Conventional models of chromatography operate on assumptions of homogeneity in geometry, flow, and solute concentrations in the column. The interstitial region is modeled as a macroscopically continuous domain with uniform porosity, where solute concentrations are assumed to be constant across the cross-section area of the column. Particle loading is also assumed to be perfectly symmetric. These assumptions enable further simplification of the model via dimensionality reduction. The column itself is reduced to a one-dimensional entity, with model parameters varying only in the axial dimension. The particle domain is similarly reduced to a one-dimensional entity along its radius. Such models are henceforth referred to as reduced-order models (ROMs).

There exist several chromatography ROMs on a spectrum of complexity depending on their ability to model certain subprocesses to varying degrees. The most well-known of these are the Equilibrium Dispersive Model (EDM), Lumped Kinetic Model (LKM), and the General Rate Model (GRM)[9]. Their simplicity allows them to be solved extremely quickly, facilitating their use as unit operations in highly complicated process chart simulations and process sensitivity and optimization studies that require several evaluations of the process. However, the geometric simplification results in the need for explicit mathematical modeling of specific phenomena, resulting in the need for artificial parameters such as coefficients of axial dispersion and film-diffusion in order to capture missing dispersive and transport-related effects. These artificial parameters are required to be calibrated, typically using experimental data, in order to make the model useful. The calibrated values of these parameters are also tied to the geometry and operating conditions of the column, which leaves such a characterization of the column fragile. Furthermore, the homogenization enforces a lumping of subprocesses that result in similar effects, e.g., all dispersive effects from all sources are lumped together.

Two-dimensional reduced-order models

Two-dimensional ROMs model the column in the axial and radial dimensions, assuming homogeneity in only the angular dimension. This extension allows radially varying model parameters, consequently enabling the simulation of wall effects in thin columns. While it may seem like 2D ROMs are poised to dominate 1D ROMs due to this increased spatial dimensionality, the number of artificial parameters requiring calibration increases with the discretization in the radial dimension. Likewise, the resolution of the calibration reference data must correspondingly increase in dimensionality and resolution. While it is certainly possible to generate this data experimentally using techniques such as Confocal Laser Scanning Microscopy (CLSM), they impose restrictions on the stationary phase and solute materials, making it very restrictive and generally expensive.

High-definition models

In high-definition (HD) models, the column and the packed-bed macroscopic geometry is fully resolved in three dimensions; the interstitial domain is modeled in its entirety, while the intra-particle domain is modeled as a macroscopically continuous porous medium. Thus, the non-uniform and highly non-linear flow, dispersive phenomena due to wall effects and particle size distributions, and mass transfer resistances due to boundary layers are inherently captured physics-based principles without requiring explicit mathematical description. This geometric resolution enables detailed insight into column behaviors, especially within the interstitial domain.

The increased model fidelity results in increased numerical and developmental complexity that affects every stage of the simulation pipeline, from computational packing generation to visualization and post-processing. Scaling such models to realistic column sizes is extremely challenging, requiring technical expertise across several domains such as parallel computation, mesh partitioning algorithms, and numerical solvers and matrix preconditioning. In spite of these challenges, these models can be extremely useful in furthering knowledge and understanding of the chromatography process by providing high-quality data pertaining to the internal state of the column. Combined with non-invasive scanning techniques such as micro-CT, MRI [10], and CLSM [11–15], they have the potential to create accurate digital twins of the chromatography process. This is especially applicable to columns with 3D-printed substrates and monolithic stationary phases. Such techniques can also be used to validate simulation results for specific combinations of solutes, solvents, stationary phase, and container materials [16–23]. Furthermore, Spatially-resolved results of HD simulations can serve as high-dimensional sources of fixed parameters and reference data for ROM calibrations. This can be especially useful in calibrating 2D ROMs, which require radially-resolved profiles of interstitial velocity and reference data. While experimental chromatograms are typically used as such reference data, solute concentrations and masses within the column can be more potent in characterizing the entire column.

Existing work dealing with HD simulations in packed-bed columns focus on hydrodynamics in thin columns with short beds and are performed with commercial software such as ANSYS [24–26], COMSOL [27–30], and STAR-CCM+ [31–35]. The effect of column geometry [28, 32, 36], particle geometry [25, 37] and pore size [26] is explored.

While Jurtz et al. [38] and Dixon et al. [39] provide overviews of models and methods applied, they focus on gas-flow catalytic reactor systems. Among the few 3D simulations of chromatography in packed-bed columns in literature, Schnittert et. al. [27] extended the general rate model to 3D simulations of columns with up to 150 particles using COMSOL, and Gerontas et. al. [28] simulated Langmuir adsorption on a microfluidic column with 4700 particles.

1.3 Preliminary work

Previously, a stabilized Galerkin space-time finite element method was utilized by Andreas Püttman to solve the high-definition model of chromatography as detailed in his publication [40] and dissertation [41]. He implemented the HD Model in XNS, a massively-parallel multi-physics solver developed at the Chair for Computational Analysis of Technical Systems (CATS), RWTH Aachen University. The model comprises two coupled simulation stages: a steady-state laminar creeping flow simulation in the interstitial region is weakly coupled to a transient transport-adsorption simulation in the entire column. In his dissertation, Püttmann presented simulation results of his largest three-dimensional geometrical models containing 7861 particles in a monodisperse packing, and 5482 particles in a polydisperse packing, successfully demonstrating wall effects in thin columns.

Although a significant feat at the time, these simulations exhibited substantial holdup volume errors of 74.1 % and 78.3 % respectively. While a mechanism to correct the errors was developed, it could only be applied to the column breakthrough curve as a whole, without accounting for the distribution of the error in space within the column. A discussion regarding the side-effects of such a correction was also lacking. Furthermore, particle sizes were globally reduced by 2 % due to complications in mesh generation at point contacts between rigid spherical particles. The effective bed volume was, as a result, reduced by 5.8808 % with respect to the ideal geometry. Calibrations of 1D GRM with respect to the corrected chromatograms were based on fitting only the axial dispersion coefficient assuming the film-diffusion coefficient to be ∞. Nevertheless, the work done by Püttmann in setting up the theoretical groundwork for HD models and implementing them has been foundational for the current work. His implementation of the chromatography problem module in XNS and some of the auxiliary tools built for the pre-processing stage of the simulation pipeline served as a starting point for this work.

1.4 Scope

This work aims to achieve a diverse set of goals, including effecting improvements in the accuracy of HD simulations, analysing results to achieve insights into simulation error and the process itself, calibrating 1D and 2D ROMs using HD simulation results as reference data, and laying the groundwork for simulating wider columns using periodic boundary conditions. These goals are separated into the following work packages with specific objectives.

HD simulations

The primary objectives of this work package are to investigate different techniques of contact-point modeling in order to reduce the deviation between ideal and simulated geometries, to analyze results and reduce simulation error, and to simulate larger columns with more than 10 000 particles. Additionally, the HD simulation infrastructure is to be updated for robustness and scalability.

ROM calibration

Existing strategies for ROM calibration involve using breakthrough curves or chromatograms as objectives with experimentally generated reference data. Such experimentally generated reference data is typically extremely difficult to obtain in a radially resolved manner as required by 2D ROMs. In this work package, a novel calibration strategy, applicable to both 1D and 2D ROMs, that uses the internal state of the column obtained from HD results is to be devised. The newly developed methodology is to be applied to monodisperse and polydisperse, 1D and 2D GRM configurations in order to gain insight into the effect of geometry on ROM parameters such as dispersion and film-diffusion coefficients.

Periodic boundary conditions

As HD simulations are restricted to relatively thinner and smaller columns due to them being computationally intensive, an alternative approach to simulate wider columns that do not exhibit wall effects is to be explored in this work package. The objectives of this work package are to update the existing workflow and tools to facilitate simulations of columns with periodic boundary conditions. This involves generating periodic packings and meshes, and implementing support for periodic simulations in XNS.

Modeling 2

2.1 Packed-bed chromatography column

The packed-bed chromatography column is schematically illustrated in Figure 2.1. The two domains available for flow, transport, and adsorption/desorption are the interstitial (bulk) domain Ω_1, and the intra-particle (particle) domain Ω_2. The inlet and outlet surfaces of the column are given as Γ_{in} and Γ_{out} respectively, with the container walls denoted as Γ_{wall}. Particle surfaces are denoted as $\Gamma_{\text{surf}} = \Omega_1 \cap \Omega_2$. Solute components within the columns can exist in three phases, the bulk phase (c^b) in Ω_1, and the particle pore (c^p) and solid (c^s) phases in Ω_2.

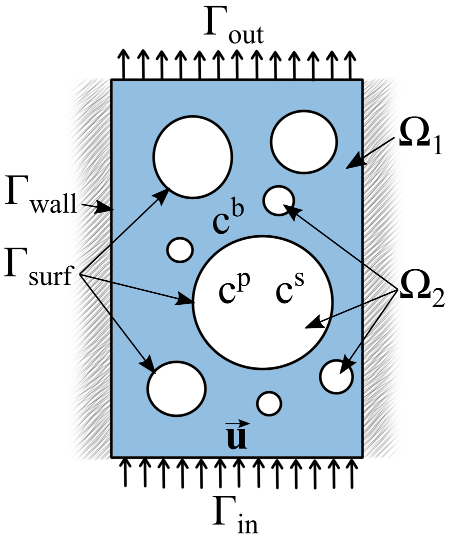

Figure 2.1: Schematic of domains and domain boundaries of HD chromatography model.

Particles in the packed-bed are randomly close-packed at the center of the column, with a regularity being imposed due to contact at the column walls. This regularity causes channels with porosity $\varepsilon_c = 1$, that fluctuates in a damped manner while approaching the average packing porosity at the center of the column. This is known as the geometric wall effect, and is significant in thin columns. While HD models inherently account for it and its consequent effects on velocity, 1D ROMs are not capable of resolving this effect, and 2D ROMs require manual input for radial variations in porosity and velocity.

HD simulations solve the interstitial flow field $\mathbf{u}$ in Ω_1, whereas in ROMs, it is typically prescribed as a scalar quantity estimated from a known flowrate and average porosity. Most models of chromatography assume advective-diffusive transport in Ω_1, and diffusive transport with adsorption/desorption in Ω_2. Flow at the inlet is considered to be fully developed, i.e., parabolic in profile, and the concentration of solute components injected are assumed to be uniform at the inlet. Flow of viscous fluid in Ω_1 around particle surfaces Γ_{surf} leads to the creation of boundary layers that create additional mass transfer resistance. This is modeled inherently in the flow simulations of the HD model, while requiring to be explicitly mathematically modeled in GRM.

Temperature effects and pH effects are conventionally neglected.

In the upcoming sections, the 1D and 2D general rate model (GRM), and the high-definition model (HDM) are discussed mathematically and in further detail. Next, basics of the finite element method are discussed and the weak forms of HD model equations are derived.

2.2 High-definition model of packed-bed chromatography

The prime feature of HD models is the spatially resolved column geometry, specifically in the bulk domain. While the increased dimensionality within the particles also enables mechanistic high-resolution views into the particle loading and unloading process, the particle domain is still modeled as a macroscopically homogeneous porous domain. In other words, the macro- and micro-pore channels and the complexity of the particle interior is not captured at the geometry level. The intra-particle porosity is taken into account mathematically in the pore- and solid-phase equations directly. This choice is deliberate, as column dispersion and film-diffusion phenomena that are the target of this study take place in the bulk domain. Resolution of the geometry in the bulk domain directly supports the resolution of the subprocesses in the bulk domain that contribute to, and are lumped into, column dispersion.

The bulk domain supports flow and interstitial transport, while the particle domain supports the solid-phase adsorption and transport in addition to pore-phase transport. Within the bulk domain, a Navier-Stokes flow field is solved, after which an advective-diffusive transport is set up and solved. In the models used in this work, a laminar creeping flow with extremely low Reynolds numbers along with constant solvent viscosity due to extremely low solute concentrations is assumed within the bulk domain. These assumptions enable further simplifications, namely, a stationary flow regime that need only be solved once. As per convention, small pore-sizes in the particle domain are assumed to typically preclude any fluid material flow, and transport in the particle domain is modeled as purely diffusive and without any advection. An arbitrarily complex adsorption/desorption mechanism is similarly modeled within the particle domain. In this work, the single component Langmuir adsorption model was used in all simulations with no reaction in either domain.

Fluid flow

In most liquid chromatography columns, viscous forces dominate over inertial forces. These cases where $Re < 1$ are categorized as 'creeping flow' and are modeled with the Stokes equations as:

$$-\mu\nabla^2\mathbf{u} + \nabla p = 0 \qquad \text{in } \Omega_1 \tag{2.1a}$$

$$\nabla \cdot \mathbf{u} = 0 \qquad \text{in } \Omega_1 \tag{2.1b}$$

where $\mathbf{u}$ is the flow velocity, p is the pressure, and μ is the viscosity. On the boundaries,

$$\mathbf{u} = 0 \qquad \text{on } \Gamma_{\text{wall}} \cup \Gamma_{\text{surf}} \tag{2.2a}$$

$$\mathbf{u} = u_z^{\text{in}} \qquad \text{on } \Gamma_{\text{in}} \tag{2.2b}$$

$$-p\mathbf{n} + \mu\mathbf{n} \cdot \left(\nabla\mathbf{u} + \nabla\mathbf{u}^T\right) = 0 \qquad \text{on } \Gamma_{\text{out}} \tag{2.2c}$$

where ρ is the density, Γ_{in}, Γ_{out}, Γ_{surf}, and Γ_{wall} are inlet, outlet, particle surface and column wall surfaces, respectively, u_z^{in} is the specified inlet velocity, and $\mathbf{n}$ is the outward normal vector at the column outlet.

Mass transport

In the multi-domain mass transfer simulations, diffusive flux continuity is used as surface coupling mechanism at the particle surfaces. In the bulk domain (Ω_1) the convection-diffusion problem is solved, and in the particle domain (Ω_2) the coupled diffusion-adsorption equations are solved. In the bulk region,

$$\frac{\partial c^b}{\partial t} + (\mathbf{u} \cdot \nabla)\, c^b = D_b \nabla^2 c^b \quad \text{in } \Omega_1 \tag{2.3}$$

where c^b is the concentration of the solute molecules in the bulk phase, and D_b is the free molecular diffusivity of the solute molecules. In the particle interior (Ω_2),

$$\varepsilon_p \frac{\partial c^p}{\partial t} + \left(1 - \varepsilon_p\right) \frac{\partial c^s}{\partial t} = D_p \varepsilon_p \nabla^2 c^p \quad \text{in } \Omega_2 \tag{2.4}$$

where c^p is the pore phase concentration, c^s is the solid phase concentration, D_p is the effective pore molecular diffusivity, and ε_p is the particle porosity. Adsorption and desorption is described by the single-component Langmuir model:

$$\frac{\partial c^s}{\partial t} - k_a c^p \left(c^s_{max} - c^s\right) + k_d c^s = 0 \quad \text{in } \Omega_2 \tag{2.5}$$

where k_a and k_d are the adsorption and desorption coefficients, and c^s_{max} is the maximum binding capacity.

The bulk concentration c^b is prescribed at the inlet (Γ_{in}). On the other column surfaces ($\Gamma_{out} \cup \Gamma_{wall}$), homogenous Neumann boundary condition is applied. Across particle surfaces (Γ_{surf}), for multi-domain coupling we have a flux continuity condition.

$$c^b = c^{\text{in}} \qquad \text{on } \Gamma_{in} \tag{2.6a}$$

$$\mathbf{n} \cdot \nabla c^b = 0 \qquad \text{on } \Gamma_{out} \cup \Gamma_{wall} \tag{2.6b}$$

$$\mathbf{n_1} \cdot \left(D_b \nabla c^b\right) = \mathbf{n_2} \cdot \left(D_p \varepsilon_p \nabla c^p\right) \qquad \text{on } \Gamma_{surf} \tag{2.6c}$$

The above flux continuity condition automatically ensures $c^b = c^p$ at the domain interface at all times $t > t_0$, provided that the computation is started with $c^b = c^p$ on Γ_{surf} at $t = t_0$.

Generalized holdup volume

The generalized holdup volume, V_H, of a column is the retention capacity of the column for a given sample. It will be used for measuring the accuracy of HD simulations in this work. The generalized holdup volume indicates the capacity available for sample molecules within the column. This includes the bulk volume, particle pore volume, and the volume of the sample that is adsorbed in a fully loaded column. While calculating the holdup volume for non-binding scenarios is simple, the generalized holdup volume depends on the binding mechanism and parameters. For the single component Langmuir model, it is possible to analytically calculate the generalized holdup volume as follows:

$$V_H^A = V_b + \varepsilon_p V_p + (1 - \varepsilon_p) V_p \frac{c^s_{\text{max}}}{c^b_{\text{in}}} \tag{2.7}$$

where

$$\frac{c^s_{\text{max}}}{c^b_{\text{in}}} = c^s_{\text{max}} \frac{k_a}{k_a c^b_{\text{in}} + k_d} \tag{2.8}$$

Here, V_b is the total volume of the bulk domain and V_p is the total volume of the particle domain.

The generalized holdup volume can also be numerically calculated for any fully developed breakthrough curve, i.e., when the column is fully saturated. The area between the normalized constant inlet concentration and the normalized breakthrough curve, shown in Figure 2.2, multiplied by the volumetric flow rate, $\dot{V} = \int_A u_z \, dA$, results in the numerical generalized holdup volume of the system:

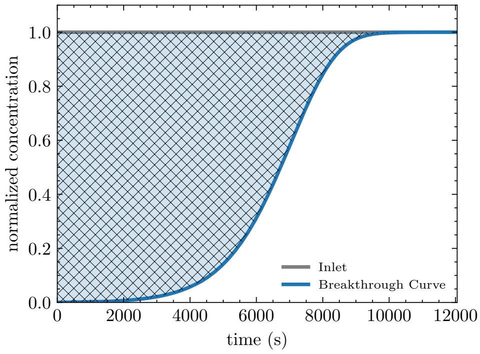

Figure 2.2: Generalized holdup volume as area over normalized chromatogram.

$$V_H^N = \dot{V} \int_0^\infty (1 - \frac{c_{\text{out}}^b}{c_{\text{in}}^b})\, dt \tag{2.9}$$

In HD simulations, the concentrations over cross sections A at the column inlet and outlet, respectively, are to be averaged. These averages are weighted by the velocity u_z:

$$c^{\text{avg}} = \frac{\int_A c u_z dA}{\int_A u_z dA} \tag{2.10}$$

With that, the numerical holdup volume becomes:

$$V_H^N = \dot{V} \int_0^\infty \left(1 - \frac{\int_A c_{out}^b \; u_{z,\text{out}} \; dA}{\int_A c_{\text{in}}^b \; u_{z,\text{in}} \; dA}\right) dt \tag{2.11}$$

The ratio of numerical to analytical holdup volumes ϱ is thus defined,

$$\varrho = \frac{V_H^N}{V_H^A} \tag{2.12}$$

The relative holdup volume error (ξ) is also defined as follows in order to quantify the error in the simulations performed in this work.

$$\xi = (\varrho - 1) \times 100\% \tag{2.13}$$

2.3 Reduced-order models of packed-bed chromatography

General rate model

Like most dimensionally reduced models, the general rate model holds two primary homogenizing assumptions:

1. the column is homogeneous in its cross section in terms of packing (porosity), flow, and transport.
2. bead loading is completely spherically symmetric.

The first assumption, which also implies that the column-to-particle diameter ratio, $\frac{d_c}{d_p} \gg 1$, allows the simplification of the model column geometry to an axially one-dimensional entity. The second enables the reduction of the individual particles into radially one-dimensional entities. Thus, the interstitial velocity u, and the average column porosity ε_c is scalarized for the entire column.

The generalized set of equations in the absence of reactions and assuming single bound state per component is given as

$$-\beta^b \frac{\partial c_i^b}{\partial t} - \beta^b u \frac{\partial c_i^b}{\partial z} + \beta^b D_{\mathrm{ax},i} \frac{\partial^2 c_i^b}{\partial z^2} - \beta^p j_{f,i} = 0, \qquad \text{in } \Omega_1 \tag{2.14a}$$

$$-\beta^p \frac{\partial c_i^p}{\partial t} + \beta^p D_{p,i} \left(\frac{\partial^2 c_i^p}{\partial r^2} + \frac{2}{r} \frac{\partial c_i^p}{\partial r} \right) - \beta^s j_{b,i} = 0 \qquad \text{in } \Omega_2 \tag{2.14b}$$

$$-\beta^s \frac{\partial c_i^s}{\partial t} + \beta^s D_{s,i} \left(\frac{\partial^2 c_i^s}{\partial r^2} + \frac{2}{r} \frac{\partial c_i^s}{\partial r} \right) + \beta^s j_{b,i} = 0 \qquad \text{in } \Omega_2 \tag{2.14c}$$

Here, the subscript $i = 1, \ldots, N_c$ indicates the component index, and will be dropped for readability. The phase ratios $\beta^b = \varepsilon_c$, $\beta^p = (1 - \varepsilon_c)\varepsilon_p$, and $\beta^s = (1 - \varepsilon_c)(1 - \varepsilon_p)$, where ε_c and ε_p are the column porosity and particle porosity respectively. D_{ax} is the axial dispersion coefficient, D_p is the particle pore diffusion coefficient, and D_s is the surface diffusion coefficient. $c^\kappa, \kappa \in \{b, p, s\}$ represents concentrations in the respective phases (bulk, particle pore, and solid).

The term j_f couples the concentrations between the bulk and particle pore phases at Γ_{surf},

$$j_{f,i} = \frac{1}{\varepsilon_p} \frac{3}{r_p} k_{f,i} \left(c_i^b - c_i^p(r = r_p) \right) \tag{2.15}$$

where r_p represents particle radius, and k_f the film-diffusion coefficient.

This set of equations can theoretically be combined with arbitrary binding models by defining j_b appropriately.

The resulting set of equations, in the absence of surface diffusion, simplifies to

$$\frac{\partial c_i^b}{\partial t} = -u \frac{\partial c_i^b}{\partial z} + D_{\text{ax},i} \frac{\partial^2 c_i^b}{\partial z^2} - \frac{1-\varepsilon_c}{\varepsilon_c} \frac{3}{r_p} k_{f,i} (c_i^b - c_i^p(r = r_p)) \qquad \text{in } \Omega_1 \tag{2.16a}$$

$$\frac{\partial c_i^p}{\partial t} = -\frac{1-\varepsilon_p}{\varepsilon_p} \frac{\partial c_i^s}{\partial t} + D_{p,i} \left(\frac{\partial^2 c_i^p}{\partial r^2} + \frac{2}{r} \frac{\partial c_i^p}{\partial r} \right) \qquad \text{in } \Omega_2 \tag{2.16b}$$

$$\frac{\partial c_i^s}{\partial t} = j_{b,i} \tag{2.16c}$$

This set of equations models mass transport within the column in a mechanistic manner by taking into account advection and dispersion in the bulk domain, and diffusion and adsorption in the particle domain. Thin film diffusive resistance is explicitly handled by the finite film diffusion coefficient k_f. In comparison to fully mechanistic models, however, GRM still lumps all sources of column dispersion into the axial dispersion coefficient (D_{ax}) attached to the diffusion operator. This leads to D_{ax} being orders of magnitude greater than the molecular diffusivity in the bulk phase D_b. The lumping is necessitated by the inability of ROMs to explicitly model different geometrical flow paths, the ultimate effects of which are taken into account by increasing the total effective diffusion within the bulk domain. Furthermore, this conventional set of equations is unable to model packed beds with particle size distributions, i.e., packing polydispersity, which is known to affect column dispersion.

Equation 2.16b relies on the premise that all solute molecules are infinitesimally small and capable of unrestricted access to all pores within the particle. It is also assumed that particles are perfect spheres with uniform material properties. Furthermore, it disregards the contribution of surface diffusion processes occurring within the solid phase, and considers only a single bound state of the solute molecule. While it is possible to explicitly model these subprocesses, they were ultimately not considered in the simulations undertaken for this work as they fell outside the scope of this research.

Danckwerts boundary conditions [42], Equation 2.17, are used at the column inlet and outlet.

$$-u\, c_i^b(z=0) + D_{\text{ax}} \frac{\partial c_i^b}{\partial z}(z=0) = -u\, c_{\text{in},i}^b \tag{2.17a}$$

$$\frac{\partial c_i^b}{\partial z}(z = L) = 0 \tag{2.17b}$$

Boundary conditions at the particle center and surface are given in Equation 2.18.

$$D_{p,i}\frac{\partial c_i^p}{\partial r}(r=0)=0 \quad \text{and} \quad D_{s,i}\frac{\partial c_i^s}{\partial r}(r=0)=0 \tag{2.18a}$$

$$\frac{3}{r_p}D_{p,i}\frac{\partial c_i^p}{\partial r}(r=r_p)=j_{f,i} \quad \text{and} \quad \frac{3}{r_p}D_{s,i}\frac{\partial c_i^s}{\partial r}(r=r_p)=0 \tag{2.18b}$$

Langmuir Adsorption

Adsorption models describe the process by which solute components either adsorb or desorb between the mobile phase c^p in the particle pores and the solid phase c^s on the functionalized inner surfaces of the particles. The simplest adsorption model assumes a linear relationship between the two quantities. The Langmuir adsorption model applies a saturation limit for the solid phase concentration, resulting in a behavior similar to linear models at low concentrations, and gradually approaching stagnation closer to the saturation limit or binding capacity c^s_{max}.

The multi-component Langmuir model makes the following assumptions:

- Adsorption affinity for a given component is uniform across the binding surface.
- Adsorption state is binary, solute molecules in the solid phase are considered bound, while those in the pore phase are considered unbound.
- Multiple components in the solute are inert with respect to each other.
- And, optionally, dynamic equilibrium exists between the two phases.

This results in the following set of equations describing the equilibrium for each component.

$$\frac{\partial c_i^s}{\partial t}=j_{b,i}=k_{a,i}c_i^p c^s_{max,i}\left(1-\sum_j^{N_c}\frac{c_j^s}{c^s_{max,j}}\right)-k_d^i c_i^s \quad \forall\, 1\leq i\leq N_c \tag{2.19}$$

where k_a and k_d are coefficients of adsorption and desorption respectively. For single component systems, the equation reduces to

$$\frac{\partial c^s}{\partial t}=k_a c^p\left(c^s_{max}-c^s\right)-k_d c^s \tag{2.20}$$

2D General rate model

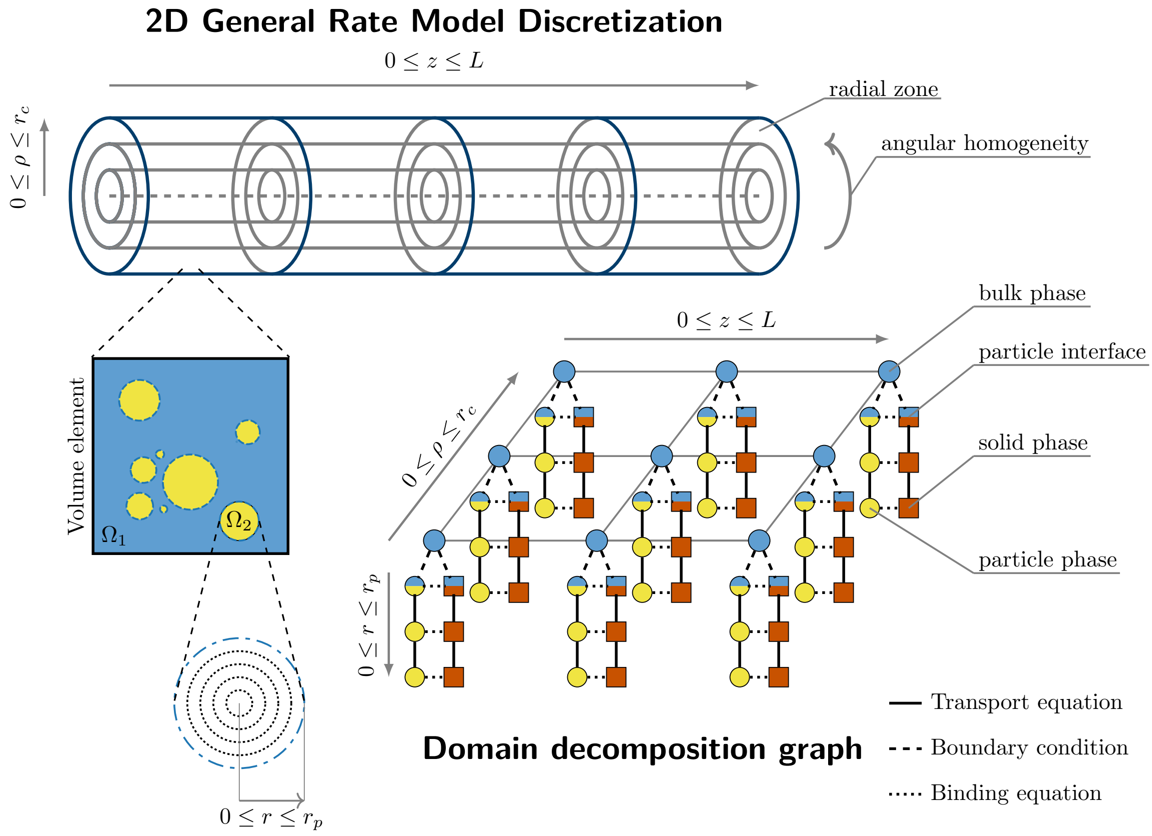

Figure 2.3: Discretization and domain decomposition representation for 2D GRM.

In 2D GRM, the homogeneity assumption in the bulk domain is relaxed to only the angular dimension, allowing parameters to vary in the radial column dimension, $\rho \in [0, r_c]$ where r_c is the column radius [43]. Thus, concentrations c^κ, particle volume fractions d_j, column porosity ε_c, flow velocity u, and the axial and radial dispersion coefficients $D_{\mathrm{ax},i}, D_{\rho,i}$ may depend on the radial coordinate.

The transport equation in the interstitial region becomes

$$\beta^b \frac{\partial c_i^b}{\partial t} = -\beta^b u \frac{\partial c_i^b}{\partial z} + \beta^b D_{\mathrm{ax},i} \frac{\partial^2 c_i^b}{\partial z^2} + \frac{1}{\rho} \frac{\partial}{\partial \rho} \left(D_{\rho,i} \rho \frac{\partial}{\partial \rho} \left(\beta^b c_i^b \right) \right) - \beta^p j_{f,i} \tag{2.21}$$

Furthermore, the inlet profile can also change in the radial direction due to the application of Danckwerts boundary conditions eq. (2.17) on the axial boundaries.

Additional boundary conditions at the column center and wall are:

$$\frac{\partial c_i^b}{\partial \rho}(\rho = 0) = 0 \tag{2.22a}$$

$$\frac{\partial c_i^b}{\partial \rho}(\rho = r_c) = 0 \tag{2.22b}$$

The model is visually represented with an equidistant radial discretization scheme and the domain decomposition graph in Figure 2.3.

Particle size distribution

Polydisperse packings can be modeled by ROMs by discretizing particle sizes into distinct groups or bins with a mean particle size $r_{p,j}$ and a volume fraction d_j, where $j = 1, \dots, N_p$ is the discrete particle type index, and $\sum_{j=1}^{N_p} d_j = 1$. These representative particle types are then instantiated in the model equations Equation 2.14b-Equation 2.14c, and Equation 2.15-Equation 2.18 with index j.

All particle-related parameters, including particle porosity ε_p, and the thin-film diffusion coefficient $k_{f,i}$ and binding parameters can depend on j.

The resulting transport equation becomes

$$\beta^b \frac{\partial c_i^b}{\partial t} = -\beta^b u \frac{\partial c_i^b}{\partial z} + \beta^b D_{\mathrm{ax},i} \frac{\partial^2 c_i^b}{\partial z^2} + \frac{1}{\rho} \frac{\partial}{\partial \rho} \left(D_{\rho,i} \rho \frac{\partial}{\partial \rho} \left(\beta^b c_i^b \right) \right) - \sum_{j=1}^{N_p} \beta_j^p d_j j_{f,i,j} \tag{2.23}$$

Numerical Methods 3

3.1 Finite element method

Fundamentals

Accurate resolution of the packed-bed and interstitial geometry is a necessity for the goals of this project. Hence, a numerical framework with support for boundary-conforming unstructured meshes is required. The finite element method (FEM), with its robustnuss, flexibility, and extensibility as a numerical framework was chosen for this work. It supports boundary-conforming unstructured meshes with higher-order interpolation functions within elements. Discontinuity in the solution can also be integrated into the framework.

FEM operates on the weak form of the partial differential equation, where regularity requirements on the solution are relaxed by the introduction of the so-called test (weighting) functions, followed by integration-by-parts. Thus, approximate solutions can be formulated in terms of linear combinations of piecewise polynomials or discontinuous functions, which allows for easier handling of problems with large gradients or shocks in the solution. This discretization is illustrated in Figure 3.1, where the true solution, u, is approximated by the discrete solution, u^h.

Consider the 1D model poisson problem in a bounded domain $\Omega \subset \mathbb{R}^d$ with a smooth boundary Γ.

$$\begin{aligned} -\nabla^2 u &= f, \quad \text{in } \Omega, \\ u &= 0, \quad \text{in } \Gamma. \end{aligned} \tag{3.1}$$

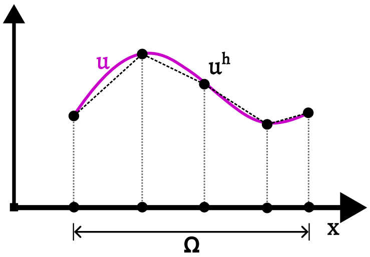

Figure 3.1: 1D representation of a solution u approximated by a discretized solution u^h in a bounded domain Ω. The solution is linearly interpolated within each element.

where $f \in L^2(\Omega)$. The weak form of the above PDE is obtained by multiplying with a test function w, and integrating the equation.

$$-\int_\Omega w\nabla^2 u \; d\Omega = \int_\Omega wf \; d\Omega, \tag{3.2a}$$

$$\int_\Omega \nabla w \cdot \nabla u d\Omega - \int_\Gamma w\nabla u \cdot \mathbf{n} d\Gamma = \int_\Omega wf \; d\Omega, \tag{3.2b}$$

where Gauss' divergence theorem is applied to obtain Equation 3.2b. In this case, since $u = 0$ on Γ, the boundary term is zero. Assuming dirichlet boundary conditions, the boundary term may also be removed by selecting such test functions that vanish at the boundaries, i.e., $w = 0$ on Γ. Thus,

$$\int_\Omega \nabla w \cdot \nabla u d\Omega = \int_\Omega wf \; d\Omega \quad \forall w \in H_0^1(\Omega) \tag{3.3}$$

The solution to Equation 3.1 can then be defined as $u \in H_0^1(\Omega)$ that satisfies the above expression, which can be generally expressed in its bilinear form as follows.

$$a(u, w) = l(w) \quad \forall w \in H_0^1(\Omega), \tag{3.4}$$

where $H_0^1 \subset H^1$ is the subspace of the Hilbert space H^1, that contains functions whose trace on Γ vanishes. Here, $l(w) = (f, w)_{0,\Omega}$ is assumed to be a continuous functional.

In fact, problems of this form that exist in the general Hilbert space H can be shown to have unique solutions $u \in H$ given the bilinear form $a(\cdot,\cdot)$ satisfies the conditions of boundedness (continuity) and coercivity defined as follows.

$$\begin{aligned} |a(u, w)| &\leq C \, \|u\|_H \, \|w\|_H \, , & \forall u, v \in H, \\ a(u, w) &\geq \alpha \, \|w\|^2 \, , & \forall w \in H. \end{aligned} \tag{3.5}$$

where $C > 0$ and $\alpha > 0$ are constants. This is proven by the Lax-Milgram lemma.

Using the Ritz-Galerkin method, the problem is projected into a finite-dimensional subspace, $S_h \subset H$ of the original Hilbert space, H. The problem then reduces to finding $u_h \in S_h$ such that

$$a(u_h, w_h) = l(w_h), \quad \forall w_h \in S_h \tag{3.6}$$

A set of basis functions that span the n-dimensional subspace S_h is constructed as $\{\phi_1, \ldots, \phi_n\}$. Thus, the solution in S_h can be represented as

$$u_h = \sum_{k=1}^{n} c_k \phi_k \tag{3.7}$$

The basis functions themselves can be applied as test functions w_h in the bilinear form, resulting in

$$\begin{aligned} a\left(u_h, \sum_{j=1}^{n} \phi_j\right) &= \sum_{j=1}^{n} l(\phi_j) \\ \sum_{j=1}^{n} a(u_h, \phi_j) &= \sum_{j=1}^{n} l(\phi_j) \\ \sum_{j=1}^{n} a\left(\sum_{k=1}^{n} c_k \phi_k, \phi_j\right) &= \sum_{j=1}^{n} l(\phi_j) \\ \sum_{j=1}^{n} \sum_{k=1}^{n} c_k a(\phi_k, \phi_j) &= \sum_{j=1}^{n} l(\phi_j) \end{aligned}$$

which is the linear system of equations for the unknown coefficients c_k,

$$\mathbf{A}\mathbf{x} = \mathbf{b}$$

In this work, nonlinear PDEs are linearized using a Newton-Raphson iteration. The Generalized Minimum Residual (GMRES) method [44, 45] is used to solve the linearized system of equations, which typically consists of a sparse, non-singular matrix $\mathbf{A}$ which may not be symmetric or positive definite. GMRES iteratively approximates the true solution $\mathbf{x}^* = \mathbf{A}^{-1}\mathbf{b}$ as

$$\mathbf{x}_m = \mathbf{x}_0 + \mathbf{z} \mid \mathbf{z} \in K^m(\mathbf{A}; \mathbf{r}_0) \tag{3.8}$$

where $\lim\limits_{m \to \dim(\mathbf{x})} \mathbf{x}_m = \mathbf{x}^*$, $\mathbf{r}_0 = \mathbf{A}\mathbf{x}_0 - \mathbf{b}$ is the initial residual for an initial guess $\mathbf{x}_0$, and $K^m(\mathbf{A}; \mathbf{v})$ is the m-dimensional Krylov subspace generated by $\mathbf{A}$ from $\mathbf{v}$.

$$K^m(\mathbf{A};\mathbf{v}) = \mathrm{span}\{\mathbf{v}, \mathbf{A}\mathbf{v}, \mathbf{A}^2\mathbf{v}, \dots, \mathbf{A}^{\mathbf{m-1}}\mathbf{v}\} \tag{3.9}$$

This is done by minimizing the residual $\|\mathbf{r}_m\| = \|\mathbf{b} - \mathbf{A}\mathbf{x}_m\|$ over $\mathbf{x}_m - \mathbf{x}_0 \in K^m(\mathbf{A};\mathbf{r}_0)$.

Fluid flow

The steady state Stokes flow equations defined in Equation 2.1 can be converted to their weak form as follows.

$$\begin{aligned} \int_{\Omega_1} \mathbf{w} \cdot (-\mu\nabla^2\mathbf{u} + \nabla p) &= \mathbf{0} \quad \text{in } \Omega_1, \\ \int_{\Omega_1} q(\nabla \cdot \mathbf{u}) &= \mathbf{0} \quad \text{in } \Omega_1 \end{aligned} \tag{3.10}$$

where $\mathbf{w} \in H^1(\Omega_1)$ and $q \in L^2(\Omega_1)$ are test functions for the velocity and pressure respectively. Integrating by parts,

$$\begin{aligned} -\mu\left(\int_{\Gamma} \nabla\mathbf{u} \cdot \mathbf{w}\, d\Gamma - \int_{\Omega_1} \nabla\mathbf{u} : \nabla\mathbf{w}\right) + \left(\int_{\Gamma} p\mathbf{w} \cdot \mathbf{n} d\Gamma - \int_{\Omega_1} p\nabla \cdot \mathbf{w}\right) &= \mathbf{0} \quad \text{in } \Omega_1, \\ \int_{\Omega_1} q(\nabla \cdot \mathbf{u}) &= \mathbf{0} \quad \text{in } \Omega_1 \end{aligned} \tag{3.11}$$

The boundary terms are nullified in the case of dirichlet boundary conditions, since the test functions are chosen such that $\mathbf{w} \in V := H^1_{\Gamma_D} = \left\{\mathbf{w} \in H^1 | \mathbf{w} = \mathbf{0} \text{ on } \Gamma_D\right\}$, where Γ_D is the part of the domain on which dirichlet conditions are applied. The solution space is similarly chosen such that $\mathbf{u} \in S := \left\{\mathbf{u} \in H^1 | \mathbf{u} = \mathbf{u}_D \text{ on } \Gamma_D\right\}$.

Linear shape functions are applied to both pressure and velocity, resulting in an equal-order approximation. This formulation does not satisfy the LBB compatibility condition, which guarantees well-posedness of the above problem. The LBB condition is instead sidestepped by applying Galerkin/least squares stabilization, resulting in the following discretized problem.

Find $(\mathbf{u}^h, p^h) \in S^h \times Q^h$ such that $\forall(\mathbf{w}^h, q^h) \in V^h \times Q^h$

$$\begin{aligned}\int_{\Omega_1} \mu \nabla \mathbf{u} : \nabla \mathbf{w} - \int_{\Omega_1} p \nabla \cdot \mathbf{w} + \sum_E \int_{Q_E^n} (-\nu \nabla^2 \mathbf{w}^h)\ \tau_E\ (-\nu \nabla^2 \mathbf{u}^h + \nabla p^h) = \mathbf{0} \quad \text{in } \Omega_1, \\ \int_{\Omega_1} q(\nabla \cdot \mathbf{u}) - \sum_E \int_{\Omega_E} (\nabla q^h)\ \tau_E\ (-\nu \nabla^2 \mathbf{u}^h + \nabla p^h) = \mathbf{0} \quad \text{in } \Omega_1\end{aligned} \tag{3.12}$$

The added stabilization terms are weighted residuals, thus ensuring that Equation 3.12 remains consistent with Equation 2.1. The second-order derivatives of $\mathbf{w}$ vanish due to the choice of linear elements, resulting in the problem reducing to

$$\begin{aligned}\int_{\Omega_1} \mu \nabla \mathbf{u} : \nabla \mathbf{w} - \int_{\Omega_1} p \nabla \cdot \mathbf{w} = \mathbf{0} \quad \text{in } \Omega_1, \\ \int_{\Omega_1} q(\nabla \cdot \mathbf{u}) - \sum_E \int_{\Omega_E} \nabla q^h\ \tau_E\ \nabla p^h = \mathbf{0} \quad \text{in } \Omega_1\end{aligned} \tag{3.13}$$

The stabilization parameter, τ_E is typically calculated exactly for 1D elements and extrapolated to 2D and 3D elements based on some metric of element length. In this work, it is calculated as described in the dissertation of Lutz Pauli [46], as $\tau_E = \tau_{\text{PSPG}} = \tau_{\text{MOM}}$, and

$$\tau_{\text{MOM}} = \min \left\{ \left(\mathbf{u}^h \cdot \mathbf{G} \mathbf{u}^h \right)^{-\frac{1}{2}}, \frac{C_M}{D_b \sqrt{\mathbf{G} : \mathbf{G}}} \right\} \tag{3.14}$$

where $\mathbf{G} = \left(\frac{\partial \xi}{\partial \mathbf{x}} \right)^T \mathbf{K} \left(\frac{\partial \xi}{\partial \mathbf{x}} \right)$ is the contravariant tensor, and $\left(\frac{\partial \xi}{\partial \mathbf{x}} \right)$ is the inverse jacobian of the element mapping between the reference space and the physical space. The matrix $\mathbf{K}$ is given for 3D cases as

$$\mathbf{K} = \frac{1}{2\sqrt[3]{2}} \begin{bmatrix} 3 & -1 & -1 \\ -1 & 3 & -1 \\ -1 & -1 & 3 \end{bmatrix} \tag{3.15}$$

$C_M = 0.0285$, and $\sqrt{\mathbf{G} : \mathbf{G}} = 2.2797 h^{-2}$ for tetrahedrons.

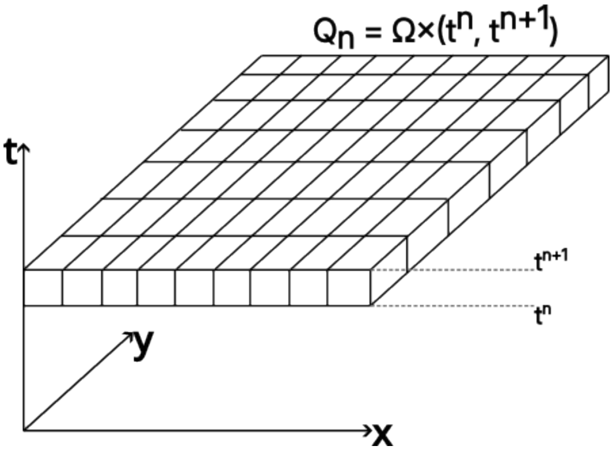

Figure 3.2: Illustration of a 2+1 dimensional discretized spacetime slab.

Mass transport and adsorption

The spacetime Galerkin approach with time-discontinuity is applied for solving the mass transport and adsorption equations. In contrast to traditional finite element methods that discretize only the spatial domain of the problem, spacetime methods treat the spatial and temporal domain jointly. This provides several advantages such as higher-order temporal accuracy and unconditional numerical stability. The application of discontinuity in time also improves the ability of capturing shocks, while reducing the total memory footprint of the simulation in practice. The space-time domain is divided into space-time slabs $Q_n = \Omega \times I^n$, where $I^n = (t^n, t^{n+1})$ represents an open time step interval with $t^{n+1} = t^n + \Delta t$. Piecewise linear discontinuous shape functions are used in the time direction across the space-time slab interfaces. This is illustrated in Figure 3.2.

Bulk domain, Ω_1

The advection-diffusion equation (Equation 2.3) may be ill-posed for large Peclet numbers $Pe = \frac{Lu_b}{D_b} \gg 1$ where advection dominates diffusion, thus requiring some form of added artificial stabilization. Considering the space-time slab $Q^n = \Omega_1 \times (t^n, t^{n+1})$ over the spatial domain Ω_1, the mass transport problem can be expressed as finding a discrete solution $c^{b,h} \in S_D^h$ that satisfies the weak form of Equation 2.3 for all discrete test functions $w^h \in S_0^h$. Note that while both the solution and test function spaces are subsets of the hilbert space H, they have differing boundary constraints. The solution space S_D^h must satisfy dirichlet boundary conditions, while the test function space S_0^h is designed to vanish at the boundaries.

$$\int_{Q^n} w(c^b_{,t} + (\mathbf{u}\cdot\nabla)c^b)dQ^n + \int_{Q^n} \nabla w \cdot D_b \nabla c^b\ dQ^n + \int_{\Omega_1} w^+(c^{b+} - c^{b-})d\Omega_1 = f^p_\Gamma \quad (3.16)$$

Here, the last term on the left hand side weakly enforces temporal continuity across space-time slab interfaces, with c^{b-} and c^{b+} representing solutions at the interface when approaching it from above and below respectively, $c^{b\pm} = c^b(t^n_\pm) = \lim \varepsilon \rightarrow 0^+ c^b(t^n \pm \varepsilon)$. The right hand side of the equation f^p_Γ couples c^b and c^p across particle surfaces Γ_{surf} for the given timestep Δt by ensuring continuity of fluxes.

$$f^p_\Gamma = \int_{\Gamma_{surf}\times\Delta t} w\mathbf{n}_2 \cdot (D_p \varepsilon_p \nabla c^p)dS \quad (3.17)$$

Equation 3.16 is stabilized using Galerkin/least squares stabilization which results in a weak formulation that is consistent with the strong form, i.e., any solution to the strong form is also a solution to the weak form.

$$\begin{aligned}\int_{Q^n} w(c^b_{,t} + (\mathbf{u}\cdot\nabla)c^b)dQ^n \quad &+ \quad \int_{Q^n} \nabla w \cdot D_b \nabla c^b\ dQ^n \\ + \quad \sum_E \int_{Q^n_E} (w_{,t} + (\mathbf{u}\cdot\nabla)w)\ \ \tau_E\ \ &(c^b_{,t} + (\mathbf{u}\cdot\nabla)c^b - D_b\nabla^2 c^b)dQ^n_E \\ &+ \quad \int_{\Omega_1} w^+(c^{b+} - c^{b-})d\Omega_1 \quad = \quad f^p_\Gamma \quad (3.18)\end{aligned}$$

The stabilization parameter is again selected from [46].

$$\tau_E = \tau^p_{\mathrm{CDR}} = \min\left\{\left(\left(\frac{2}{\Delta t}\right)^2 + \mathbf{u}^h \cdot \mathbf{G}\mathbf{u}^h\right)^{-\frac{1}{2}}, \frac{C_M}{D_b\sqrt{\mathbf{G}:\mathbf{G}}}\right\} \quad (3.19)$$

which is similar to τ_{MOM} in Equation 3.14, with an added term to account for timestep sizes.

Particle domain, Ω_2

Similarly, the diffusion-adsorption problem in the particle domain is a problem of finding $c^{p,h}, c^{s,h} \in S^h$ such that the following weak form of Equation 2.4 holds $\forall w^h \in S^h$ for the space-time slab $Q^n = \Omega_2 \times (t^n, t^{n+1})$

$$\begin{aligned}\int_{Q^n} w(\varepsilon_p c^p_{,t} + (1-\varepsilon_p)c^s_{,t})dQ^n \quad &+ \quad \int_{Q^n} \nabla w \cdot D_p \varepsilon_p \nabla c^p \; dQ^n \\ + \quad \int_{\Omega_2} w^+(c^{p+} - c^{p-})d\Omega_2 + \quad \int_{\Omega_2} w^+(c^{s+} - c^{s-})d\Omega_2 \quad &= \quad f^b_\Gamma \end{aligned} \tag{3.20}$$

Again, the right hand side f^b_Γ is formulated to enable flux continuity between concentrations c^b and c^p in Ω_1 and Ω_2 respectively.

$$f^b_\Gamma = \int_{\Gamma_{surf} \times \Delta t} w\mathbf{n}_1 \cdot (D_b \nabla c^b) dS \tag{3.21}$$

The multi-component langmuir adsorption in its weak form is given as follows.

$$\int_{Q^n} w \left(K c^s_{,t} - k_a c^p c^s_{max} \left(1 - \sum_{j=1}^{N} \frac{c^{s,j}}{c^{s,j}_{\max}} \right) + k_d c^s \right) dQ^n = 0 \tag{3.22}$$

Stabilization is not applied to the diffusion-adsorption equations in this work as test simulations for the parameters used in this work exhibited no spurious oscillations, with the problems being on the edge of reaction-dominance.

3.2 Conclusions

In this chapter, numerical methods used in this work are described and applied to model equations. Weak forms of model equations are derived with relevant stabilization terms.

High-definition simulation workflow 4

This chapter discusses the HD simulation workflow, and the specific tools and algorithms developed, implemented, and applied.

4.1 Overview

High-definition simulation of chromatography is challenging at several levels due to its increased model fidelity. The spatial resolution allows modeling highly non-linear flow and transport phenomena, but also multiplies computational complexity, with any increase in resolution causing a cubic increase in computational time. Consequently, HD models must necessarily be solved on massively-parallel solvers in order to allow scaling up the column geometry to a suitable level. The entire simulation pipeline from packing generation to the post-processing and visualization of results must be built in a robust, and parallel manner in order to efficiently utilize available resources and save time. Thus, developing, deploying, and maintaining these simulations and the surrounding infrastructure demands technical adeptness in addition to the theoretical and numerical expertise that is typically required in setting up simulation workflows.

The high-definition simulation workflow can be broadly subdivided into the following parts, resembling standard workflows for simulations.

- Pre-processing
    - Packing generation
    - Mesh generation
    - Mesh preparation
    - Mesh decomposition
- Solution
    - Solution of the steady-state flow stage
    - Mapping of flow field across meshes
    - Solution of the transport-adsorption stage
- Post-processing
    - Mesh and data conversion
    - Mesh and data visualization, reduction, and analysis

The workflow set up by Andreas Püttmann in his work was adopted and modified to suit the goals of this work. Several tools such as the mesh generation tool, `pymesh`, the mesh conversion tool, `mixd2pvtu`, and the post-processing and visualization toolkit, `paravision` were newly built during the course of this work. Bespoke intermediate tools and scripts were written to process and validate meshes and data in order to accommodate the specific requirements and capabilities in major steps of the workflow. Existing tools, such as `gmsh2mixd` were parallelized and updated to accomodate second-order shape functions in preparation for future work.

All the auxiliary tools used in this work can be found at the cadet github page, distributed into relevant repositories prefixed with 'CADET-HD'*. The solver XNS can be made freely available to collaborators upon request.

4.2 Column packing and computational packing generation

HD simulations of chromatography require the packed-bed geometry to be accurately resolved at a macroscopic level. Therefore, each particle must be fully specified in terms of its shape, size, and position in the bed in a manner that is geometrically consistent and non-overlapping.

The packed-bed geometry can be generated in two ways:

1. 3D scans of experimental columns, and
2. Computational generation of particle packings.

Imaging techniques such as Magnetic Resonance Imaging (MRI), Focused Ion Beam (FIB), and Confocal Laser Scanning Microscopy (CLSM) involve advanced imaging tools that demand significant investment in terms of cost, careful calibration, and post-processing effort. During the course of this work, several attempts were made at reconstruction of real packed beds from micro-CT scans provided by the team of Assoc. Prof. Rainer Hahn at BOKU University, Vienna, with the ultimate aim of studying packing defects. Some of the challenges faced in this endeavor include inadequate image resolution leading to insufficient distinction between particles, various image artefacts due to equipment vibration during scanning, and signal attenuation leading to a progressive loss in signal quality within the packed bed. These problems required additional equipment calibration, attenuation corrections, and denoising to improve the scanned images. Extracting the

---

* https://github.com/cadet?q=CADET-HD

complete packed bed geometry from the series of scanned images involves constructing a 3D image of the packed bed and fitting particles to the image.

A proof-of-concept for extracting spherical particle packing based on initial low-resolution scans set up by Dr. Jonas Bühler is shown in Figure 4.1. The series of 2D micro-CT scanned images of the column cross-section were filtered using Otsu's thresholding, and reconstructed into a 3D image. A cuboidal section of this image was extracted, onto which particles were superimposed manually, resulting in an overlapping set of particles that could serve as an initial state for a more sophisticated random close-packing algorithm.

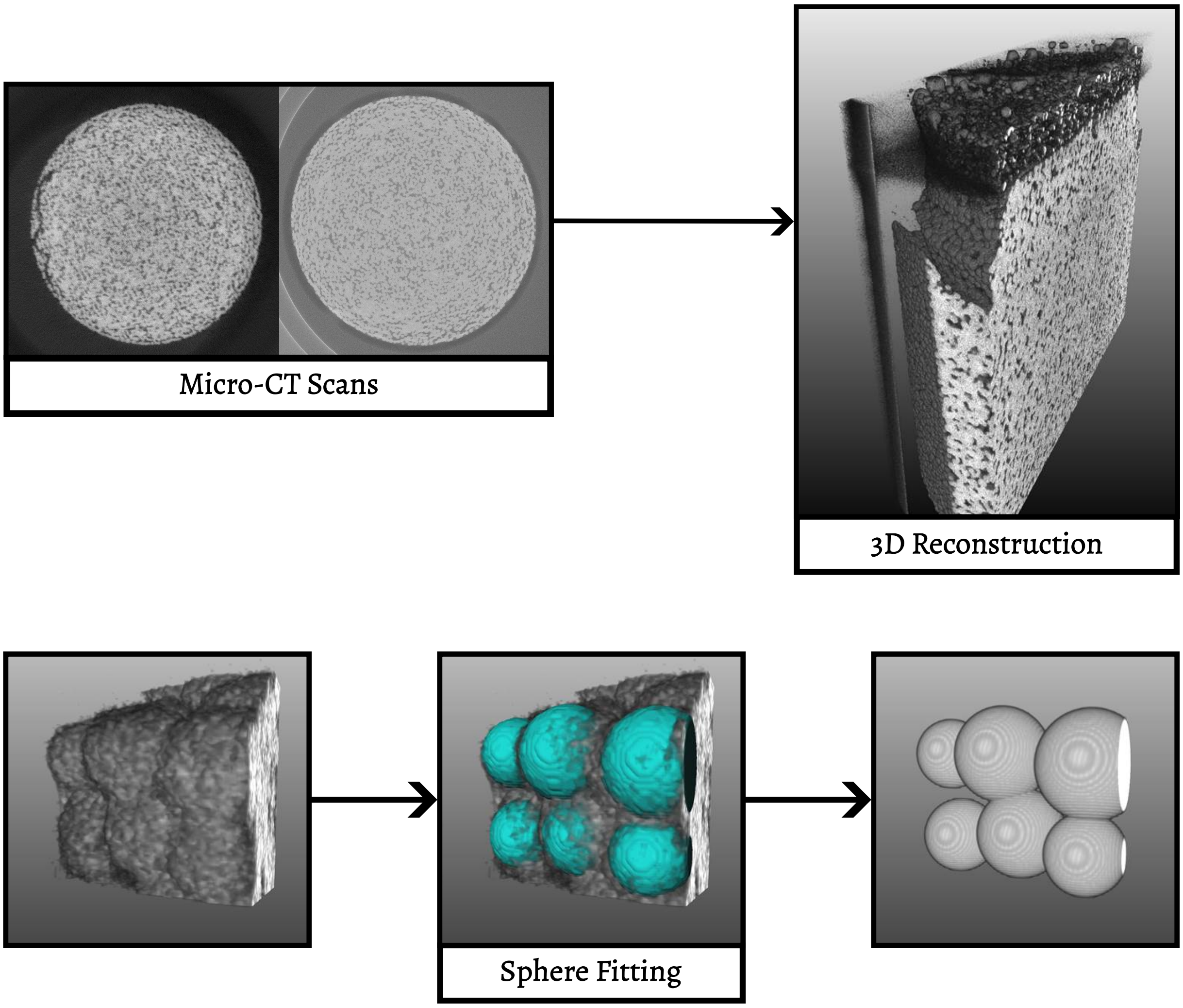

Figure 4.1: Illustration of extraction of particle positions and sizes from micro-CT scans. The 3D reconstruction shown above is longitudinally sliced and contains artifacts due to vibrations that occurred during the scan.

Numerically generated packings are more preferable in comparison due to their ease-of-use. Several algorithms with varying degrees of convergence rates, scalability, randomness, packing-densities, and time-to-completion exist for this purpose. They may be classified based on particle initialization, addition, and rearrangement as follows.

Sequential addition algorithms Particles are individually deposited onto the top of the packed bed [47–49].

Collective rearrangement algorithms Starting with an initial, overlapping, random packing, particles are repositioned or resized until the bed converges to a non-overlapping state [50–52].

Based on the fundamental mechanisms used in algorithms, they may also be classified as follows.

Physics-based algorithms rigid body dynamics, molecular dynamics, body forces, compaction, and shaking are simulated to generate packings [48, 50, 51, 53, 54].

Geometric algorithms Paricles are repositioned and resized based on rules and constraints derived from geometric properties of spheres, sphere contacts, and confinement region [52, 55–57] .

Optimization-based algorithms Optimization algorithms are applied to generate packings. [58–61]

Other methods Digitalization methods [62], . . .

A well-known geometric collective rearrangement algorithm, the Jodrey-Tory method [52] involves a random initialization of points that act as centers to inner and outer spheres within a given confinement. The inner diameter is calculated after each iteration as the minimum distance between any two points. The outer sphere is initially assigned an arbitrary diameter, which, over the course of the algorithm's iterations, converges to the inner diameter. During each iteration, the spheres with the worst overlaps are pushed apart until they no longer overlap. If overlaps with other neighbouring particles remain, the outer diameters are slightly reduced. The final packing density is influenced by the contraction rate of the outer diameter. A slower contraction rate is known to lead to a higher final packing density while also increasing execution time.

The initially proposed algorithm was defined for unconfined packings with periodic boundary conditions. A modified, parallelized form of the algorithm was used by the Tallarek Research Group at Phillips-University, Marburg, [63] to generate two large packings in cylindrical confinements: (a) a monodisperse packing with approximately 150,000 particles, and (b) a polydisperse packing with approximately 15,000 particles. The particle size distribution in the polydisperse packing was based on existing packings [64]. The packed-beds used in this work are cut sections of these larger packings.

4.3 Mesh generation

Mesh generation is a crucial step in the finite element method for solving partial differential equations, where the continuous problem domain is discretized into a set of interconnected elements. This involves mapping a set of nodes and conforming elements to the problem domain's geometry representation, and can be achieved through various techniques, including Delaunay triangulation, Voronoi diagram-based methods, and advanced algorithms such as mesh optimization and mesh adaptation. The quality and accuracy of the resulting solution depend heavily on the quality and refinement of the mesh. The goal of mesh generation is to create a mesh that accurately captures the complex geometrical features of the physical system, while also minimizing the number of elements required to achieve the desired level of accuracy.

Meshes can be categorized broadly into structured (quadrilateral and hexahedral elements), unstructured (triangular and tetrahedral elements), and hybrid. While structured elements result in more uniform meshes, they are difficult to apply to complex geometries, and typically involve tedious manual decomposition and mapping of the domain geometry. On the other hand, unstructured elements can be automatically applied to arbitrary domains quite easily. All the meshes generated in this work use linear tetrahedrons.

Contact point modeling

Packed-bed columns are notoriously challenging to mesh due to their complex geometry, which arises from the packing itself and affects the meshing process in two ways. Firstly, the random close-packing of particles of arbitrary shape and size creates several contact points between them. This requires the geometrical representations of the packed-bed to be extremely precise. Unfortunately, computationally generated random packings are not trivial to generate in such a precise manner. Furthermore, automatic meshing algorithms typically cannot handle such imprecise geometries at contact point regions, and require manual intervention to either adjust geometries or prescribe nodes at their positions. Secondly, the remaining interstitial domain is a complex geometry consisting of channels wiht highly irregular shapes and widths. The curved geometries necessitate smaller element sizes to conform to their shape, but this can lead to element distortion and degeneracy near the contact points in the interstitial domain. This leads to loss of accuracy and stability in the solution in those areas.

Several studies were conducted in attempts to mitigate these issues by side-stepping the problem of contact-points entirely. Commonly used methods employ techniques to modify the geometry in a pre-processing step that either remove the contact point entirely, or reshape it to a contact area instead. Broadly, they are classified into global or local methods, depending on whether these modifications are applied to all the particles globally, or if specific changes are applied directly at the individual contact points. The 4 most common methods of contact point modification are:

- Global reduction: Reduce size of all particles.
- Global expansion: Increase size of all particles.
- Local removal: Slice off material at contact points.
- Local addition: Add material (typically cylindrical bridges) at control points.

They are also visually depicted on two particles of different sizes in Figure 4.2. Global methods significantly modify packed-bed volumes, with a 2% reduction in volume leading to a 5.8% decrease in bed volume, and an expansion of similar magnitude resulting in a 6.1% increase in bed volume. In contrast, local methods are more favourable but require more effort to implement. Additive methods are generally more preferable as they do not alter local flow profiles as much, but they also increase complexity during generation due to added constraints and material, which can lead to poor scalability. However, it was observed in this work that a global reduction was the most practical solution when the reduction factor is low. The decoupling of individual particles enables shared-memory parallel mesh generation, as well as more advanced techniques such as copying meshes onto other particles.

Lastly, it is also possible to model the packed bed to be consisting of non-rigid bodies that experience minor deformation at contact points due to packing forces, converting all contact points into contact areas. Such an approach requires a static structural simulation to obtain the deformed mesh upon which the flow, transport, and adsorption equations would be solved. This is considered out of scope of the current work, but is nonetheless a valid approach to avoid singularities due to point contacts.

Mesh generation tools and procedures

GMSH is a widely-used open-source mesh generation tool distributed under the GPL2 license. It contains four modules: geometry kernel, mesh generator, solver, post-processor. Of these modules, only the first two are of interest in generating meshes for this project. The geometry kernel is used to create parameterized CAD (computer aided design)

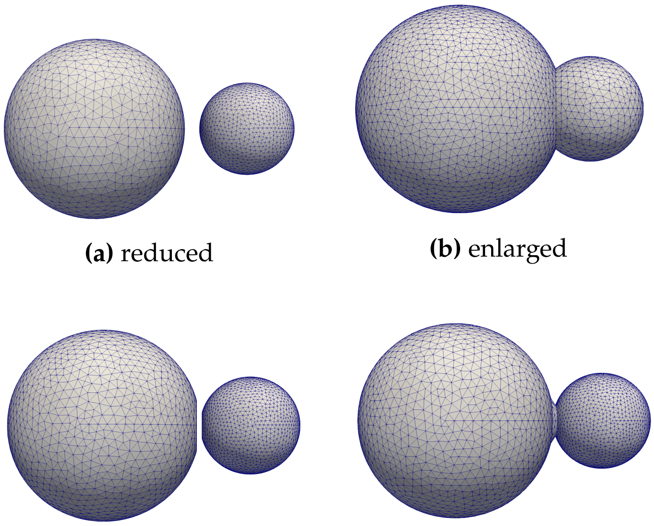

(a) reduced **(b)** enlarged

(c) capped **(d)** bridged

Figure 4.2: Contact point modifications illustrated using two particles.

representations of geometries that are then manipulated using boolean operations. GMSH uses Boundary Representation (B-Rep) to define geometrical entities, and provides some flexibility in terms of choosing the CAD geometry kernel: One may use the built-in kernel, or the OpenCascade OCCT toolkit. The two kernels differ slightly in the functions available to create and modify geometry. Geometrical entities can be constructed using either kernel via two approaches: (1) Bottom-up, where entities are defined in order of their dimensionality (points, curves, surfaces, and then volumes), and (2) Constructive Solid Geometry (CSG), where boolean operations are performed to produce final geometries.

Several mesh generation algorithms are available in GMSH. In order to guarantee conformity of meshes (non-overlapping elements), GMSH uses the bottom-up approach of meshing entities in order of their dimensionality. Element sizes can be constrained either uniformly on the whole model, or using size fields with appropriate attributes in specific regions. Finally, specific boundaries, interior surfaces, and volumes can be tagged such that boundary conditions and domain-specific equations can be solved in the later simulation step. Linear tetrahedral elements were used in all meshes in this project.

A modern packed-bed column mesh generation tool based on GMSH was developed for this project using GMSH's Python scripting interface. The code is freely available as an open-source software on GitHub at `https://github.com/modsim/ChromaHD-pymesh`. The software repository is structured as a core library with additional executable scripts that perform mesh generation and other related calculations on the packed-bed geometry and column mesh. The `pymesh` library builds on the the functions exposed in the GMSH Python API in order to generate meshes with the correctly defined volumes, surfaces, and physical groups that are necessary for the subsequent simulation steps. The generator script is invoked with the `mesh` command, and is configured via a yaml configuration file to handle settings such as particle modifications, container shape and parameters, mesh sizing information, and meshing algorithms. It also requires a binary-encoded file containing the 3D coordinates and diameters of individual particles that constitute the packed-bed.

A valid and suitable mesh can be generated via multiple methods that follow different sequences of operations on the provided geometries. In `pymesh`, two such methods are provided which can be configured using the `mesh_method` keyword in the input configuration file. The default `generic` method broadly performs the following operations:

- Load particle positions and sizes.
- Remove particles to adjust porosity if necessary.
- Apply contact-point modifications to packed-bed.
- Generate packed-bed geometry.
- Generate full container geometry.
- Perform boolean subtraction to generate column interstitial geometry.
- Separate and tag physical volumes and surfaces.
- Generate a mesh on the interstitial and packed-bed geometries.
- Write out mesh in the required format.

The fundamental concept underlying this approach is the creation of complex geometries through constructive solid geometry (CSG), followed by a direct volumetric mesh generation process. While this straightforward method exhibits robustness and versatility in generating meshes using any algorithm, it can become computationally demanding and time-consuming for larger, more intricate geometries.

The `copymesh` method was developed to speed up mesh generation for standard columns with confined packings. In this method, a reference particle is meshed volumetrically, and this reference mesh is then copied over to every particle in the packed-bed. In order to realize the efficiency improvement in practice, GMSH source code required patching to allow copying nodes and elements without automatically destroying and regenerating its internal mesh cache. This patch for the GMSH source code is provided with the `pymesh` source code in its repository.

The rough sequence of operations for the `copymesh` method is as follows:

- Load particle positions and sizes.
- Remove particles to adjust porosity if necessary.
- Apply contact-point modifications to packed-bed.

- Generate reference particle geometry and mesh.
- Copy reference particle mesh to all particles.
- Generate container surface geometry and mesh.
- Separate and tag physical volumes and surfaces.
- Generate a mesh in the remaining interstitial region.
- Write out mesh in the required format.

As the same reference mesh is applied to all elements, the mesh generation computation for the entire packed bed with n particles was replaced with that for a single particle followed by n copy operations. This method yielded 10× improvement in mesh generation speed with respect to the `generic` method, for columns with approximately 1000 particles.

In both methods, mesh size is scaled with respect to particle size such that a given mesh at a given element size conforms to all particles identically. Thus, all particles are captured equally well regardless of their diameter. Magnified views of monodisperse and polydisperse packings are shown in Figure 4.3.

`pymesh` can generate meshes with the bulk (Ω_1) and particle (Ω_2) domains either joined or disjoined at the interface $\Gamma_{surf} = \Omega_1 \cap \Omega_2$, enabling flexibility in the use of meshes depending on interface coupling and solution methods used in later stages of the workflow.

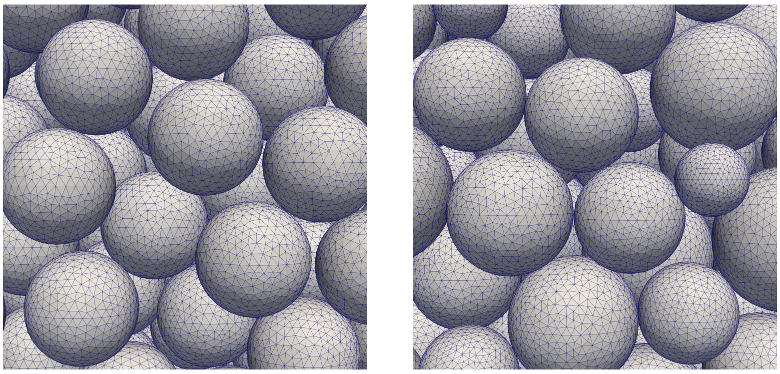

(a) monodisperse **(b)** polydisperse

Figure 4.3: Magnified views of meshes of monodisperse and polydisperse packings showing meshes scaled according to particle size.

Anisotropic meshes

It is possible in `pymesh` to prescribe anisotropy in mesh element sizes using the field mesh sizing feature of `GMSH`. Thus, element sizes can be refined in areas of high solution gradients, and coarser elements can be applied in other areas. Elements in the bulk domain, close to particle surfaces can be refined to capture the boundary layer, while those within the particles can be coarsened. Views of a test column with 4 particles in a cylindrical container with an anisotropic mesh applied are shown in Figure 4.4.

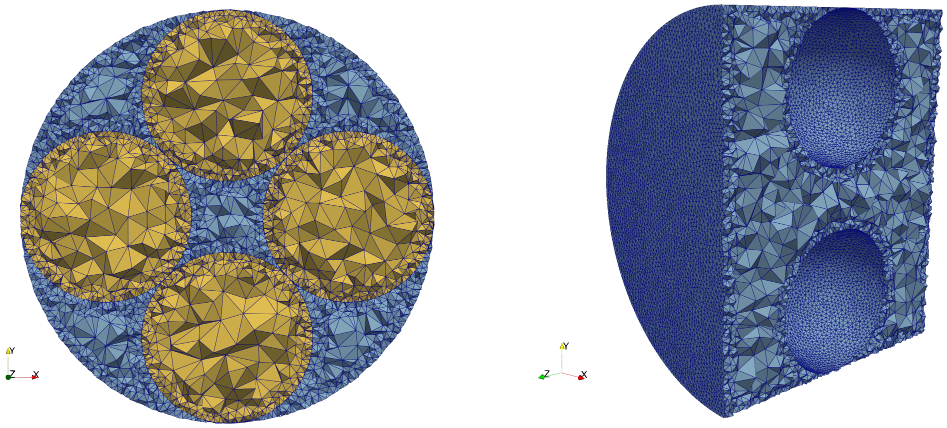

(a) Cross-section sliced view.

(b) Longitudinal clipped view.

Figure 4.4: Sliced and clipped views of an anisotropic mesh applied onto a toy geometry with 4 particles in a cylindrical confinement. This configuration ensures finer elements near particle surfaces and walls and coarser elements away from them.

Inlet splitting

`pymesh` also supports splitting container inlet walls to support the application of boundary conditions to only certain parts of the inlet. This is useful in realistically modeling sample injection, which is usually done only at the center of the column. An example is shown in Figure 4.5.

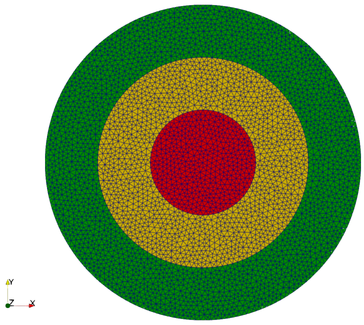

Figure 4.5: Illustration of a column inlet split into 3 concentric equidistant sections.

Periodicity

Generating periodic meshes on periodic packing geometries is also supported in `pymesh`. The algorithms applied to prepare packing geometries, generate periodic meshes, and validate resulting meshes are provided in chapter 8.

Local contact-point modification

Meshes used in preliminary investigations into the effect of various contact-point modeling methods were generated using `genmesh`, a predecessor to `pymesh`. It implements local contact-point modifications such as addition of cylindrical and conical bridges, and slicing off material at contact points, using boolean geometry operations. This, however, made local methods infeasible for large-scale geometries due to the increased computational requirements. Ultimately, this feature was not ported to `pymesh` due to the ease-of-use, performance benefits, and practicality of global size-reduction techniques.

4.4 Mesh preparation

The mesh generated in the previous step must be modified, and converted into the MIXD format that is used by `XNS`. The MIXD format stores mesh information and attached data across several separate serialized big-endian binary-encoded files, with the mesh metadata stored in an ASCII-encoded text file. Constituent files pertaining to a MIXD mesh are described in Table 4.1.

The `gmsh2mixdv2` utility is used to convert the mesh from the generated `msh2` format into a semi-discrete reference mesh in the MIXD format while splitting the mesh at the bulk-particle interface by doubling the nodes and elements on the packed-bed surface, Γ_{surf}. This enables modeling discontinuities in the solution at Γ_{surf}. This reference mesh is then used to generate the meshes used in the two solution stages.

The semi-discrete mesh of the bulk region, on which the flow equations are solved, is obtained by removing the elements of the particle domain using the `rmmat` utility. The space-time slab mesh of the entire column is obtained by duplicating the nodes and connectivity information from the reference mesh.

Table 4.1: Primarily used MIXD files

MIXD	Content
`minf`	A text file that contains information about the total number of nodes and elements in the mesh
`mxyz`	A file that stores the coordinates of each node in the mesh
`mien`	A regular mesh connectivity file, which records the global node numbers associated with each element in a specific order
`mrng`	A file that contains RNG or boundary information, specifying the boundary code for each element face, with multiple face entries per element
`mmat`	A file that defines volume domain identification using material IDs
`mprd`	A file that assigns each node either a corresponding partner node (for periodic boundaries) or its own ID if no partner exists
`mtbl`	A file that maps each node to its partner node (as mesh nodes at the particle surfaces are duplicated) or to its own ID if no partner exists

Mesh partitioning

While problems of moderate sizes can be simulated on a single workstation, large-scale problems require deployment on distributed compute clusters that may contain upto several thousands of processors, with each node equipped with a large amount of memory. Compared to the compute and memory limitations of individual workstations, clusters can perform computations in a massively parallel manner by dividing the problem in to chunks that can be locally solved with some communication across processes and threads. This scheme of parallelism demands minimal communication, and thus, latency, across processes in order to achieve a high degree of scalability. Such distributed finite element simulations require the meshes to be optimally partitioned into an appropriate number of chunks such that the communication across these partitions is minimized.

Mesh partitioning involves first generating an extended dual graph of its connectivity of constituent entities, with each element and node represented by vertices, and connections between them represented by edges. This graph is then decomposed in such a manner as to minimize the number of edges connecting individual partitions, while trying to ensure that the sizes of these partitions are similar to one another in order to optimally balance computational load. In this work, the `decompose` utility, that can interface with commonly used graph partitioning algorithms such as (Par)METIS [65] and (PT-)SCOTCH [66] is used. Depending on the size of the mesh, these tools might also need to be deployed in parallel and with support for 64 byte integers in order to avoid integer overflows.

In simulations with complex topological changes or mesh adaptivity, this step would be performed repeatedly during the simulation run. As mesh connectivity stays constant throughout the simulations in this work, this decomposition is only performed once for a given number of partitions.

4.5 Numerical simulation

The discretized system of equations corresponding to those shown in chapter 3 were previously implemented by Andreas Püttmann in XNS, a numerical simulation software developed at the Chair for Computational Analysis of Technical Systems (CATS), RWTH Aachen University. The heart of XNS is the GMRES solver that is applied to linearized matrix-vector equations resulting from Newton-Raphson iterations. The solution of the linear algebraic system of equations can be distributed across compute nodes in a cluster using MPI as the underlying message-passing framework. This enables the solution of extremely large problems, which are beyond the computational or memory limitations of individual workstations. The initial purpose of XNS was to solve the Navier-Stokes equations, and subsequent enhancements have expanded its applicability to tackle a broad spectrum of equation systems. Among other finite element techniques, XNS supports the stabilized discontinuous-in-time space-time Galerkin method that is applied to problems across engineering domains, such as injection moulding, blood-flow modeling, and bioreactor simulations. XNS stores results to disk at specified timestep intervals. This enables restarting simulations that require longer than 24 hours to complete, a common limitation on modern supercomputers.

The HD simulation is carried out in 2 stages. First, the steady-state stokes flow is solved in the bulk domain. Next, transport-adsorption equations are solved in both bulk and particle domains. As the two stages are simulated on different domains, the stationary flow field resulting from the first stage is mapped between the respective meshes, As the flow stage involves no temporal dimension due to its steady-state nature, the semi-discrete finite element approach is applied, whereas the mass transport stage is solved using the discontinuous-in-time space-time finite element method.

In this work, the previous implementation was updated to work with advances and changes in XNS. Support for reading and writing large files, adaptive time-stepping, and the chromatography module itself was brought up to date. Further updates were carried out to use the metric stabilization method with the chromatography module. In a later work package, support for periodic boundary conditions was also added.

Generic field approach in XNS

The chromatography module in XNS was implemented in what is known as classic XNS, in which the construction of matrices for specific problems are implemented in independent translation units known as blockfiles. In this framework, the multi-domain transport-adsorption problem is solved as a monolithic system. In recent years, XNS was refactored to a newer architecture, known as the generic field approach, that allows iterative coupling of arbitrary problems that are structured in a modular manner. In the generic field approach, equations in the two coupled domains would be solved iteratively until convergence.

During this work, the linear binding model was implemented into the generic field framework. Figure 4.6 shows the uptake simulations in the particle phase for a single particle, validated against an identical setup with GRM. In its current state, the coupling between the two domains can be done using dirichlet or neumann boundary conditions. A consistent boundary flux (CBF) method is yet to be implemented. Results for a single particle column test case are given in Figure 4.7.

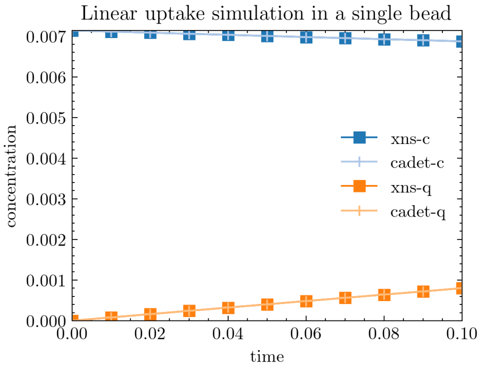

Figure 4.6: Uptake simulations in a single particle with linear binding model.

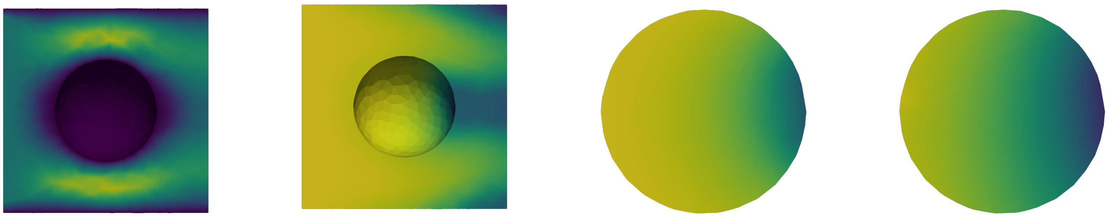

(a) u_z **(b)** c^b **(c)** c^p **(d)** c^s

Figure 4.7: Preliminary simulations showing implementation of chromatography module in XNS generic field framework with linear binding model.

4.6 Postprocessing and visualization

Postprocessing MIXD results (mesh and scalar/vector data) involves first converting them into a suitable format such that existing visualization and data processing applications can be leveraged to study the chromatography process. For this work, ParaView, a widely-used visualization and analysis tool was chosen due to several reasons. Primarily, being actively used open-source software, ParaView is under constant development, and by extension, has an active community of users. It comes with an extensive set of so-called filters (data or mesh processing operations) that can be chained together to transform results in myriad ways for analysis. Furthermore, it supports a scripting interface based on Python that enables automation and headless operation, a feature extremely useful in the context of high-performance computing. Finally, and most importantly, ParaView supports parallel file formats that enable running the post-processing pipeline on distributed systems to achieve great speedups on large datasets.

With large-scale HD simulation results containing several hundreds of gigabytes of data, parallel-enabled toolkits are an absolute necessity. In order to convert MIXD results into a file format suitable for ParaView, a new converter was written in C++: `mixd2pvtu`[†]. Built using `VTK` directly, it takes advantage of the pvtu/vtu unstructured file format that enables parallel file reads in ParaView. Keeping in mind the memory limits on individual nodes, the tool itself is also designed using MPI to be deployed in parallel across multiple nodes of a cluster.

Leveraging ParaView's scripting interface, a small library of Python/ParaView scripts[‡] (`paravision`) housing the most-used post-processing pipelines was developed during the course of this project. Several of the pre- and post-simulation visualizations and analyses shown in this work were generated using some of these scripts. `paravision` scripts can be run using either the single-process `pvpython` or the MPI-based, multi-process `pvbatch` mechanisms provided by ParaView.

4.7 Conclusions

HD simulation infrastructure is updated with new mesh generation, mesh conversion, and post-processing tools. Various contact-point modeling methods are implemented and explored, leading to the conclusion that global particle size reduction provides the most

---

[†] https://github.com/cadet/CADET-HD-mixdtools/tree/main/mixd2pvtu

[‡] https://github.com/cadet/CADET-HD-paravision

practical solution for handling contact point singularities, offering a favorable balance between computational efficiency and geometric accuracy compared to more complex local modification methods. High-level mesh generation strategies for packed-bed columns are implemented into `pymesh`. Further improvements such as anisotropic mesh generation, and inlet surface splitting, second-order element support, and periodicity are implemented as well.

The existing chromatography module and related improvements to handling large files in XNS were brought up to date. The new metric stabilization method, and support for periodic boundary conditions was implemented within the chromatography module. The implementation of the generic field approach in XNS, while still under development, shows promise for improved modularity and coupling flexibility in multi-domain transport-adsorption problems A preliminary implementation of linear adsorption model in the generic field version of XNS is showcased.

The post-processing stage of the workflow is now MPI-parallelized to scale to larger simulations and enable faster feedback loops. The use of parallel-friendly data formats were key in this regard.

These developments collectively establish a mature foundation for conducting high-fidelity chromatographic simulations that can capture the complex interplay between packing structure, flow dynamics, and mass transfer phenomena at unprecedented levels of detail.

High-definition simulation results 5

5.1 Preliminary results

Local contact-point modifications

Effect of contact-point modifications on average mesh porosity and simulation error for a short column with 750 particles was explored. Specifically, the global particle size reduction by 2 % by radius, as applied in the dissertation of Andreas Püttmann, was compared with local contact-point modifications. Particles were capped and bridged using cylinders with sizes calculated as a proportion (20 %) with respect to corresponding particle sizes. The relative holdup volume errors with respect to modified volumes (ξ_m), and ideal volumes (ξ), as well as error in mesh porosity are shown in Table 5.1.

Table 5.1: Effect of contact-point modification on holdup volumes errors.

Modification	Porosity error	ξ_m	ξ
2% Reduced	+6.5%	+12.3%	-1.4%
20% Capped	+0.71%	+15.3%	+13.9%
20% Bridged	+0.13%	+14.1%	+13.2%

It is observed that global contact point modifications cause significant deviation in volumes and porosities of geometries and meshes from ideal column geometries. In high-definition simulations, the holdup volume error is a convenient metric to calculate overall error in the column. It represents an effective increase in the retention capacity of the column due to numerical diffusion induced by the necessary stabilization methods. While local methods show consistent magnitudes of errors between ξ_m and ξ, global reduction shows a strong discrepancy in the two errors as well as an increase in the mesh porosity. In effect, the reduced packed-bed volume counterbalances the reduced flowrate in the bed, leading to a net reduction in error with respect to the ideal column (ξ).

Effect of stabilization

The result of updating the stabilization method is briefly shown in this section. Table 5.2 shows the relative holdup volume error ξ for the SUPG and metric stabilization methods for various mesh element sizes applied to a short column with 750 particles.

Table 5.2: Improvement in relative holdup volume error with metric stabilization method for a short column with monodisperse packing with 750 particles.

Mesh Size	0.08	0.10	0.12	0.15
ξ_{SUPG}	40 %	75 %	114 %	188 %
ξ_{Metric}	13 %	26 %	42 %	77 %

Conclusions

The standard configuration of high-definition simulations conducted in this work is altered based on these preliminary results. Particle sizes are reduced by a minimal amount (0.03 %) such that overlaps due to numerical precision are eliminated without affecting bed volume and capacity. Thus, the relative holdup volume with respect to the ideal column volumes, ξ, reflects the simulation error accurately. Furthermore, the metric stabilization method was applied to all subsequent simulations.

5.2 Case study

Columns with monodisperse and polydisperse packings in cylindrical confinements of radius $R = 5.01 \times 10^{-4}$ m were created for column lengths of 2.01 mm and 16.00 mm. They are henceforth referred to as short monodisperse (SM), short polydisperse (SP), long monodisperse (LM) and long polydisperse (LP). The corresponding short and long column geometries are shown in Figure 5.1 and Figure 5.13, with detailed geometry statistics given in Table 5.3. For all cases, the container extends a length of approximately $0.2d_c$ on either end of the the packed bed, where d_c is the column diameter.

Table 5.3: Geometrical properties of simulated packed-bed columns.

Identifier	Particle Size Distribution	Column Length (mm)	Number of Particles (−)	Avg. Particle Radius (µm)	Column Porosity (−)	Bed Porosity (−)	Bed Length (mm)
SM	monodisperse	2.01	1,360	49.985	0.551	0.438	1.607
SP	polydisperse	2.01	1,002	52.798	0.543	0.444	1.649
LM	monodisperse	16.00	13,845	49.985	0.425	0.411	16.000
LP	polydisperse	16.00	9,874	53.144	0.425	0.401	15.358

The monodisperse packing consists of constant-sized particles with diameter $d_p \approx \frac{d_c}{10}$. Polydisperse packings, being naturally more densely packed by due to smaller particles

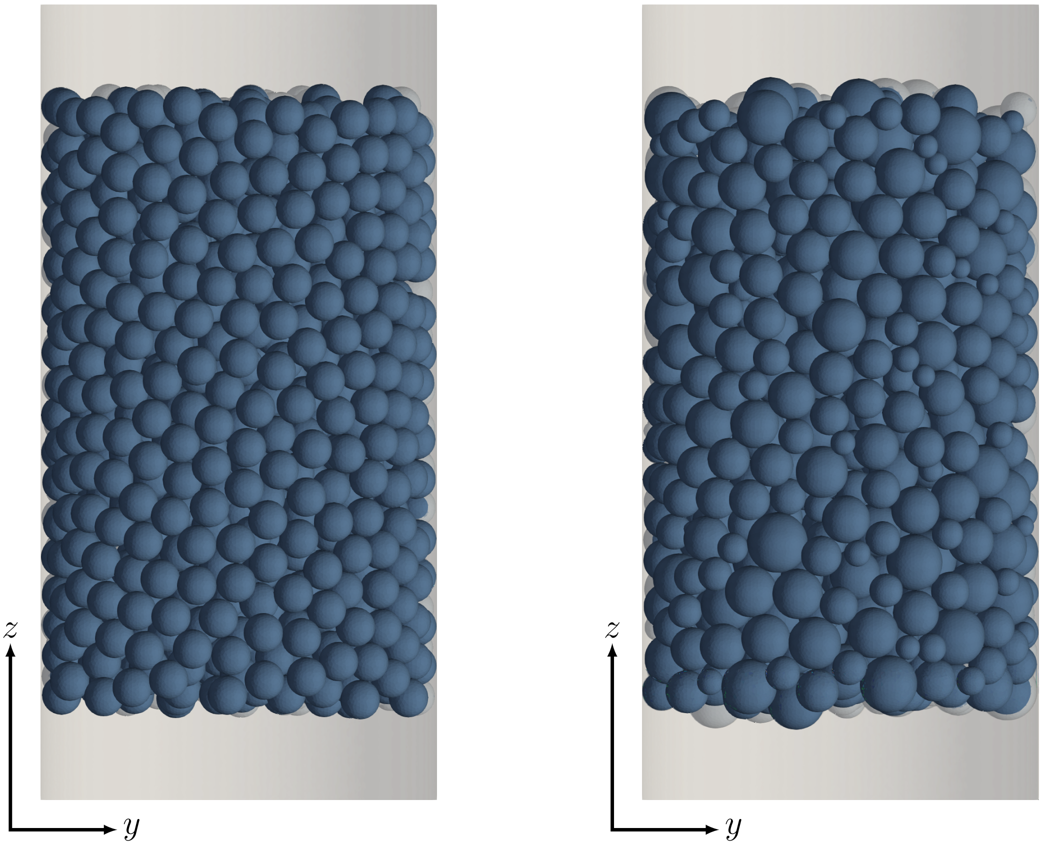

(a) SM packing **(b)** SP packing

Figure 5.1: Geometry of short monodisperse (SM) and short polydisperse (SP) packings.

nestling between larger ones, were adjusted until the average total column porosities matched those of the monodisperse counterparts. The PSD of the polydisperse packed-bed is shown in Figure 5.2a. It is representative of a measured PSD of Sepharose [67].

The variation in column porosity across the column radius for LM and LP columns is shown in Figure 5.2b. Geometric wall effects are clearly visible in the porosity plot, where local porosity ε_c tends towards a value of 1.0 at the container walls. The structural constraint at the wall causes a regularity in the distribution of particles that is otherwise random, resulting in large oscillations in local porosity. For the column configurations chosen in this work, it is observed that the oscillations stabilize towards the column center for the polydisperse packings, while still being significant in the case of monodisperse packings. The disparity in particle sizes in polydisperse packings enables a more efficient and uniform packing, whereas interstitial gaps in monodisperse packings remain unfilled, leading to larger oscillations. As the column's diameter ratio $\frac{d_c}{d_p}$ is increased, such oscillations would vanish at the center of the column.

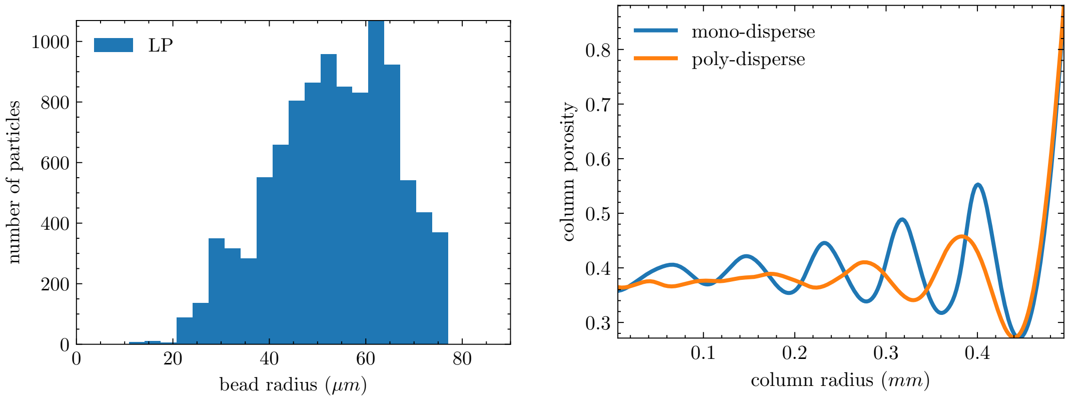

(a) Particle size distribution

(b) Porosity profile

Figure 5.2: PSD of LP packing and porosity profiles of LM and LP packings.

Meshes

The mesh size for all meshes in this work is characterized based on the element size relative to the average particle diameter. Thus, an element size of 0.10 corresponds to 10 elements per particle diameter. Hereafter, specific meshed columns are referred to with their mesh element sizes suffixed to their column types, i.e., SP–0.04 refers to the short polydisperse column with an element size of 0.04.

As the local element size is scaled by particle sizes in order to capture curvatures of small and large particles alike, meshes of monodisperse columns always result in uniform element sizes, whereas the mesh is denser in the vicinity of smaller particles in polydisperse columns. Figure 5.3 shows the meshes applied at various element sizes to polydisperse particle surfaces.

Model setup and parameters

Chromatography model parameters for all simulations in this work were adopted from another work [64]. These parameters are tabulated in Table 5.4. They reflect the binding behavior of lysozyme on blue Sepharose particles.

Although it is possible to simulate the typical load-wash-elution cycles of chromatography, this work is focused on only the loading stage. Both domains of the column are empty at $t = 0$. A step input is given as the inlet concentration, and the column is simulated until it is completely saturated and the outlet concentration matches the inlet concentration. This leads to a breakthrough curve at the column outlet.

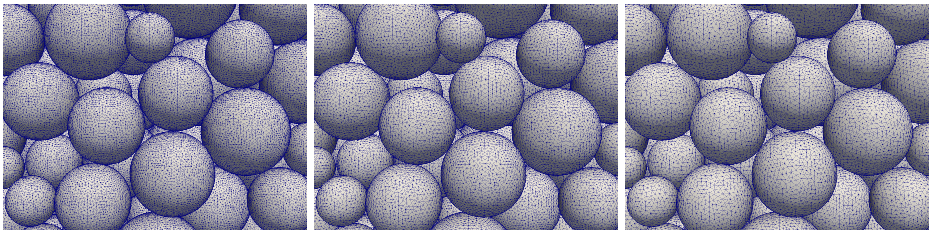

(a) SP–0.04 **(b)** SP–0.05 **(c)** SP–0.06

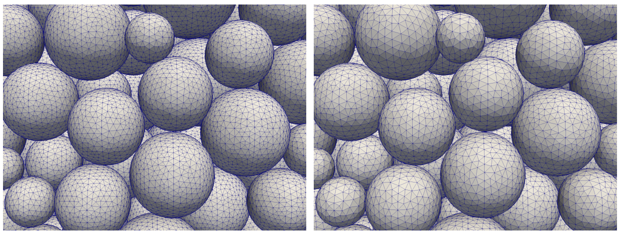

(d) SP–0.08 **(e)** SP–0.10

Figure 5.3: Zoomed in tetrahedral meshes of polydisperse packing used for mesh sensitivity study.

Table 5.4: Chromatography model parameters.

Parameter	**Value**	**Unit**
D_b	$1.15 \cdot 10^{-10}$	$\mathrm{m^2\,s^{-1}}$
D_p	$7.07 \cdot 10^{-11}$	$\mathrm{m^2\,s^{-1}}$
ε_p	0.75	–
k_a	1.144	$\mathrm{m^3\,mol^{-1}\,s^{-1}}$
k_d	$2 \cdot 10^{-3}$	$\mathrm{s^{-1}}$
c^s_{max}	4.88	$\mathrm{mol\,m^{-3}}$
c^b_{in}	$7.14 \cdot 10^{-3}$	$\mathrm{mol\,m^{-3}}$
u_z^{in}	$2.09 \cdot 10^{-4}$	$\mathrm{m\,s^{-1}}$

5.3 Mesh sensitivity study

A mesh sensitivity study was conducted with the aim of investigating the flow and mass transfer behavior of the system, as well as assessing the numerical stability, accuracy, and consistency of the employed methods. Tetrahedral unstructured meshes for short column models, SM and SP, were generated with five distinct refinement levels ranging from 0.10 to 0.04.

In comparison to conventional breakthrough curves, the extremely short column length in the test case causes a rapid partial breakthrough. This is observed as a discontinuous jump in the initial concentration in the chromatogram in Figure 5.4a. Due to the short residence time, some particles do not diffuse into the particles, essentially being directly flushed out of the column. This is also exacerbated due to the relatively low column-to-particle diameter ratio of the column ≈ 10, making wall effects a significant factor. Higher residence time in longer columns allows solute molecules sufficient time to diffuse into particles and adsorb.

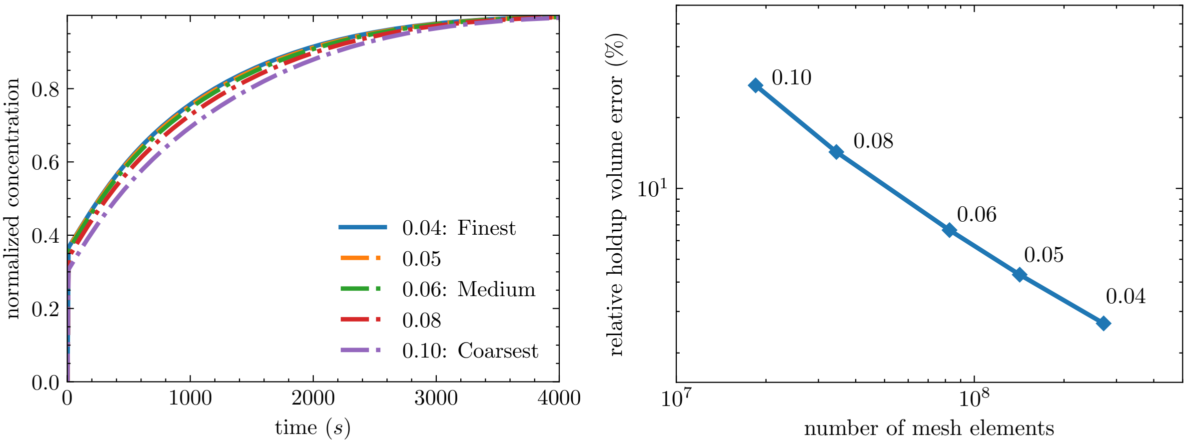

(a) Breakthrough chromatograms

(b) Mesh convergence

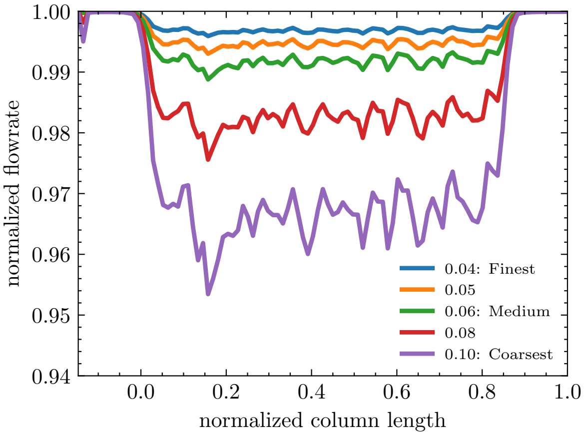

(c) Mass flux error

Figure 5.4: Results of flow and transport simulations for short polydisperse column with varying element sizes.

As finite element methods are not locally conservative, it is important to verify mass balance within the column. Figure 5.4c shows average flowrates in the SP column at various cross sections along it's length. Improvement in mesh density leads to a reduction in the flowrate error, which drops below 1% for element sizes 0.06 and finer. The corresponding breakthrough curves for SP simulations is shown in Figure 5.4a. At these column lengths, the breakthrough curves of the three finest meshes are almost indistinguishable from one another. The generalized holdup error, ξ (Equation 2.13), in these curves, however, drops from 8% to 3% as shown in Table 5.5 and Figure 5.4b.

Table 5.5: Mesh sensitivity results for SM and SP columns.

Geometry/ Element Size	Elements Interstitial	Elements Total	ξ
SM–0.04	131.34M	244.67M	3.26%
SM–0.05	67.01M	131.86M	5.50%
SM–0.06	39.76M	070.98M	8.65%
SM–0.08	16.86M	031.37M	19.83%
SM–0.10	8.94M	016.74M	41.46%
SP–0.04	143.09M	271.65M	2.67%
SP–0.05	72.30M	142.01M	4.30%
SP–0.06	42.52M	082.57M	6.65%
SP–0.08	18.16M	034.46M	14.28%
SP–0.10	9.57M	018.46M	27.40%

5.4 Flow field hotspots

Flow in the complex interstitial domain, with its intricate network of widening and contracting channels around the packed bed, leads to extremely nonlinear velocity gradients. In these channels, velocity is zero at the particle and wall surfaces due to friction, but in order to maintain the overall flowrate, the fluid is forced to accelerate in the space between these surfaces, leading to hotspots of high velocity.

Figure 5.5 shows the x, y, and z components of the normalized velocity field $(\frac{u_i^b}{\tilde{u}_z^b})$ in the central x-y, and y-z planes of the SM geometry. Here, $\tilde{u}_z^b = u_z^{in}/\varepsilon_c$ denotes the average interstitial z velocity in the packed-bed.

Velocity hotspots were found throughout the bulk domain, with maximum magnitudes for the x- and y-components reaching approximately four times that of the characteristic flow velocity $\tilde{u}_z^b$, while z-component hotspots achieved values roughly ten times greater than this characteristic velocity. Figure 5.6 shows the hotspot regions at progressively higher velocity thresholds, where $u_z > n \cdot \tilde{u}_z^b$, with $n \in [1, 5]$.

The influence of mesh density on the velocity hotspots is illustrated in Figure 5.7, which examines the volume fractions occupied at various thresholds for different mesh resolutions. It is observed that finer meshes are capable of capturing substantially more hotspot volume compared to coarser meshes at lower threshold values; however, these differences diminish as the threshold increases. This indicates that finer meshes perform better than coarser ones due to their ability in capturing areas of lower velocity thresholds, i.e., boundary layers on surfaces. While finer meshes also naturally contribute to accurately capturing

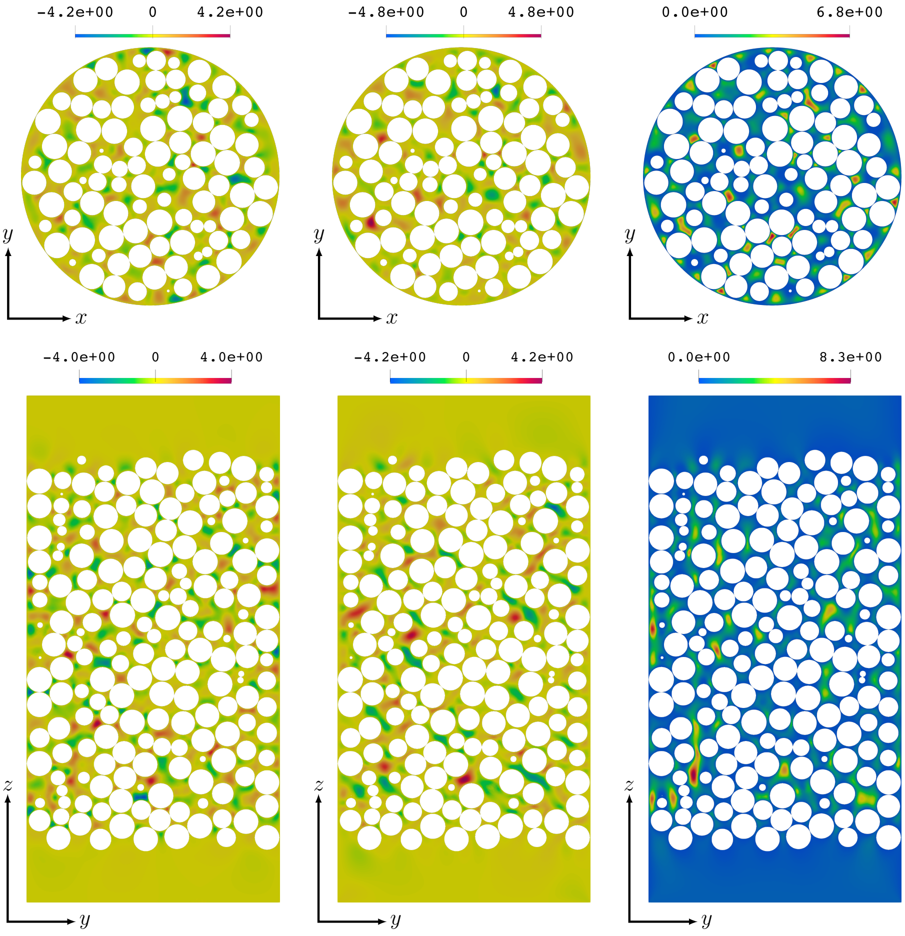

(a) u_x **(b)** u_y **(c)** u_z

Figure 5.5: Normalized velocity components $\frac{u_i^b}{\tilde{u}_z^b}$ in central x-y and y-z planes of SM geometry. Direction of flow is upward.

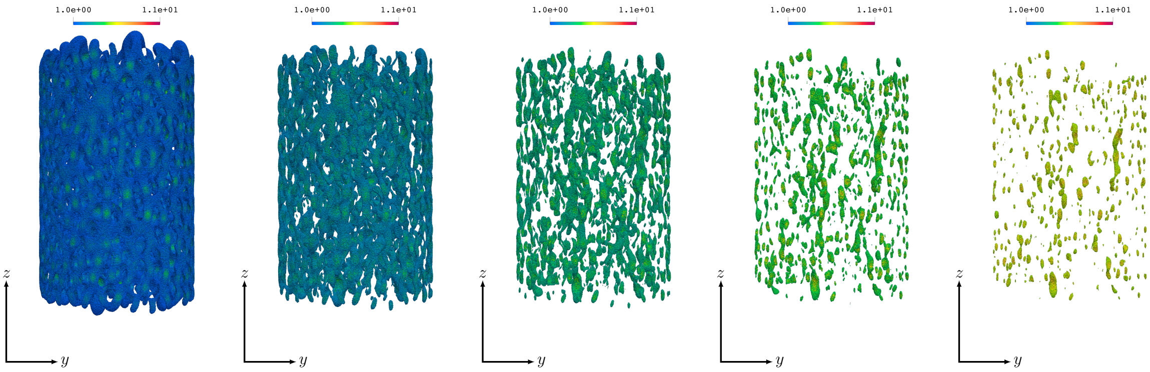

(a) $u_z \geq \tilde{u}_z^b$ **(b)** $u_z \geq 2\tilde{u}_z^b$ **(c)** $u_z \geq 3\tilde{u}_z^b$ **(d)** $u_z \geq 4\tilde{u}_z^b$ **(e)** $u_z \geq 5\tilde{u}_z^b$

Figure 5.6: Normalized axial velocity ($\frac{u_z^b}{\tilde{u}_z^b}$) hotspots at various thresholds in SM geometry.

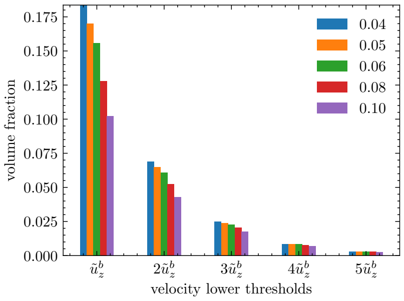

Figure 5.7: Hotspot volume fraction over velocity threshold for SM geometry.

velocity peaks, their effect is negligible due to their diminished overall volumes. This result provides great insight that can be used in generating meshes with a gradient density, with a finer element size at surfaces in comparison to the bulk region.

5.5 Transport and adsorption

In the bulk phase, convective transport prevails, whereas within the particle domain, mass transport is governed exclusively by diffusive mechanisms. Transport between the bulk and particle domains is contingent upon the bulk phase concentration around the given particle, which is further influenced by local fluid dynamics and geometric properties, including position, size, and configuration, of the particle itself as well as its neighboring particles. The local flowfield around particle surfaces is slower due to friction between the surface and fluid, forming a diffusive barrier at the surface that imparts an additional mass transfer resistance. This is modeled in reduced-order models as a film-diffusion resistance.

Figures 5.8 to 5.10 show snapshots of the normalized bulk, particle pore and solid phase concentrations in the central y-z plane of the SM column at different times (compare Figure 5.4a), including zoom boxes of specific regions. Visual inspection of these images reveals a pronounced wall effect, where the concentration front advances more rapidly towards the column walls compared to its central region. This wall effect is attributed to the increased porosity (Figure 5.2b), and consequently increased velocity (Figure 5.5c) at the wall. The velocity profile mostly matches the porosity profile, except directly at the wall, where the effect of friction dominates for a thin region.

As the mass transport behavior of a particle is influenced by the surrounding bulk concentration, it must be homogeneous for symmetric loading. Conversely, inhomogeneities such as wall effects, channeling, and variations in particle size distribution can lead to uneven advancement of the concentration front within the packed bed, resulting in asymmetrical loading patterns as exemplified by Figure 5.8c.

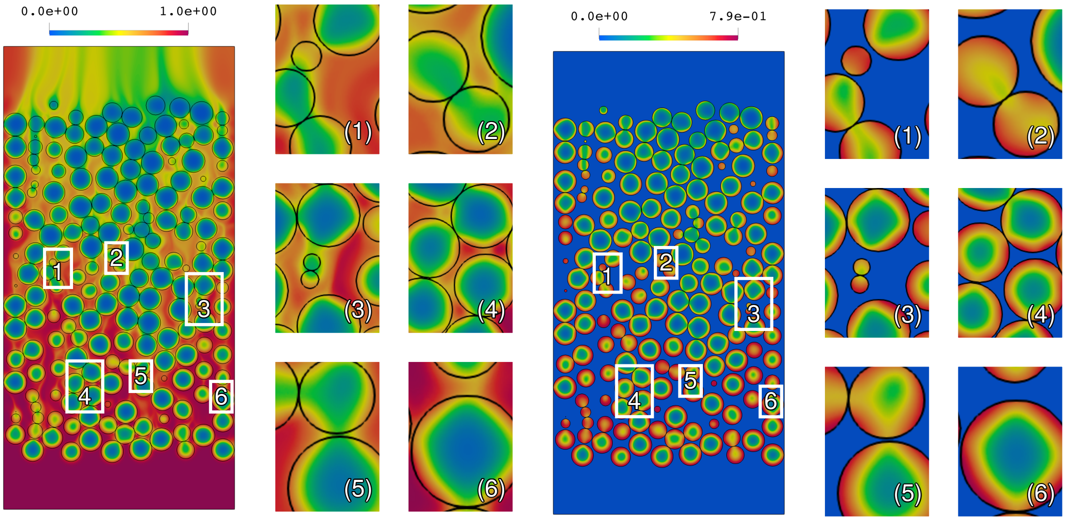

(a) c^b and c^p **(b)** zoom boxes **(c)** c^s **(d)** zoom boxes

Figure 5.8: Normalized bulk ($\frac{c^b}{c^b_{\text{in}}}$), particle pore ($\frac{c^p}{c^b_{\text{in}}}$) and solid ($\frac{c^s}{c^s_{\max}}$) phase concentrations in central y-z plane of SM column at time $t \approx 550s$ with zoom boxes of specific regions. Direction of flow is upward.

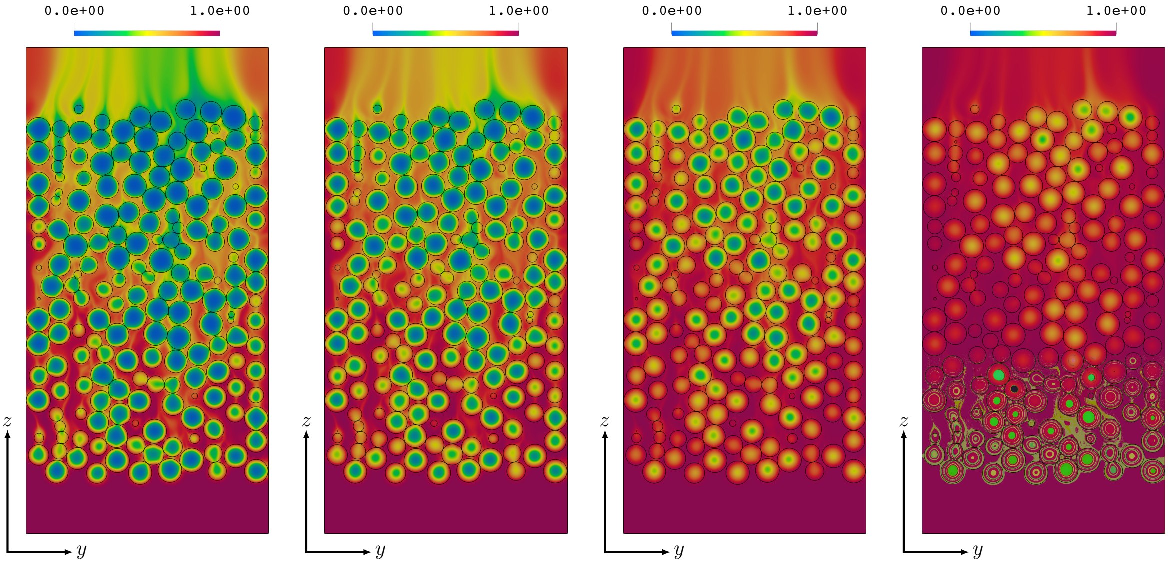

(a) $t \approx 550s$ **(b)** $t \approx 840s$ **(c)** $t \approx 1275s$ **(d)** $t \approx 1920s$

Figure 5.9: Normalized bulk ($\frac{c^b}{c^b_{\text{in}}}$) and particle pore ($\frac{c^p}{c^b_{\text{in}}}$) phase concentrations in central y-z plane of SM column at different times. Direction of flow is upward.

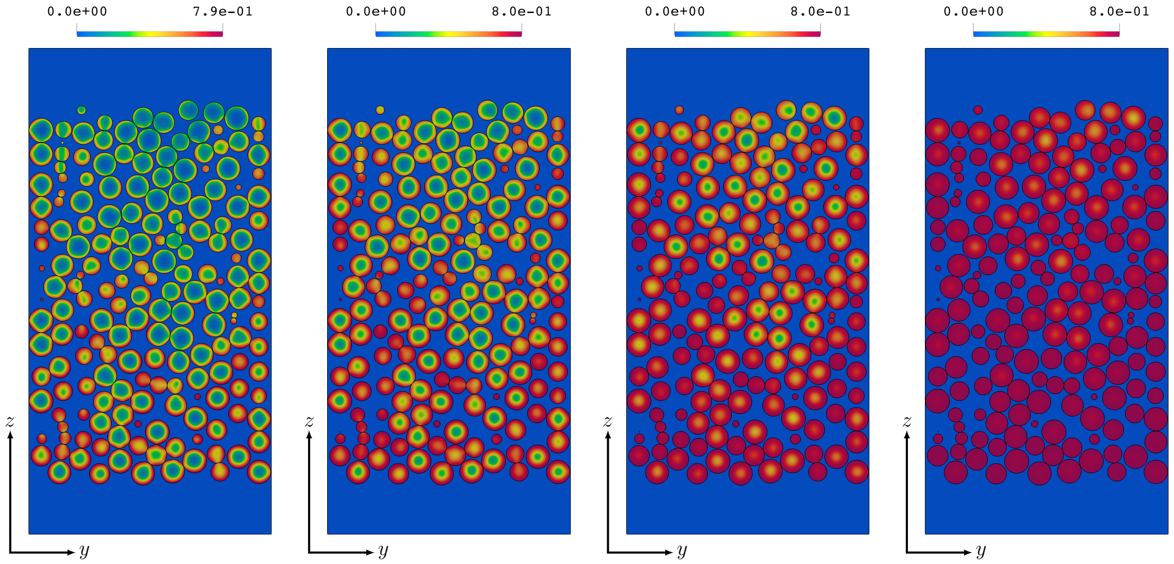

(a) $t \approx 550s$ **(b)** $t \approx 840s$ **(c)** $t \approx 1275s$ **(d)** $t \approx 1920s$

Figure 5.10: Normalized solid phase concentration ($\frac{c^s}{c^s_{\max}}$) in central y-z plane of SM column at different times.

The asymmetry in loading behavior is exacerbated for smaller particles, which are typically loaded faster than larger ones. This is because the asymmetry in the bulk domain diminishes as the loading process continues and the solute concentrations in the bulk reaches equilibrium. Thus, over time, larger particles experience symmetric boundary conditions forcing symmetry in the later stages of particle loading.

5.6 Particle loading

The high fidelity of the HD simulations enables visualization and analysis of the loading and unloading of individual particles, enabling the study of the impact of particle size and axial/radial positioning on the loading process. Figure 5.11 shows loading profiles of all particles in the SM and SP simulations coloured by axial position in the column and the time required for reaching 90% saturation over axial position. The plotting order of the loading curves was randomized to avoid bias caused by overlays in the final plot. While the particle sizes are a confounding factor in the polydisperse case, the monodisperse plot clearly shows an increase in the bandwidth of the saturation scatter plot at the column outlet. This is due to the previously showcased wall effects, with particles at the walls being loaded progressively faster towards the end of the column, in comparison to particles in the center and beginning of the column.

Similarly, Figure 5.12 shows loading profiles of all particles in the SP simulations coloured by particle radius and the time required for reaching 90% saturation over the particle radius. Visualizations provided in these figures effectively demonstrate the influence of particle size distribution on the column's loading behavior. Figure 5.11d and 5.12b show that particle size has a dominant impact on the saturation time of individual particles in comparison to its axial position in the column.

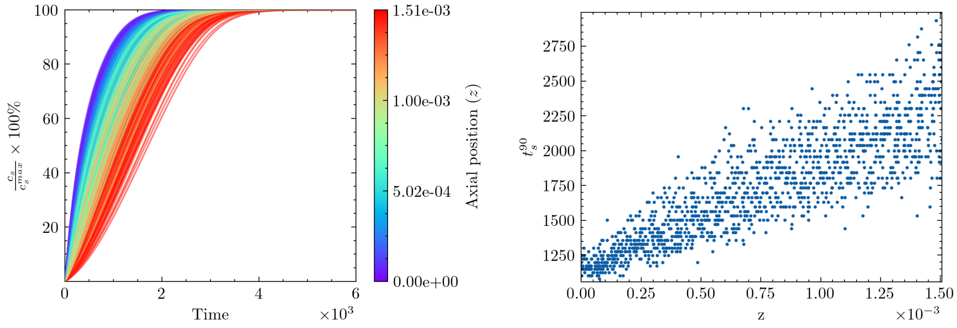

(a) SM loading curves over time **(b)** SM 90% loading times over axial position

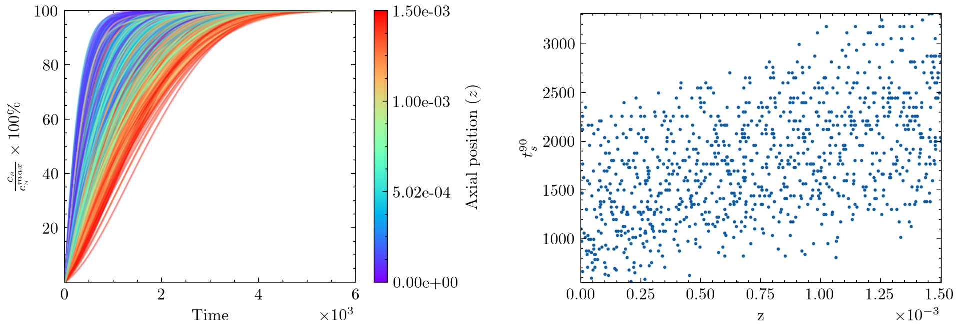

(c) SP loading curves over time **(d)** SP 90% loading times over axial position

Figure 5.11: Effect of axial position on particle loading curves (left) and 90% loading time (right) in SM (top) and SP (bottom) simulations.

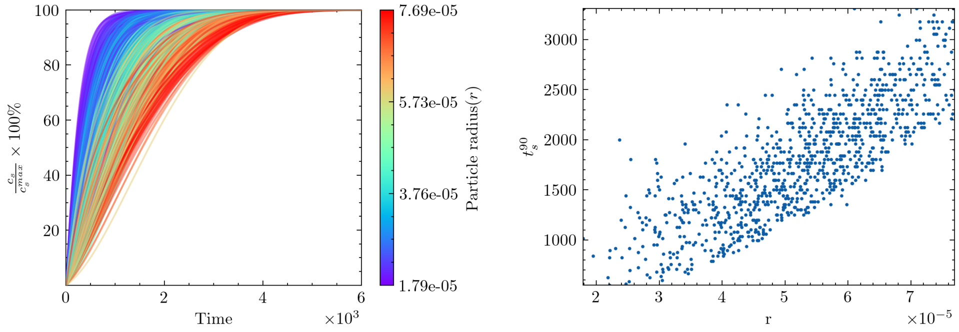

(a) Loading curves over time **(b)** 90% loading times over particle radius

Figure 5.12: Effect of particle radius on particle loading curves (left) and 90% loading time (right) SP simulations.

5.7 Large-scale simulations

The impact of PSD on fully developed breakthrough curves is investigated using the long monodisperse (LM) and polydisperse (LP) columns shown in Figure 5.13.

Both columns are constructed to have identical total porosity and capacity with identical bed volumes. Due to different packing densities in the monodisperse and polydisperse cases, this results in different bed lengths. Geometrical details are given in Table 5.3.

The sizes of usable meshes in XNS are currently constrained by limitations in integer representation. To facilitate further enhancements, modifications must be made to the binary mesh storage format to allow for the number of elements to exceed the current limit of 2,147,483,647. Arithmetic operations in XNS involving these numbers may also overflow and are required to be updated. In fact, such modifications would have to be implemented in the entire toolchain, including some dependencies.

The element size of 0.06 yielded generalized holdup volume errors of 8.65% and 6.65% in the mesh sensitivity study for the SM and SP cases respectively. Generating meshes for LM and LP with this element size produced meshes with 561M and 583M elements respectively. Results of simulations performed with these meshes are presented in Table 5.6.

Table 5.6: Mesh characteristics for LM and LP columns.

Geometry/ Element Size	Elements Interstitial	Elements Total	ξ
LM–0.06	235.88×10^6	561.53×10^6	8.20 %
LP–0.06	237.89×10^6	583.79×10^6	6.43 %

Velocity profiles for the LM and LP cases, superimposed over corresponding porosity profiles are shown in Figure 5.14a. Apart from the boundary layer at the container wall, the velocity profiles in both cases match the porosity corresponding profiles. Scatter plots of velocity vs. porosity with linear regression applied to the two variables is shown Figure 5.14b. The correlation is stronger in LP with $R^2 = 0.81$, as opposed to LM with $R^2 = 0.57$.

Normalized bulk, particle pore, and solid phase concentrations in the LP column are shown for three different times in Figure 5.15 . Consistent patterns of transport were noted in these longer columns, with characteristics that mirrored those previously observed in shorter counterparts. These comprehensive simulations provide the opportunity to systematically investigate and quantify the influence of particle size distribution (PSD) on breakthrough curves (BTCs).

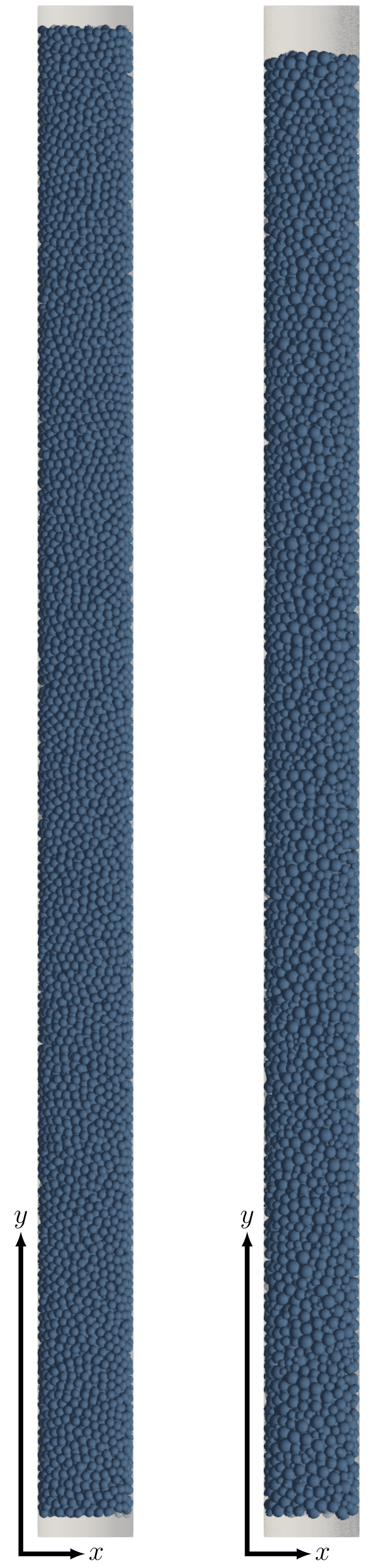

(a) LM packing **(b)** LP packing

Figure 5.13: Geometry of long monodisperse (LM) and long polydisperse (LP) packings.

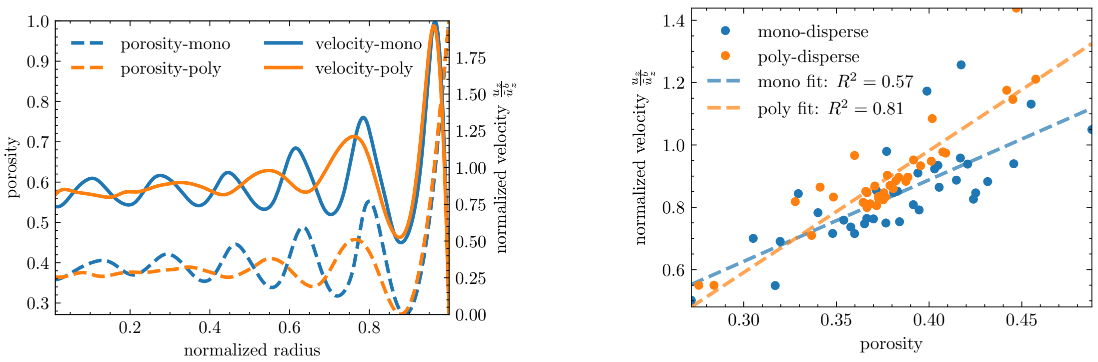

(a) Porosity and normalized velocity over column radius

(b) Linear regression of normalized velocity over porosity

Figure 5.14: Porosity and normalized velocity profiles and their correlations for LM and LP columns.

Note that the HD model implicitly describes the root causes of column dispersion by modeling flow and molecular diffusion in different trajectories through the bulk domain. The no-slip friction condition at the particle surfaces and column walls contribute to this. Furthermore, the diffusive barrier due to the boundary layer at particle surfaces is also inherently modeled in the flowfield. Hence, the discrepancies observed in BTC shape and slope (Figure 5.16) between the two columns are mechanistically predicted. In other words, dispersion is not explicitly accounted for in the mass transfer equation in the bulk domain, Equation 2.3, but emerges implicitly due to the characteristics of the underlying flow field.

Simulation error due to the mass flux error described in section 5.3 results in a slightly delayed chromatogram with respect to the ideal case. This can be corrected by rescaling the chromatogram with the holdup volume ratio as shown in Figure 5.17. This implicitly corrects the chromatogram with the error in interstitial flowrate.

Scalability of flow simulations

The scalability of XNS and the steady-state incompressible Stokes flow simulations using the LP column is demonstrated in Table 5.7. Simulations were performed on JURECA DC standard compute nodes, each equipped with two 64-core AMD EPYC CPUs and 512 GB of main memory. Starting from a reference of 320 processes, results show ideal efficiency up until 1920 processes, which implies an opportunity for further growth.

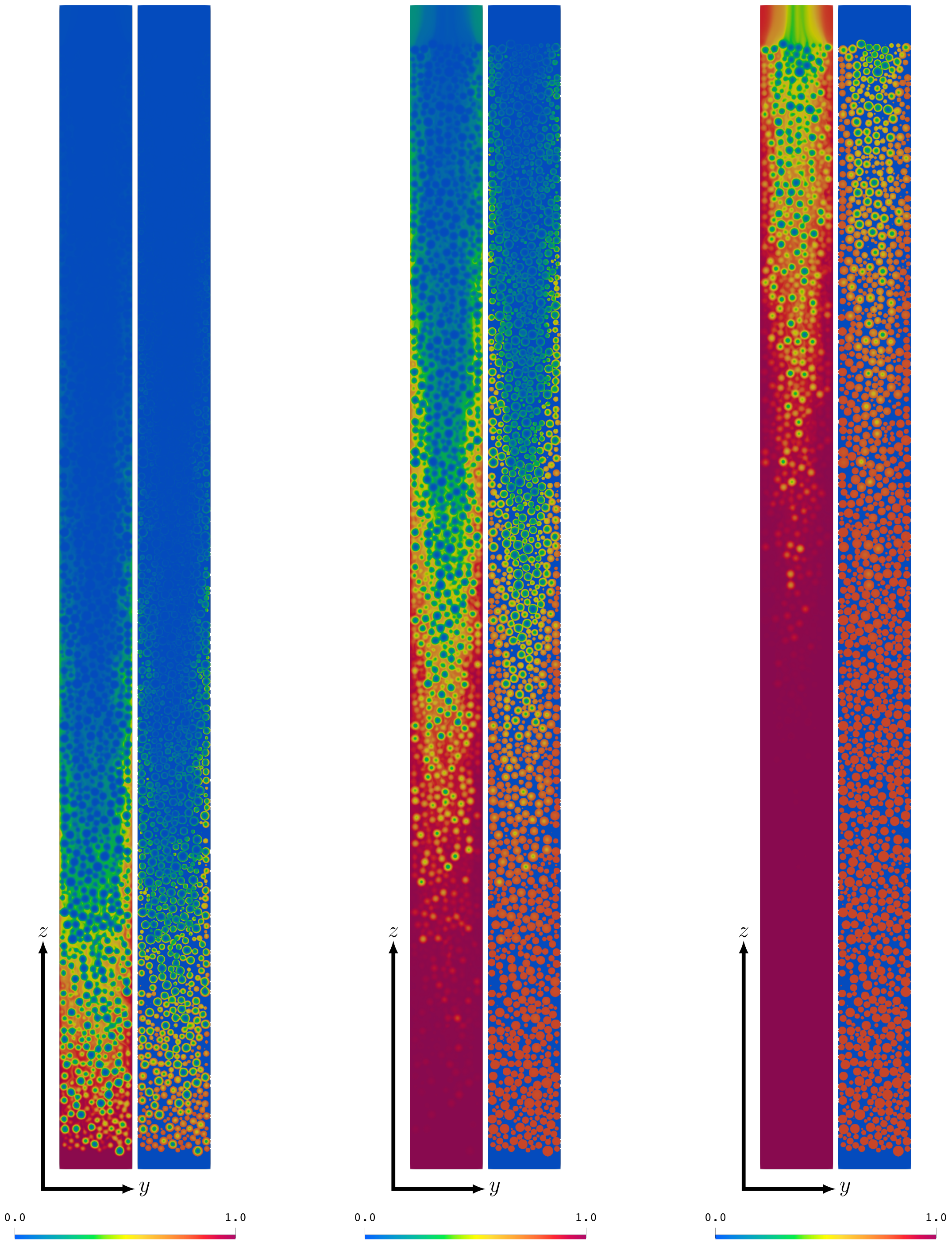

(a) $t = 1500s$ **(b)** $t = 4500s$ **(c)** $t = 7500s$

Figure 5.15: Central y-z plane of normalized bulk ($\frac{c^b}{c^b_{\text{in}}}$), particle pore ($\frac{c^p}{c^b_{\text{in}}}$) and solid ($\frac{c^s}{c^s_{\text{max}}}$) phase concentrations in LP simulation at different times. Direction of flow is upward.

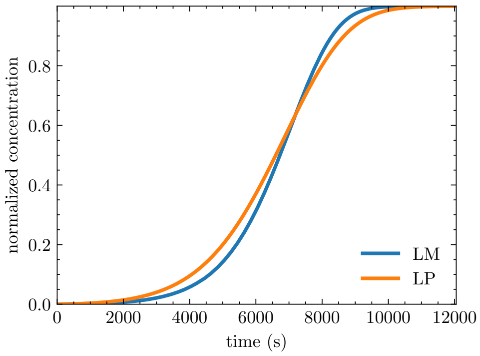

Figure 5.16: Breakthrough curves for LM and LP geometries shows band broadening in LP.

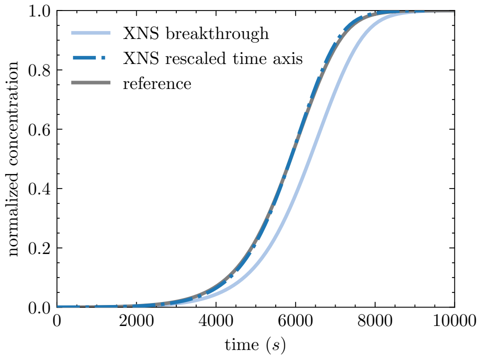

Figure 5.17: GRM based evaluation of BTC rescaling by holdup volume ratio $\varrho = 1.082$.

Table 5.7: Strong scaling results (JURECA-DC) for the steady-state fluid flow simulation using a mesh of 238M elements.

Cores	Time	Speedup	Ideal Speedup	Efficiency
320	2487	1.00	1.0	1.00
480	1617	1.53	1.5	1.02
640	1449	1.71	2.0	0.86
960	765	3.24	3.0	1.08
1280	587	4.23	4.0	1.06
1920	417	5.96	6.0	0.99

5.8 Anisotropic meshes

An anisotropic mesh with finer elements near particle and wall surfaces as shown in Figure 4.4 was applied to the SM goemetry. Element sizes in the bulk domain ranged from 0.05 far away from boundary layers, and 0.03 within boundary layers and at the particle and wall surfaces. Element sizes within the particle domain, away from the surface, was set to 0.10.

This resulted in columns with significantly reduced number of elements in comparison to meshes with uniform element sizes. In this case, 54.90 % and 65.20 % reductions in the number of elements were observed in the interstitial and particle domains respectively, with negligible change in the relative holdup volume error. The comparison is shown in Table 5.8.

Table 5.8: Anisotropic mesh applied to SM geometry resulted in significant reduction in total mesh size with negligible changes to holdup volume error.

Geometry	Element size		Elements		ξ
	Interstitial	Particles	Interstitial	Particles	
SM	0.04	0.04	131.34M	244.67M	3.26%
SM	0.05–0.03	0.03–0.10	59.24M	85.14M	3.37%

5.9 Conclusions

HD simulations of short and long columns with monodisperse and polydisperse packings were conducted. Analysis of velocity hotspots showed that results were more sensitive to mesh element size changes in regions with lower flow velocity in comparison to regions with higher flow velocity. Consequently, anisotropic meshes with finer element sizes in the boundary layer region near particle and wall surfaces were constructed and simulated. When compared with the finest uniform mesh, results for short column simulations with an anisotropic mesh show a significant decrease in the number of elements (by 61.60 %) at comparable levels of generalized holdup volume errors (3.37 % vs. 3.26 %).

Simulation error for long columns with approximately 10 000 particles with uniform meshes at medium coarseness were observed to be 8.20 % and 6.43 % for monodisperse and polydisperse packings respectively.

Transport-adsorption simulations show strong wall effects causing an inverted parabolic concentration front. Particle loading plots also show wall effects in the widening distribution of particle loading times along the column length with monodisperse packing. Particle radius plays a stronger role in polydisperse cases, leading to a highly scattered axial loading distribution.

6 ROM calibration workflow

Reduced-order model coefficients are conventionally estimated using empirical correlations, which require several pulsed injections or breakthrough experiments. For example, the height of equivalent theoretical plate (HETP) and Van Deemter equation [68] can be used to calculate the axial dispersion coefficient, which can then be used in 1D ROMs.

This method suffers from several key problems, notwithstanding issues with column homogenization inherent in ROMs.

- It requires several experimental runs.
- Experimental results are typically noisy.
- Chromatgrams, which are merely the concentration flux at the column exit, are used to characterize the state of the entire column.
- Empirical correlations provide a statistical method to estimate model coefficients, but do not take any specificities into consideration.

On the other hand, HD simulation results serve as excellent sources of reference data in the form of chromatograms and the internal solute concentrations in all phases. As they mechanistically simulate dispersion and thin-film boundary layers from fundamental equations of flow and transport around a spatially resolved packed bed, HD results are especially suited for calibration of ROMs using the dispersion coefficient and thin-film diffusion coefficients. Finally, as reference data from multiple domains and phases can be extracted, they enable consistent calibration of ROMs to the complete internal state of the column, leading to robust and accurate characterization of columns via multi-objective optimization techniques. HD simulation results are especially powerful as sources of reference data for 2D ROMs, as they can provide radially-resolved reference data, which is necessary in order to calibrate radially varying dispersion parameters.

The proposed calibration workflow is illustrated in Figure 6.1. It comprises of preparing reference data from HD simulations, configuring the ROM simulation, and the parameter estimation process.

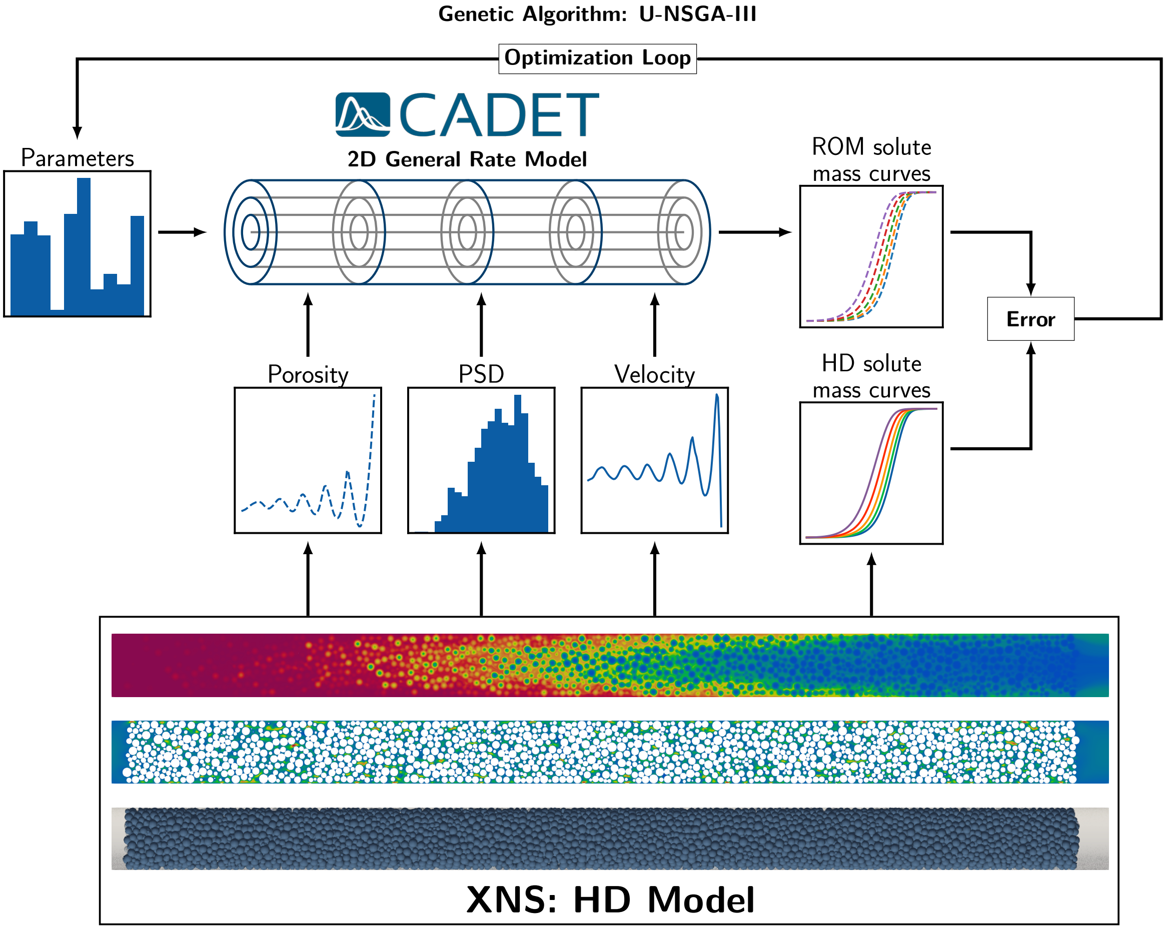

Figure 6.1: ROM calibration workflow.

6.1 Preparation of reference data

Chromatograms, i.e., averaged concentrations at the column outlet, are considered the de facto standard output of chromatography columns due to their simplicity and functional utility during fractionation. Effects of several column and environmental inputs on the chromatogram are thoroughly studied, with chromatogram features being strongly tied to column performance. They are also used as objectives and reference data in calibrating ROMs.

However, chromatograms are not uniquely representative of the internal state of the entire column as they are only the averaged solute concentrations at the column outlet.

Consider the following example with two 1D GRM ROMs: Model 1 does not account for thin-film boundary resistance, i.e., $k_f = \infty$, and Model 2 assumes a finite k_f. Only the column dispersion coefficient, D_{ax}, is calibrated for Model 1, whereas both D_{ax} and k_f are calibrated for model 2. If the calibration is performed with respect to the 1D breakthrough

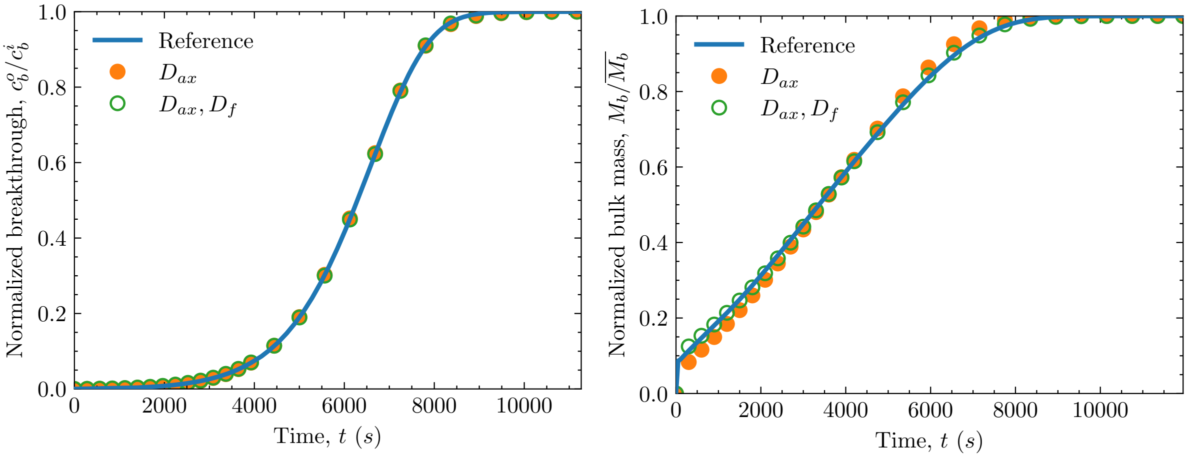

(a) Breakthrough curves

(b) Bulk mass curves

Figure 6.2: Calibration results for 1D GRM without PSD

curve, both models are able to fit the reference data perfectly as shown in Figure 6.2a. This is because both k_f and D_{ax} result in a band-broadening effect on the chromatogram, enabling one parameter to compensate for the other. Although both models are able to fit the reference data accurately, the resulting internal states of the two columns are distinctly different due to fundamentally different mechanisms being calibrated to different degrees. Ultimately, the calibration process only accounts for the sensitivity of the model outputs with respect to model inputs. Hence, chromatograms are not ideal in the scenario where ROMs are required to robustly represent the reference column state after the calibration process.

Solute masses in each phase (M_b, M_p, and M_s; Equation 6.1), especially when considered together, are unique representations of the internal column state. When models 1 and 2 are calibrated against solute mass in the bulk phase, M_b, a clear distinction between them emerges in the fit plot in Figure 6.2b .

$$M_b = \int_{\Omega_1} c^b \, dV \tag{6.1a}$$

$$M_p = \int_{\Omega_2} \varepsilon_p c^p \, dV \tag{6.1b}$$

$$M_s = \int_{\Omega_2} (1 - \varepsilon_p) c^s \, dV \tag{6.1c}$$

The solute masses, M_b, M_p, and M_s, are used as objectives in this work. Furthermore, using all the objectives in tandem allows the optimizer to account for the mass balance in different solute phases within the column, resulting in calibrated columns very closely approximating the reference column.

The reference data for each objective, $\overline{M}_b^w$, $\overline{M}_p^w$, and $\overline{M}_s^w$, are calculated from HD simulation results as shown in Equation 6.2.

$$\overline{M}_b^w = \int_{\rho_{w-\frac{1}{2}}}^{\rho_{w+\frac{1}{2}}} \int_0^{2\pi} \int_0^L c^b \, dV \qquad \forall w \in \{1, \dots, N_\rho\} \quad \text{in } \Omega_1 \tag{6.2a}$$

$$\overline{M}_p^w = \int_{\rho_{w-\frac{1}{2}}}^{\rho_{w+\frac{1}{2}}} \int_0^{2\pi} \int_0^L \varepsilon_p \, c^p \, dV \qquad \forall w \in \{1, \dots, N_\rho\} \quad \text{in } \Omega_2 \tag{6.2b}$$

$$\overline{M}_s^w = \int_{\rho_{w-\frac{1}{2}}}^{\rho_{w+\frac{1}{2}}} \int_0^{2\pi} \int_0^L (1 - \varepsilon_p) c^s \, dV \qquad \forall w \in \{1, \dots, N_\rho\} \quad \text{in } \Omega_2 \tag{6.2c}$$

where the column radius r_c is discretized into N_ρ radial zones ρ_w, bounded by lower and upper radii $[\rho_{w-\frac{1}{2}}, \rho_{w+\frac{1}{2}}]$ with $w \in \{1, \dots, N_\rho\}$. The index w is omitted in 1D calibrations.

As per convention, solute masses are spatially integrated in the axial direction. Along the radial direction, the same discretization scheme used to configure the reduced-order model is applied to integrate results within the discrete radial zones.

6.2 ROM Configuration

Chromatography models may be, theoretically, made arbitrarily simple or arbitrarily complex in their representation of the process. In essence, a spectrum of model complexity may be charted based on the characteristics of each model with respect to several aspects of its representation of the column. In the field of chromatography, there exist several reduced-order models that fall on the simpler side of this spectrum (LKM, EDM, etc.), and several others that embrace complexity, such as the 2D/3D general rate model. Apart from initial and boundary values, and numerical solver configurations, a typical ROM can be broadly characterized by the following features.

Compartmentalization Void spaces before and after the packed bed can be either modeled separately as plug flow reactors, or lumped into the column's packed-bed unit operation.

Dimensionality The extent of local variations in porosity and velocity profiles within the column in the axial and radial directions dictates the dimensionality of the model.

Bed morphology Particle shapes and size distribution can be modeled. Futhermore, different particle types with differing affinities for multiple solute components can also be modeled.

Mass transfer kinetics The appropriate level of resolution of various mass transfer phenomena depends on the chosen transport model (e.g., GRM, LKM, etc.) and the choice of model parameters considered.

Adsorption model The choice of the appropriate binding model is informed by the physical properties of the solute components, and the stationary phase.

The aim of this work is the accurate and robust calibration of 1D/2D GRM to the HD simulation results of the LM and LP column geometries described in section 5.2.

A compartmentalized approach is taken to represent the column's void spaces and packed-bed regions as depicted in Figure 6.3. Void spaces are modeled using the lumped rate model without pores (LRM). Axial dispersion in these unit operations is neglected, and the column porosity is set to 1.0, making it a plug flow reactor (PFR) without particles. Minor dispersive effects due to the velocity boundary layer at the container walls is also neglected. The void regions are uniformly discretized using $N_z = 10$ elements in the axial direction.

1D/2D GRM is used for the packed-bed compartment, the features of which are adjusted to match the container geometry, bed morphology, and flowrates applied to the corresponding reference HD simulations.

An axial discretization of $N_z = 100$ elements, and, in the case of 2D GRM, a radial discretization of $N_\rho = 5$ elements is used. The column radius r_c is discretized into N_ρ radial zones ρ_w, bounded by lower and upper radii $[\rho_{w-\frac{1}{2}}, \rho_{w+\frac{1}{2}}]$, where $w \in \{1, \dots, N_\rho\}$. L represents the length of the packed-bed region of the column.

Equation 6.3 is applied to HD geometry and flow simulation results to obtain the corresponding reduced-order porosity, $\varepsilon_{c,w}$, and velocity, u_w, respectively for each radial zone ρ_w in the 2D GRM discretization scheme. Plots of reduced velocity and porosity for $N_\rho = 5$ are shown in comparison to a radial discretization of $N_\rho = 40$ with cubic interpolation in Figure 6.4c and Figure 6.4d.

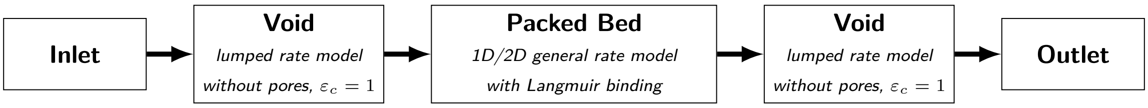

(a) Compartmentalized unit operation sequence in 1D and 2D GRM

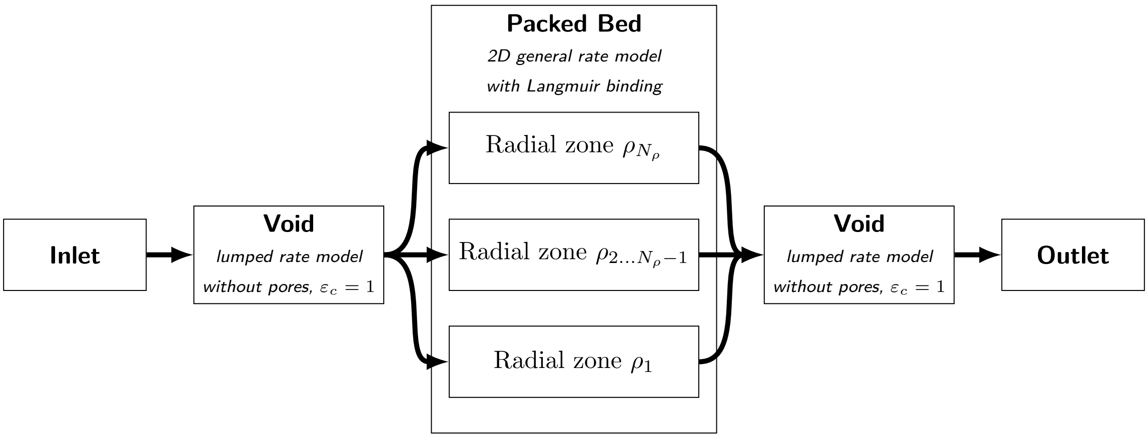

(b) Flow connectivity between unit operations in 2D GRM

Figure 6.3: Compartmentalization and flow connectivity in CADET.

$$u_w = \frac{1}{L} \int_{\rho_{w-\frac{1}{2}}}^{\rho_{w+\frac{1}{2}}} \int_0^{2\pi} \int_0^L u \, dV \qquad \text{in } \Omega_1 \tag{6.3a}$$

$$\varepsilon_{c,w} = \frac{1}{\pi \cdot (\rho^2_{w+\frac{1}{2}} - \rho^2_{w-\frac{1}{2}}) \cdot L} \int_{\rho_{w-\frac{1}{2}}}^{\rho_{w+\frac{1}{2}}} \int_0^{2\pi} \int_0^L dV \qquad \text{in } \Omega_1 \tag{6.3b}$$

In models that take into account the packing PSD, particle sizes are discretized into N_{bins} bins of equal size $\Delta r = \frac{r_{\max} - r_{\min}}{N_{\text{bins}}}$ using Equation 6.4.

$$B_k = \{ i \in \mathcal{P} : r_{\min} + k\Delta r \leq r_i < r_{\min} + (k+1)\Delta r \} \tag{6.4}$$

where B_k is the k^{th} bin with $k \in \{1, \ldots, N_{\text{bins}}\}$, and $\mathcal{P}$ is the set of all particles in the packed bed. $N_{\text{bins}} = 10$ for all ROMs with PSD in this work. The resulting histogram is shown in Figure 6.4a.

Particles are discretized into $N_{par} = 5$ elements that are radially concentric. The single-component Langmuir binding model is set up with parameters matching those of the HD

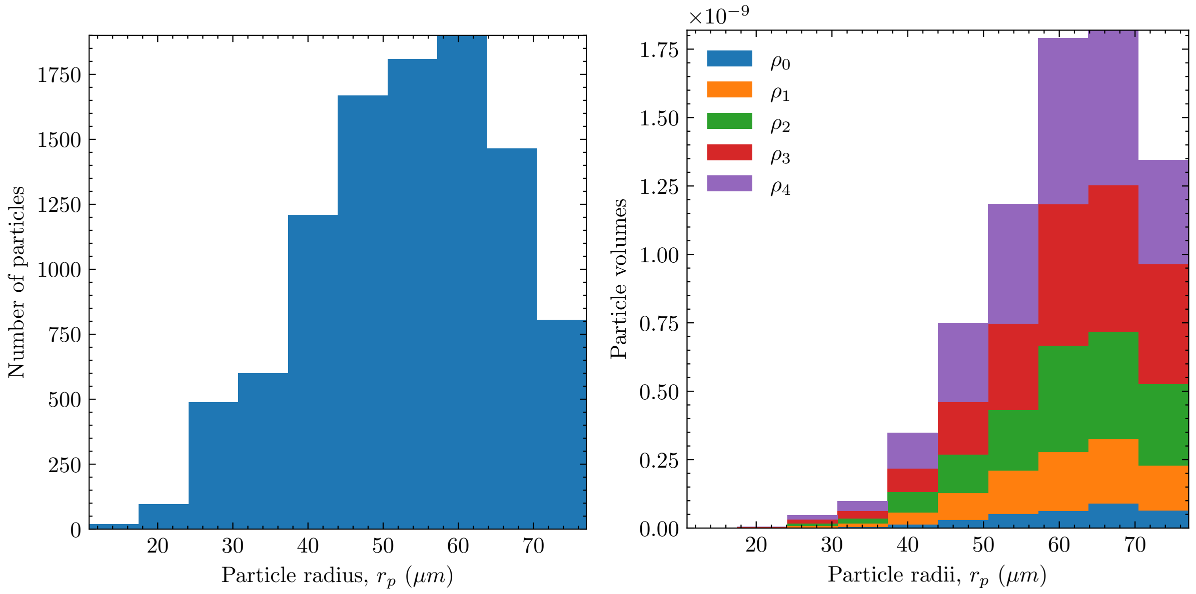

(a) PSD **(b)** Volume fractions

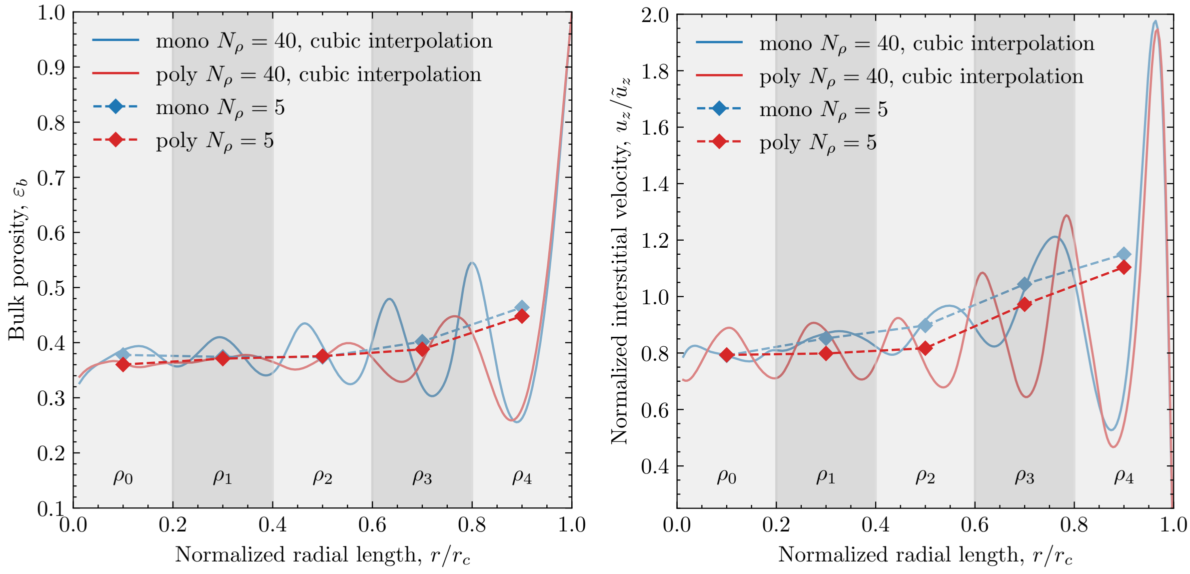

(c) Porosity profiles **(d)** Velocity profiles

Figure 6.4: Geometric inhomogeneities in HD simulated columns

simulations. As in the reference HD simulations, surface diffusion is not modeled.

Table 6.1 shows the pre-specified parameters for a 1D GRM representation of the monodisperse column used in this work.

Table 6.1: Fixed parameters in 1D GRM without PSD

Parameter	Value
General rate model	
Column length, L	$1.560 \times 10^{-2}\,\mathrm{m}$
Column radius, r_c	$5.01 \times 10^{-4}\,\mathrm{m}$
Particle radius, r_p	$4.999\,85 \times 10^{-5}\,\mathrm{m}$
Particle porosity, ε_p	0.75
Particle diffusion coefficient, D_p	$7.07 \times 10^{-11}\,\mathrm{m^2\,s^{-1}}$
Particle surface diffusion, D_s	$0.0\,\mathrm{m^2\,s^{-1}}$
Langmuir adsorption	
Adsorption coefficient, k_a	$1.144\,\mathrm{m^3\,mol^{-1}\,s^{-1}}$
Desorption coefficient, k_d	$2.0 \times 10^{-3}\,\mathrm{s^{-1}}$
Maximum binding capacity, $c^s_{\max}$	$4.88\,\mathrm{mol\,m^{-3}}$
Binding type	kinetic
Discretization	
Column axial discretization, N_z	100
Particle radial discretization. N_r	10

6.3 Parameter Estimation

Problem formulation

The parameter estimation problem that is central to the ROM calibration process may be formulated in the following way.

$$\widehat{\boldsymbol{\theta}} = \arg\min_{\boldsymbol{\theta}}(\boldsymbol{J}(\boldsymbol{\theta})) = \arg\min_{\boldsymbol{\theta}}(J_1(\boldsymbol{\theta}), \dots, J_k(\boldsymbol{\theta})) \tag{6.5}$$

where $\boldsymbol{\theta} = \{\theta_1, \dots, \theta_m\}$ is the set of parameters, and $\boldsymbol{J} = \{J_1, \dots, J_k\}$ are the objective functions to be minimized. Each objective function can be represented as a function composition $J = R(\Phi(\boldsymbol{\theta}), \overline{\Phi})$, where $\Phi(\boldsymbol{\theta})$ is the model output for a given $\boldsymbol{\theta}$, and $\overline{\Phi}$ is the reference or target output. Generally, one may consider that the symbol Φ represents a particular chosen objective metric (or, simply, objectives), i.e., a physical measure such as outlet concentration or solute mass that is dependent on specific input parameters, that also has reference values against which the parameter estimation is carried out. R is a residual operator or scoring function such as the root mean squared error function. The hat symbol, $\widehat{\cdot}$, is used to represent optimal state; $\widehat{\boldsymbol{\theta}}$ is the set of optimal parameters, and $\widehat{\Phi}$ represents the corresponding best fit objective metric.

In typical 1D GRM calibrations, the dispersion coefficient is estimated by fitting the model output for each objective to their corresponding reference data, where the reference data are typically experimentally calculated breakthrough curves or chromatograms.

In calibrations with one objective, the optimization procedure results in a single solution to the problem, assuming the objective function is continuous and, ideally, differentiable, the problem possesses a well-defined optimum, and the optimization algorithm itself is convergent and sufficiently balanced between exploration and exploitation of the search space. For multi-objective optimizations, a set of solutions whose objective function values span the so-called Pareto front, a multi-dimensional manifold in the objective space, is obtained. The Pareto front, $\mathscr{P}$, is defined by the Pareto-optimal set of solutions, $\boldsymbol{\theta}^{\mathscr{P}} = \{\tilde{\boldsymbol{\theta}}_1, \ldots, \tilde{\boldsymbol{\theta}}_n\}$, that represent different tradeoffs along the many individual objectives of the problem. Thus, an additional step, known as multi-criteria decision making, is necessary in order to select the best solution from the Pareto-optimal set based on the problem's context or another metric. In this work, a scalarized meta-residual based on the individual residual values $S(\boldsymbol{J}(\boldsymbol{\theta}))$ is calculated, which results in the optimal parameters, $\widehat{\boldsymbol{\theta}}$ after a minor post-processing step.

$$\widehat{\boldsymbol{\theta}} = \arg\min_{\boldsymbol{\theta}}(S(\boldsymbol{J}(\boldsymbol{\theta}^{\mathscr{P}}))) \tag{6.6}$$

Objectives and reference data

The range-normalized root mean square error (NRMSE, Equation 6.8) is used as scoring function, R, for every objective Φ in this work.

$$R(\mathbf{y}, \overline{\mathbf{y}}) = \frac{\sqrt{\frac{1}{n}\sum_{i=1}^{n}(\overline{y_i} - y_i)^2}}{\max(\overline{\mathbf{y}}) - \min(\overline{\mathbf{y}})} \tag{6.7}$$

where $n = \dim(\mathbf{y}) = \dim(\overline{\mathbf{y}})$.

This normalization effectively assigned identical weights to each objective, thereby eliminating any bias associated with differences in their original magnitude in the reference data.

In this work, solute masses in each radial zone are chosen as objectives, $\Phi = M_\kappa^w = M_\kappa^w(\boldsymbol{\theta})$. Thus, the residual value $\xi_\kappa^w = R(M_\kappa^w)$ can be fully described as

$$\xi_\kappa^w = \frac{\sqrt{\frac{1}{N_t}(\overline{M}_\kappa^w - M_\kappa^w)^2}}{\max(\overline{M}_\kappa^w) - \min(\overline{M}_\kappa^w)} \quad \forall \kappa \in \{b, p, s\}, \forall w \in \{1, \ldots, N_\rho\} \tag{6.8}$$

where N_t is the number of discretization in time, κ is the phase index, and w is the index of the radial zone.

Parameters

The axial dispersion coefficients D_{ax}^w, and radial dispersion coefficients D_ρ^w for every radial zone ρ_w, and a global film-diffusion coefficient k_f are considered as parameters in all the calibrations performed in this work. In other words, radial dependence of these parameters is considered. Particle-type-dependence, i.e., distinct parameter values for every bin in the PSD histogram, of the film-diffusion coefficient is not considered for the sake of simplicity.

Multi-criteria decision making

Multi-objective optimizations result in a set of optimal or near-optimal solutions that span a multi-dimensional surface in the objective space known as the Pareto front, which represents trade-offs between individual solutions for specific objectives. This span can be visualized for every objective in the calibration process, and is denoted in this work as $\langle M_\kappa^w \rangle$. It provides information about the range of the Pareto front in the objective space.

In order to find the best solution in the optimal set, the multiple residuals ξ_κ^w are scalarized using the root mean square (RMS) function as shown in Equation 6.9, and pick the solution with the least scalarized (meta-)residual $\tilde{\xi}$.

$$\tilde{\xi} = \sqrt{\frac{1}{N_\xi} \sum_\kappa \sum_{w=1}^{N_\rho} (\xi_\kappa^w)^2} \tag{6.9}$$

where $N_\xi = N_\Phi \cdot N_\rho$ is the number of total objectives, with N_Φ and N_ρ representing the number of phases and radial zones respectively considered in the calibration process.

The best fitting objectives $\widehat{M}_\kappa^w$ are selected such that they minimize $\tilde{\xi}$, i.e., $\widehat{M}_\kappa^w = \arg\min \tilde{\xi}$. The corresponding best-fit parameters are notated as $\widehat{D}_{\text{ax}}^w$, $\widehat{D}_\rho^w$, and $\widehat{k}_f$.

While it is also possible to directly use the scalarized metric as the only optimization objective, formulating the parameter estimation as a multi-objective problem results in the optimizer taking into account the individual sensitivities of every objective with respect to every parameter. Furthermore, multi-objective optimization leads to better exploration of the objective space, thus resulting in more comprehensive information for decision making.

The optimization itself is terminated upon convergence of the meta-residual and every parameter for the median and best individual solutions in every generation is manually verified. While limits can be placed upon the number of ROM evaluations or generations, allowing the optimizer to proceed by visual inspection of the meta-residual allows to refine the optimal solution set further until the parameters fully converge and patterns emerge.

Genetic Algorithms: UNSGA-III

Genetic algorithms (GAs) are a subclass of evolutionary optimization algorithms that take inspiration from biological processes such as natural selection, genetic reproduction, and mutation. Starting from a pool of initial solutions known as a population, GAs evaluate, filter, combine, and mutate individual solutions in the population to create a new generation of solutions. This iterative process continues through generations, gradually improving the population towards an optimal or near-optimal solution.

The operations applied to the population every generation are roughly described below.

Evaluation Individuals in the population are evaluated to obtain a score or residual for every objective function in the context of the optimization problem.

Selection Individuals are selected for creating offspring. This may be random selection, or based on some principles of elitism built upon the multi-dimensional residuals. This process might involve selecting some non-optimal solutions in order to avoid being trapped in local optima, leading to more diversity in solutions.

Crossover Features of the parent individuals selected from the previous step are combined to create offspring.

Mutation Features of an arbitrary subset of the population are mutated within the given bounds, typically in a random manner. Higher rates of mutation lead to exploration of the search space as opposed to its exploitation.

Survival A subset of the population is selected to survive, resulting in the creation of a new generation of the population of the prescribed size.

Genetic algorithms are widely used in a variety of fields due to their ability to handle complex, high-dimensional, and non-linear problems with multiple local optima. Due to the absence of dependencies in the evaluation phase, the residual for the entire population can be calculated completely independently, making the problem embarrassingly parallel.

NSGA-based algorithms (NSGA-II, and (U)NSGA-III) [69–71] use the concept of non-dominated sorting (NS) in the survival step. An individual is said to be non-dominated with respect to a second individual, if the second does not dominate the first in any objective. The overall population is sorted into several non-dominated fronts, where individuals on fronts with lower ranks dominate those on fronts with higher ranks. Individuals for the next generation's population are selected from these fronts in order of their ranks.

(U)NSGA-III [70, 71] additionally uses the concept of reference directions along with NS in order to select individuals from the last front that cannot entirely be used in the next generation due to exceeding the set population size. Individuals are selected based on their proximity to each of a set of predefined reference directions in order to select individuals on a given front that span a wide distribution. This ensures diversity in the population of the next generation.

UNSGA-III also uses the non-dominated sorting with reference directions in a tournament-based selection process for parent individuals in order to generate offspring. This added tournament pressure improves convergence. (U)NSGA-III is known to be able to handle many-objective ($n > 3$) optimization problems, whereas earlier versions such as NSGA-II struggled to maintain diversity in the population at higher dimensional objective spaces.

The reference directions themselves are created by generating reference points, and generating vectors the origin to these reference points. The reference points are generated based on the Riesz s-Energy method described in [72]. The Riesz s-Energy is defined for two particles ($\mathbf{z}^i$ and $\mathbf{z}^j$) in an s-dimensional space as

$$U(\mathbf{z}^i, \mathbf{z}^j) = \frac{1}{\left\|\mathbf{z}^i - \mathbf{z}^j\right\|^s}$$

For a many-body system, the energies are defined as a $\mathbf{Z}$ matrix as follows.

$$U(\mathbf{Z}) = \frac{1}{2} \sum_{i=1}^{n} \sum_{j=1 j \neq i}^{n} \frac{1}{\left\|\mathbf{z}^i - \mathbf{z}^j\right\|^s}, \quad \mathbf{Z} \in \mathbb{R}^{n \times M} \tag{6.10}$$

Finding the **Z** matrix that minimizes $U(\mathbf{Z})$ produces a well-spaced point distribution that corresponds to reference directions used in the calibration algorithms.

Simulated Binary Crossover (SBX) [73], where a probability distribution is applied around the parent solutions, is used to create offspring. A distribution index (η) controls the distribution's shape, with a higher value resulting in narrower distributions, and hence increased probability of the offspring's similarity to its parents. In this work, default values of $\eta = 30$ were used for all calibrations.

6.4 Implementation

A new chromatography ROM calibration tool, `chromoo`, was built for this work*. It uses `pymoo` as the underlying optimization library, and interfaces with `CADET-Core` to perform ROM evaluations. Several custom post-processing tools and scripts were also written to extract reference data for every solute phase from HD simulation results.

All the calibrations in this work were carried out using UNSGA-III. Objective functions were constructed using a range-normalized root mean square error (NRMSE) between the model output and reference data. Normalization of objectives was implemented to ensure that all objectives received equal weightage, thus preventing bias towards variables with inherently large values. Selection of decision and response variables, as well as reference data, was tailored to the particular requirements of each use case or modeling scenario. The parameter bounds used in the calibration procedure imposed no artificial restrictions on the actual range of possible solutions. In order to improve convergence, model parameters were logarithmically scaled and normalized within their respective bounds. Low discrepancy sequences that evenly span multi-dimensional spaces are known to enhance convergence in comparison to random initializations that can lead to clustering [74]. Thus, a Sobol sequence is used for population initializations in this study. A detailed ROM calibration workflow is given as a flowchart in Figure 6.5.

---

* https://zenodo.org/records/14876413

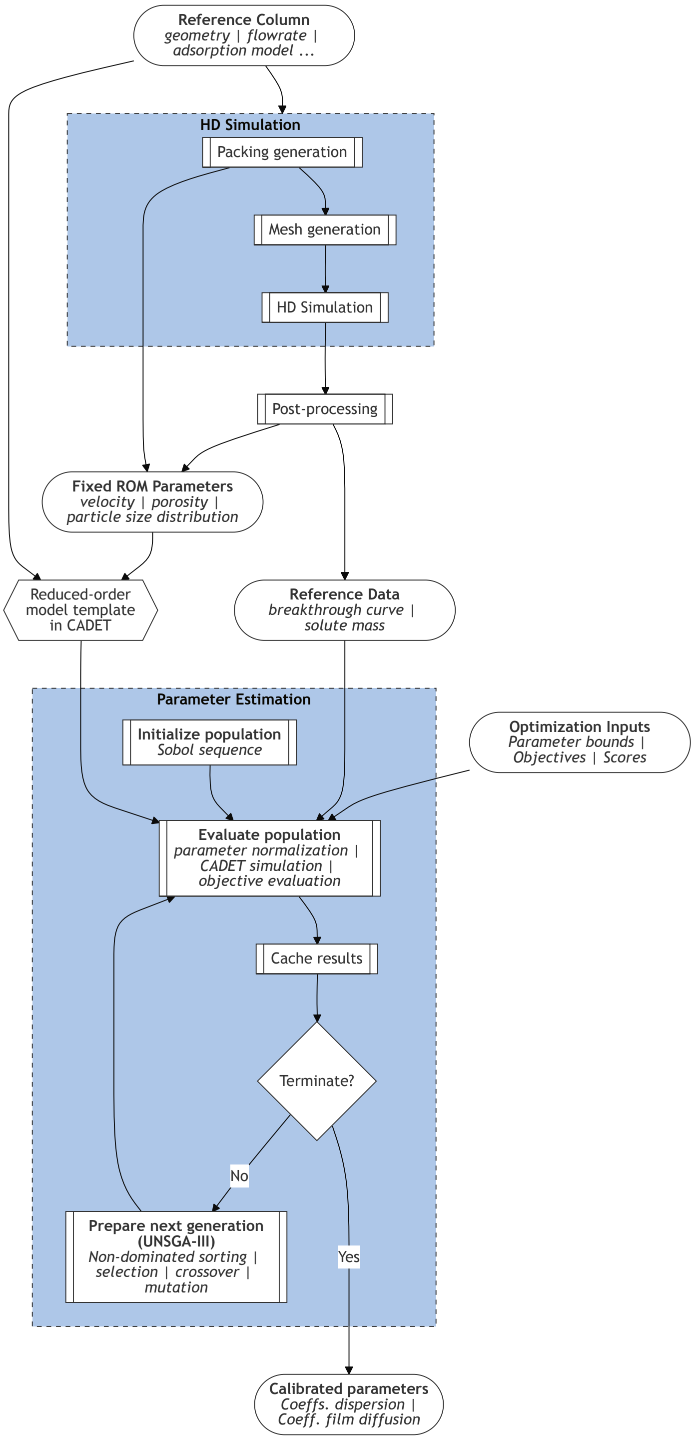

Figure 6.5: ROM calibration workflow as a detailed flowchart.

6.5 Conclusions

Advantages of HD results as a source of reference data in calibration of ROMs are discussed. A multi-objective reduced-order model calibration workflow applicable to both 1D and 2D ROMs using internal column states (solute masses) obtained from high-definition simulation results as reference data was developed.

Preliminary results showcasing the efficacy of solute mass curves over breakthrough curves are discussed. Applied techniques for reference data extraction from HD results, and configuration of ROMs are shown. The choice of objectives, residual scoring functions, and applied regularizations are discussed as well.

A new tool was implemented using the open-source optimization framework, `pymoo`, and the open-source ROM simulator `CADET-Core`.

ROM calibration results

7

7.1 Effect of polydispersity

In situations where a given packing's PSD is not known, it is common to assume that particles are all of constant size equal to the average particle size of the packing. As the packing PSD has a strong effect on the local packing density, i.e., column porosity, which in turn affects the flow field and resulting solute transport in the interstitial region, neglecting PSD is expected to show strong differences in calibrated model parameter values.

In this section, the LP column geometry and results are used as reference data to configure and calibrate two distinct ROMs: (1) GRM without PSD, and (2) GRM with PSD. D_{ax} and k_f are considered as calibration parameters for both models, with M_b as the objective. The ROM without PSD was configured with the average particle size, whereas the PSD from the reference column was discretized into $npartype = 10$ parts for the ROM with PSD. Both models are assumed to have the same column porosity values, resulting in the same packed-bed capacity. They differ in the packed-bed surface area that is not an explicit parameter, but nonetheless implicitly affects column features such as the thin-film boundary region at the particle surfaces that is modeled as a mass transfer resistance in the form of a finite film-diffusion coefficient in both ROMs.

Table 7.1: Effect of neglecting PSD on D_{ax} and k_f in 1D GRM

Packing type		Packed-bed surface area (m^2)	Axial dispersion D_{ax} ($\mathrm{m}^2\,\mathrm{s}^{-1}$)	Film diffusion k_f ($\mathrm{m\,s}^{-1}$)
HD	ROM			
Polydisperse	without PSD	4.09×10^{-4}	3.11×10^{-7}	4.40×10^{-6}
Polydisperse	with PSD	3.70×10^{-4}	3.30×10^{-7}	7.18×10^{-6}

The resulting calibration fit plot and parameters are shown in Table 7.1 and Figure 7.1 respectively. Both models are able to optimally fit the reference data. However, the resulting parameters show substantial disparity. The calculated packed-bed surface area showed a 10 % increase for the model without PSD in comparison to the model with PSD, which corresponds to a 37 % reduction in k_f and 5 % reduction in D_{ax}. With the increased bed surface area, the reduced values of the dispersion and film diffusion coefficients sufficed to model the given reference data. It must be noted that although the ROM without PSD was able to compensate for the assumption of monodispersity and optimally fit the given data, the resulting underlying calibrated model differs from that of the reference model,

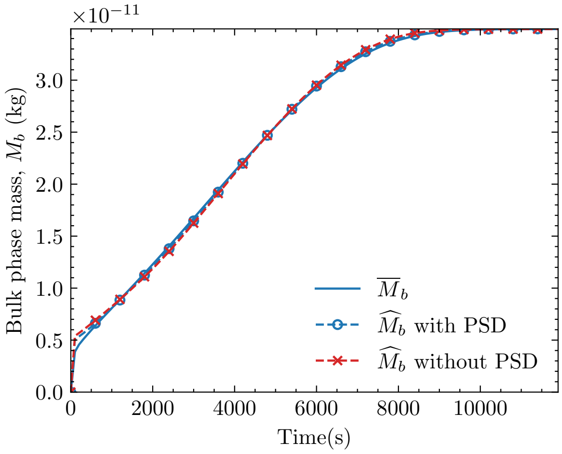

Figure 7.1: Optimal fits obtained while calibrating 1D GRM with and without PSD against bulk phase mass (M_b) for HD polydisperse packing

making it fragile to any changes in other model parameters, even those that have no effect on column dispersion and film-diffusion.

7.2 All phase masses as objectives

As the calibration parameters considered in this study,D_{ax}, D_p, and $k_f$are associated with phenomena that exist in the bulk domain, the bulk phase mass M_b may be considered a sufficient objective for such calibrations. However, using masses in other phases of the column, $M_p$and $M_s$allows the optimizer to take the mass balance across domains into account, resulting in solutions that are holistically optimal across phases for the entire column. This provides a complete picture of how the ROM fits the reference data described by the HD simulations, and potentially highlights disparities and shortcomings in both the ROM and HD model.

Two ROMs, one with and one without PSD, were calibrated with respect to reference data $\overline{M}_\kappa \forall \kappa \in \{b, p, s\}$ obtained from the columns LP and LM respectively. The resulting best fit plots in Figure 7.2 show the solution with the least scalarized error $\widehat{M}_\kappa$, the span of Pareto solutions$\langle M_\kappa \rangle$, and the reference objective data $\overline{M}_\kappa$for both model calibrations.

The model with PSD performs significantly better than the model without PSD, as is evident from the narrower Pareto spans as well as the better fit of the best solution for all objectives. Across objectives, the best fit $\widehat{M}_b$is indistinguishable from the reference solution $\overline{M}_b$, whereas small differences in $\widehat{M}_p$and $\widehat{M}_s$can be discerned with respect to their reference curves $\overline{M}_p$and $\overline{M}_s$respectively for both models. These minor discrepancies could be attributed to numerical errors in the simulations themselves, and to incompatibilities between the ROM and HD model that will be discussed in the upcoming section.

The sensitivities of individual objectives with respect to each parameter is shown in Figure 7.3, where each point in the plot represents an evaluation of the ROM simulation. Pareto optimal solutions are marked in red. As expected, M_b is highly sensitive to both model parameters, while $M_p$and $M_s$do not display such a sharp response for D_{ax}.

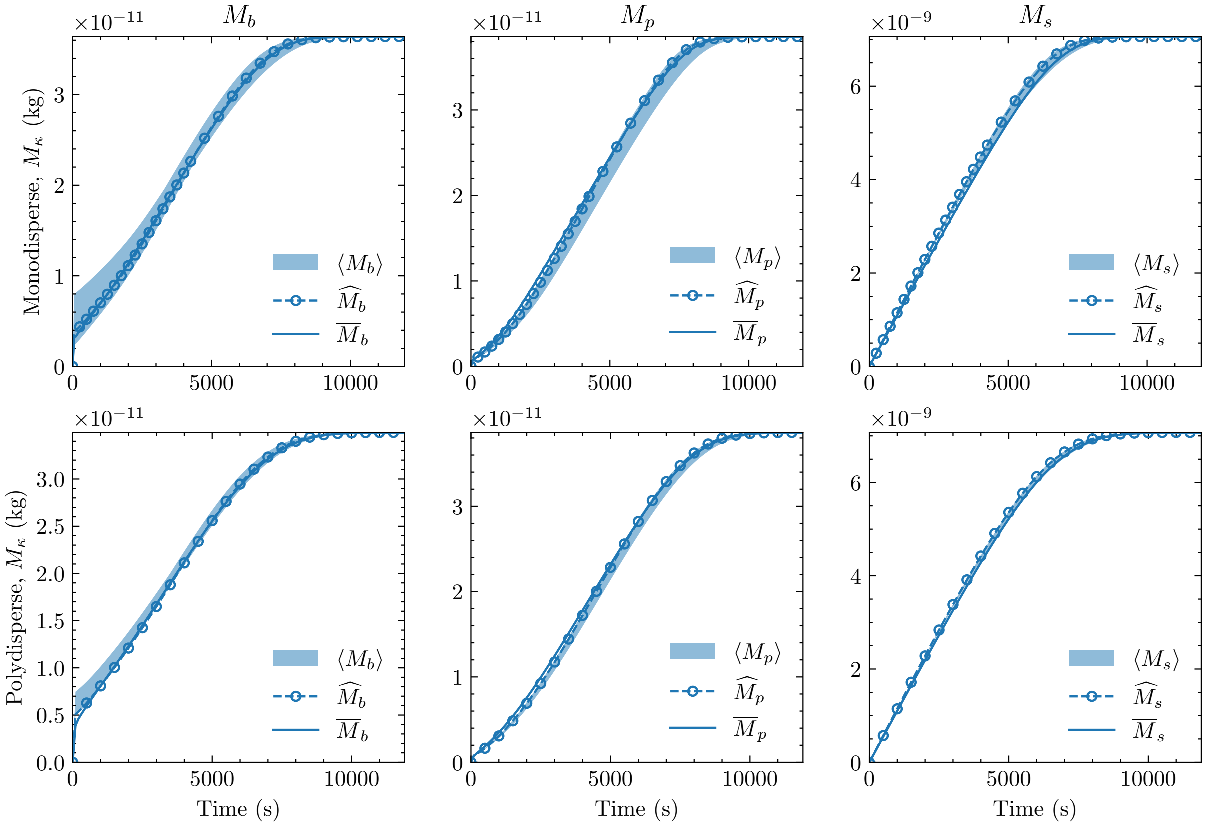

Figure 7.2: Plots showing the spans of Pareto front for the 1D GRM calibrations; without PSD for the monodisperse case (top), and with PSD for the polydisperse case (bottom).

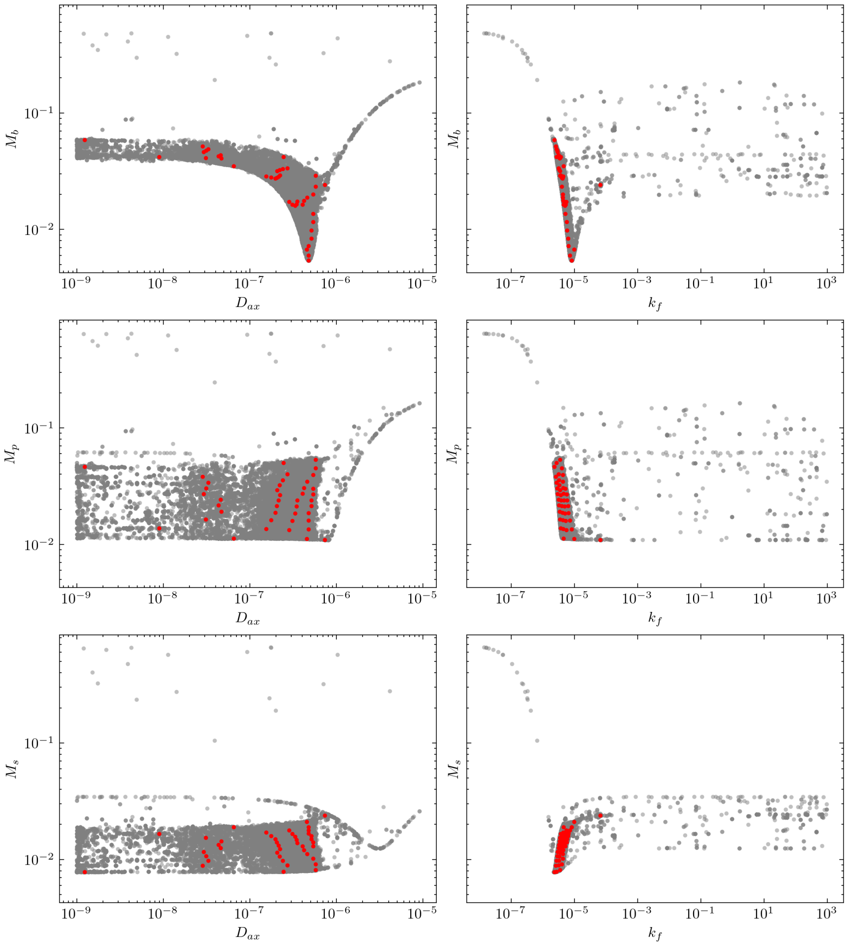

Figure 7.3: All combinations of parameters vs. objectives for all ROM evaluations in the 1D GRM calibration without PSD. Pareto optimal solutions are marked in red.

7.3 Radial inhomogeneities

Two dimensional ROMs were calibrated with respect to reference data obtained from their corresponding HD simulation results.

In contrast to examples showcased in previous sections with only $D_{\text{ax}}$and $k_f$as calibration parameters, calibrations of 2D GRM involves a multiplicative increase in the number of parameters due to the incorporation of the radial dimension when accounting for radial dependence of parameters.

The set of all parameters for the calibration of 2D GRM is given as

$$P = \{D_{\text{ax}}^w, D_\rho^w, k_f | w = 1, \dots, N_\rho\} \tag{7.1}$$

where $N_\rho = 5$ is the discretization of the column's radial dimension. Thus, the axial and radial dispersion coefficient is considered variable along the radial dimension. This configuration results in $2N_\rho + 1$parameters.

Similarly, the set of objectives, considering solute masses in all phases and all radial zones is given as

$$O = \{M_\kappa^w | \forall \kappa \in \{b, p, s\}, \forall w = 1, \ldots, N_\rho\} \tag{7.2}$$

which results in a total of $3N_\rho$ objectives.

Table 7.2 shows the best calibrated values of film diffusion coefficients for the models compared to three empirical correlations from [9]. Empirically calculated values of k_f for monodisperse and polydisperse geometries are shown to be close to identical. However, values of k_f obtained after ROM calibration, with the exception of the 2D monodisperse case, are generally varied and smaller in value.

Figure 7.4 shows the span of predictions for the Pareto front $\langle M_\kappa^w \rangle$, and the best prediction $\widehat{M}_\kappa^w$, against the corresponding reference curves, $\overline{M}_\kappa^w$, where $w \in \{1, \ldots, N_\rho\}$ and $\kappa \in \{b, p, s\}$ for all objectives.

Similar to the examples in the previous section, it is observed that ROMs with PSD generally performed better than their counterparts without PSD. This is attributed to the fact that the monodisperse packing exhibits fluctuations in local porosity due to wall effects even at the column center, whereas the fluctuations in the corresponding polydisperse packing are stabilized towards the column center. These oscillations violate the assumption of homogeneity within a radial zone for the 2D ROM, making it incompatible with the reference column.

Reducing the HD simulation results to generate reference data for a given 2D ROM involves applying the 2D radial discretization scheme onto the HD simulation results. This inevitably results in particles crossing the boundaries of radial zones. While the HD simulation considers such particles whole, the particle volume is appropriately divided across zones when configuring the 2D model. However, the 2D model does not account for the inherent coupling of such particles that are "split" across radial zones, leading to further discrepancies between the ROM and the HD model.

GRM with PSD performs slightly better in this regard as it can account for exact volume fractions and radii of such particles in each radial zone.

A possible solution to the problem of fluctuating porosity profiles is finer radial discretization. However, doing so would make radial zone widths smaller than the average particle size, further exacerbating the problem of particles split across radial zone boundaries, and violating another aspect of the homogeneity assumption in ROMs.

All in all, calibration of ROMs in case of columns with small column-to-particle diameter ratios, where wall effects are significant, is a matter of trade-offs due to incompatibilities in the fundamental assumptions inherent to reduced-order models. Nonetheless, models which are able to take into account the packing PSD are able to satisfactorily fit to the given reference data in the examples showcased in this study.

Table 7.2: Comparison of k_f values fitted using ROMs vs. empirical correlations

Packing type	ROM	Simulation fit	Wilson-Geankoplis	Kataoka	Penetration correlation
HD Mono	1D Mono	8.10×10^{-6}	1.25×10^{-5}	1.00×10^{-5}	1.74×10^{-5}
	2D Mono	1.36×10^{-5}			
HD Poly	1D Poly	6.85×10^{-6}	1.23×10^{-5}	9.75×10^{-6}	1.69×10^{-5}
	2D Poly	5.49×10^{-6}			

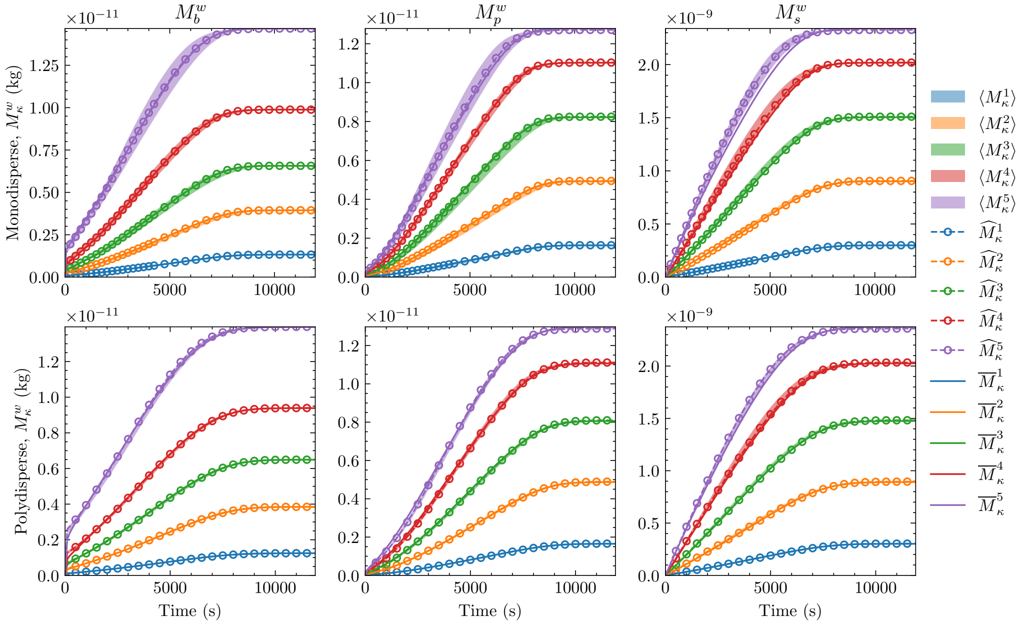

Figure 7.4: Spans of the Pareto front for the 2D GRM calibrations in the monodisperse (top) and polydisperse (bottom) cases

7.4 Conclusions

Calibration results highlight the significance of accounting for polydispersity in particle size distribution (PSD), as neglecting PSD leads to considerable discrepancies in key model parameters, such as axial dispersion and film diffusion coefficients. While both monodisperse and polydisperse ROMs can fit the reference data under optimal calibration, the model with PSD consistently yields more accurate and stable predictions across all objectives. This suggests that including PSD improves the physical fidelity of ROMs, particularly when accounting for variations in local column properties such as porosity and surface area. Moreover, the incorporation of additional phase masses, such as those in the particle and solid phases, contributes to a more holistic calibration approach, reducing the potential for model fragility and providing deeper insight into solute transport dynamics within the column. Although radial inhomogeneities and wall effects pose challenges for 2D ROMs, models incorporating PSD show significant improvement over their monodisperse counterparts. Nonetheless, calibration remains a trade-off, especially in cases where assumptions inherent to ROMs, such as homogeneity within radial zones, may be violated. These findings lay the groundwork for improving the accuracy and robustness of ROM calibrations in chromatographic systems, particularly those involving complex geometries and heterogeneous packing structures.

Periodic boundary conditions 8

8.1 Introduction

Packed-bed chromatography columns for analytical and preparative applications in experimental and production settings are found in a wide range of configurations with respect to the confinement geometry, the packed-bed morphology, and the operating conditions that are applied to the column. In high-performance liquid chromatography (HPLC), standard columns come in sizes of 4.6 mm internal diameter (i.d.), with smaller variants such as 3.0 mm and 2.1 mm i.d. columns becoming increasingly common. In other applications, microbore columns generally have values of 1.0 mm, whereas capillary columns can have even smaller internal diameters between 10–100 µm which are used for highly sensitive analyses with low sample volumes.

Thinner columns are generally preferred in instances where solvent and solute consumption is to be limited. Columns with smaller widths also have better heat dissipation, temperature homogeneity, and improved compatibility with mass spectrometry. This reduction in column volumes also necessitates tighter constraints on the extra-column volume of the equipment.

Typical column lengths range from 30–250 mm depending on the application.

The column-to-particle diameter ratio also plays a strong role in the column's performance. Conventional HPLC columns typically have d_c/d_prange from 20 to 100. In microbore and capillary columns, this diameter ratio can approach a value of 10. Larger diameter ratios are generally preferred in order to improve efficiency and reduce band broadening due to wall effects in confined packings. However, larger diameter ratios also result in larger pressure drops which might not be favourable in certain circumstances.

As demonstrated in previous chapters, HD simulations can serve as a powerful tool in modeling interstitial dispersion and thin-film boundary layer resistance in high fidelity, enabling its use as a source of reference data in the calibration of reduced-order models. However, the large-scale columns with approximately 10 000 particles simulated in this work are still orders of magnitude too small in comparison to existing HPLC columns. The simulated column i.d. was 1 mm and the diameter ratio $d_c/d_p = 10$ with a length of 16 mm.

In order to approach the scales of HPLC, the column diameter is to be scaled by a factor of 2–4, and column length is to be scaled by 2–15 times the current value. Implementing such a modification would necessitate profound and extensive changes across the entire toolchain. Specifically, it would require reengineering at multiple levels of the system architecture, including foundational libraries and dependencies, intermediate data and mesh processing tools, and high-level user interfaces. Specifically, it requires careful consideration and refactoring of deep-seated assumptions built into existing code, while accounting for other technical constraints such as integer overflows and memory and compute limits across the entire toolchain.

Unconfined simulations of packed-bed chromatography using periodic packings and boundary conditions is an alternative approach to simulating wider columns that do not exhibit wall effects. This approach still requires substantial modifications to existing tools in the workflow. However, it results in a more efficient use of compute resources in comparison to a direct scale-up of the column geometry.

8.2 Simulation Workflow

The workflow detailed for HD simulations with confined packings in chapter 4 is also applicable to unconfined cases. However, as only cylindrically-confined geometries were pre-generated for the previous thin-column simulations, periodic packings were required to be newly generated for this work. Furthermore, updates to the mesh generation tool were necessary in order to handle periodic geometries and meshes. XNS itself also required updates to re-implement periodic boundary conditions for this work. These updates to the workflow are described in this section in detail.

Packing Generation

As opposed to the previously-used cylindrically-confined random packings, unconfined packings are required to be periodic with respect to a given set of cuboidal boundaries. The periodic packings used in this chapter were generated based on the workflow outlined in [75], using the corresponding open-source tool developed in that work*. The workflow constitutes the application of the following algorithms in sequence:

- Force-Biased Algorithm (FBA),

---

* https://zenodo.org/records/580324

- Lubachevsky-Stillinger (LS) Algorithm, and
- Modified Lubachevsky-Stillinger Algorithm, also known as Lubachevsky-Stillinger Algorithm with Gradual Densification (LSGD).

The force-biased algorithm (FBA) [50] is a packing generation method that iteratively improves the spatial arrangement of particles by applying artificial forces to resolve overlaps and reduce local density inhomogeneities. Spheres are randomly initialized with inner and outer diameters. In each iteration, overlapping particles are displaced along the direction of the net force exerted by their neighbors, with the magnitude of displacement typically scaled to avoid excessive perturbation. Concurrently, the outer diameter of all particles is gradually decreased based on a contraction rate parameter. The algorithm proceeds until a predefined convergence criterion is met, such as the elimination of overlaps or the attainment of a target packing density. FBA is particularly effective for generating initial configurations with moderate densities (e.g., packing fractions between 0.4 and 0.6), which can then serve as starting points for more refined densification algorithms.

The Lubachevsky–Stillinger (LS) [51] algorithm is a dynamic, event-driven molecular dynamics approach for generating dense packings of hard spheres. The process begins by assigning velocities to an initial non-overlapping configuration of spheres. As the simulation progresses, the spheres undergo elastic collisions while simultaneously expanding at a constant growth rate, which is a key parameter controlling the evolution of the system. As the system evolves, the increasing particle sizes lead to progressive densification until jamming or a desired packing fraction is reached. The LS algorithm is capable of producing both amorphous and partially ordered structures depending on the growth rate, with slower rates typically yielding higher final densities and more ordered configurations. The LS algorithm is widely used due to its efficiency and ability to generate packings representative of maximally random jammed states.

The standard LS algorithm for fast compressions terminates prematurely due to excess non-equilibrium pressure. Applying slow compressions to unjammed packings results in almost jammed configurations with higher densities than the closest jammed configurations. A modified Lubachevsky-Stillinger algorithm [75] initially applies a faster compression rate, which is decreased (typically halved) when the reduced pressure of the system reaches a set threshold. The algorithm can be terminated when the contraction rate reaches a certain lower bound. The modified approach is particularly advantageous in producing high-density disordered packings and can be tailored to accommodate polydisperse or non-spherical particles.

Particle centers for a monodisperse periodic packing with 1000 particles generated using this workflow is shown in Figure 8.1. The generated packing is periodic along all 3 axes. The packing generation procedure is initialized by providing a desired particle size distribution. The `packing-generation` tool only ensures that the final sizes of particles is proportional to the desired values. For the monodisperse case, the target diameter of particles are set to 1.0. The cubic periodic confinement domain is initialized with a side of 10 units. In this case, the resulting particle diameters were 1.07 units. A post-scaling of 1×10^{-4} was applied to the packing in order to ensure similarity in scales to previous confined packings, resulting in particle diameters of 0.107 mm.

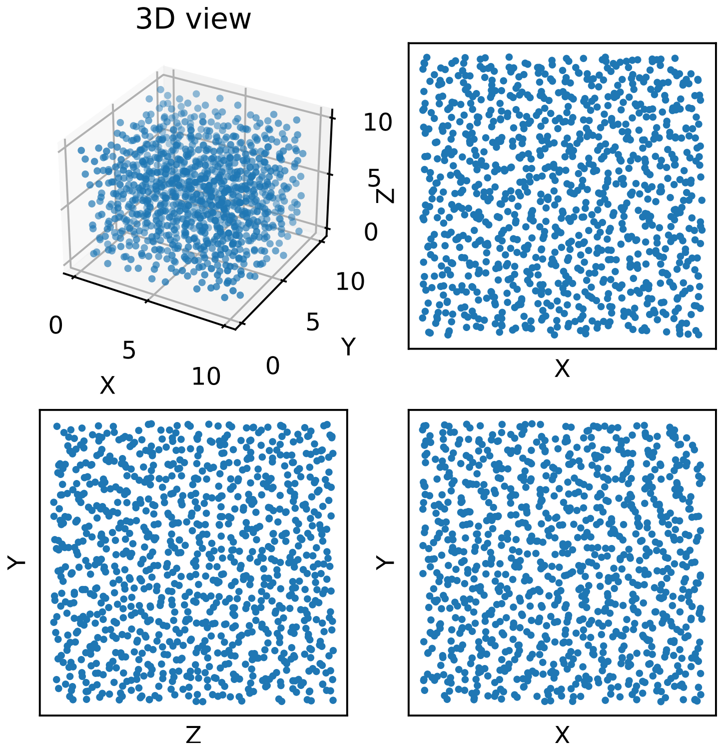

Figure 8.1: Spatial distribution of the coordinates of the particle centers

Geometry preparation and mesh generation

The generated periodic packing must be converted into a fully periodic geometric domain before it can be decomposed into a suitable periodic mesh. This is done by appropriately replicating particles that cross the predefined periodic boundaries, and clipping them at said boundaries. Particular attention must be paid to the case where a particle crosses multiple periodic boundaries, such as near corners. Particles in such cases must also be replicated across the diagonal. Figure 8.2 illustrates this boundary treatment using two particles that cross periodic boundaries at an edge and a corner respectively. Two algorithms, `VolumeCut` and `PlaneCut`, that handle particle replication are given in algorithm 1.

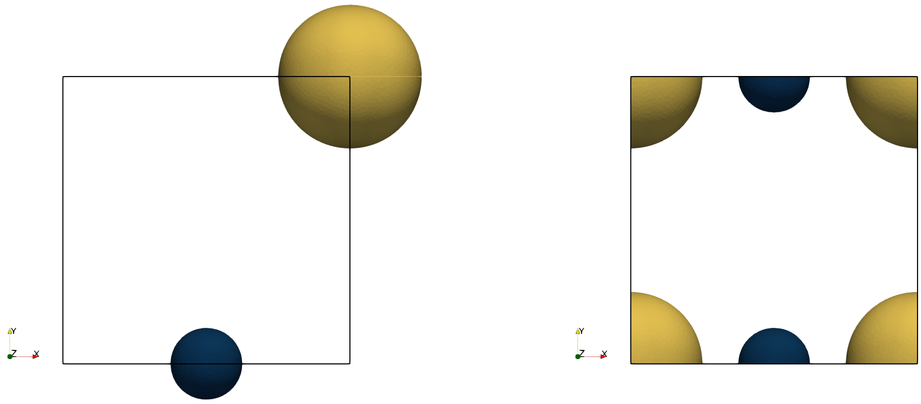

(a) Initial configuration in 2D. **(b)** Post replication and fragmentation.

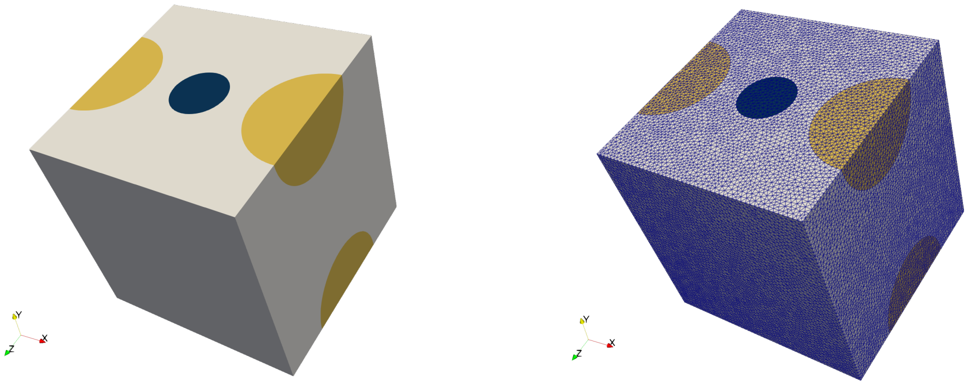

(c) Prepared geometry in 3D. **(d)** Generated mesh.

Figure 8.2: Illustration of handling of particles intersecting with XY-periodic boundaries. Such particles are mirrored to opposing boundaries and fragmented. Notably, particles intersecting multiple boundaries (yellow) are additionally mirrored across the diagonal.

The existing mesh generation code in `pymesh` was extended to handle cuboidal containers with generic periodicity in x, y, and z directions. A periodic geometry representation of the packing is generated based on the `VolumeCut` or `PlaneCut` algorithms, after which it is ensured that surfaces on either sides of prescribed periodic boundaries are geometrically consistent. Next, matching pairs of surfaces along with a corresponding affine transformation matrix are forwarded to `GMSH`, which generates the final periodic mesh.

Although it is possible to generate fully periodic packings and meshes with periodicity along all three axes, only lateral double-periodicity (i.e., along X and Y axes) is considered in this study as separation in chromatography columns occurs along its length. This configuration also allows drawing comparisons between laterally-unconfined periodic simulations and existing cylindrically-confined simulations, which in turn supports studying dispersion and film-diffusion in the presence and absence of wall-effects.

Algorithm 1: Algorithms for replicating particles crossing periodic boundaries.

Data: Initial packed-bed particle parameters, *particles*
Data: Periodic confinement parameters, *container*
Result: Updated packed-bed with replicated particles, *particles*

```
Function VolumeCut:
    containerDim ← Container dimensions ($dx$, $dy$, $dz$)
    cutParticles ← Cut all particles volumes with container volume
    for cutParticle in cutParticles do
        normals ← Calculate normals for all cut surfaces
        normals ← Extend normals combinatorially // $[n_x, n_y] \rightarrow [n_x, n_y, n_{xy}]$
        origParticle ← Find original particle corresponding to cutParticle
        for normal in normals do
            newParticle ← translated copy of origParticle by normal · containerDim
            particles ← particles ∪ newParticle
    return particles;
Function PlaneCut:
    containerDim ← Container dimensions ($dx$, $dy$, $dz$)
    cutPlanes ← Container faces
    for cutPlane in cutPlanes do
        splitParticles ← Fragment particles in intersection particles ∩ cutPlane
        accumulate splitParticles
    for splitParticle in splitParticles do
        normals ← Calculate normals for all cut surfaces
        normal ← Merge normals // $[n_x, n_y] \rightarrow [n_{xy}]$
        newParticle ← translated copy of origParticle by normal · containerDim
        particles ← particles ∪ newParticle
    return particles;
```

Periodicity Handling in XNS

The implementation of periodic boundary conditions in XNS was updated. However, major limitations of the MIXD format regarding double periodicity were encountered in the preliminary tests and validation cases. Specifically, the existing `mprd` file format only handles one-to-one nodal correspondence when applying periodic boundary conditions. While this is sufficient in handling single-periodicity in either x- or y-directions, it results in only one direction of periodicity being applied at corner and edge nodes of the computational domain, leading to a loss of conservation.

Further work will involve tailored updates to existing code and the `mprd` file format in order to correctly account for the double periodicity. This is, however, outside the scope of the present work, and will be addressed in the next phase of the project. Results of preliminary simulations with double-periodicity, shown in the upcoming section, are nonetheless useful in a qualitative manner.

Validation via block-swapping

Similar to a unit cell in a lattice structure, the periodic domain models an infinitely-wide effective domain that is formed out of seamless repetitions of itself connected at the boundaries. The block-swap approach for simulation validation exploits this inherent self-similarity in periodic geometries and solutions by decomposing the domain into blocks as shown in Figure 8.3. The green shaded region represents the original column decomposed into 2×2 blocks arranged in a counterclockwise manner. Repetitions of this domain are shown to the left, top, and top-left of the original domain. By nature of the double-periodicity, the region shaded in light-blue with the block sequence 3-4-1-2 must represent the domain (and solution) exactly identical to the original periodic domain with the block sequence 1-2-3-4.

In practice, the new configuration is achieved by simply subdividing the simulation domain into such blocks, and rearranging them appropriately. This is shown in Figure 8.4. Inner surfaces become outer surfaces and vice-versa through this process.

Simulations performed in the original and the block-swapped domains are theoretically identical. In practice, minor discrepancies due to numerical error are tolerated. This technique has proven instrumental in detecting configuration issues with boundary condition assignment. A misconfigured simulation of a double-periodic packing, where no-slip boundary is enforced on lateral surfaces, is provided as an example in Figure 8.5.

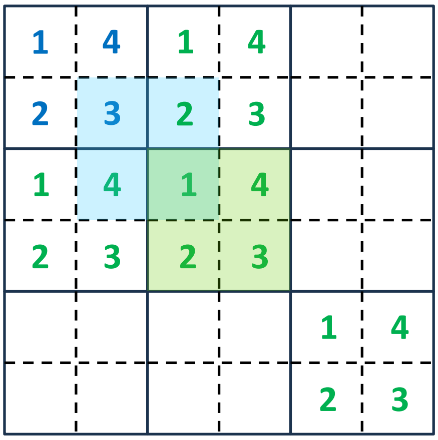

Figure 8.3: Fundamental diagram of the block-swap approach

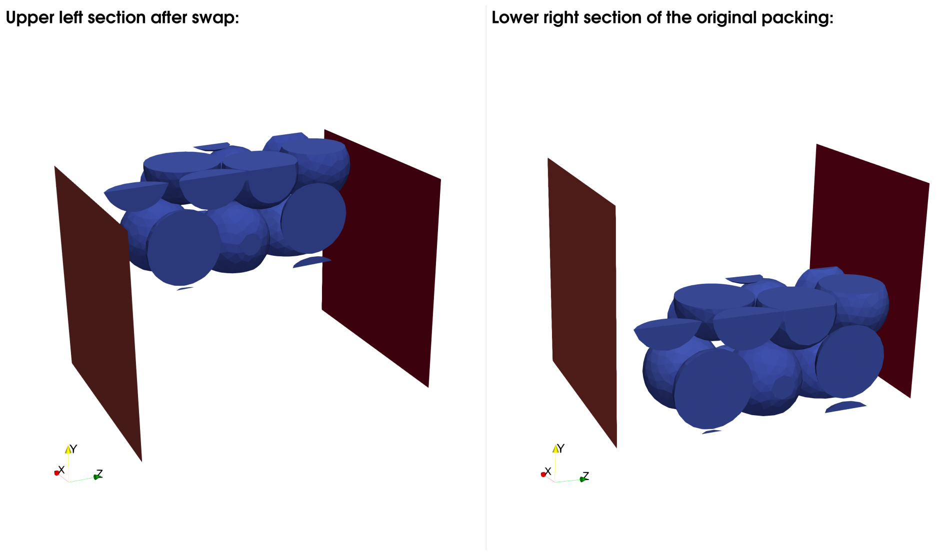
Upper left section after swap:

Lower right section of the original packing:

Figure 8.4: Block-swap approach for double-periodicity validation

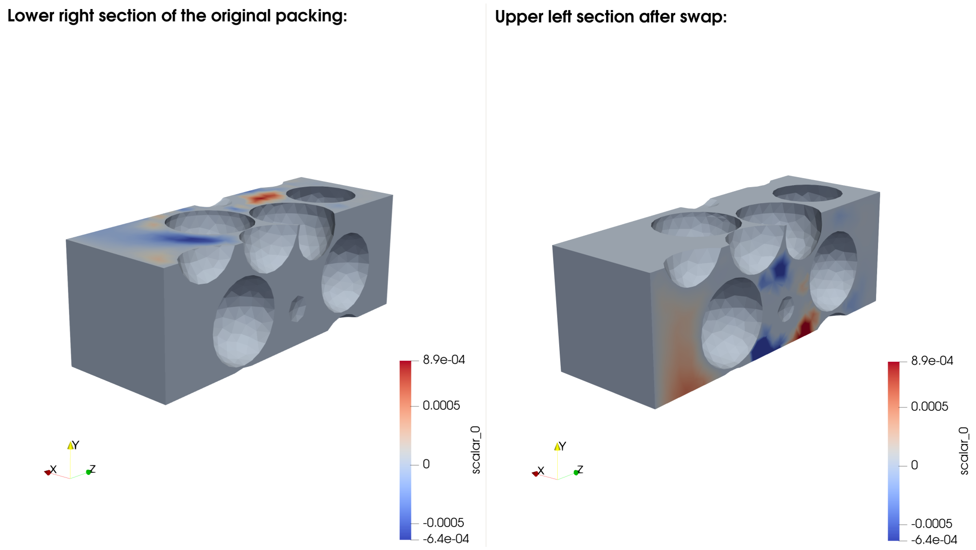
Lower right section of the original packing:

Upper left section after swap:

Figure 8.5: Application of the block-swap validation method on a misconfigured test case showing discrepancy in u_x on outer surfaces.

8.3 Preliminary Results

Test cases at small and large scales with approximately 1000–10 000 particles were set up to measure and ensure consistency in the periodic geometry, mesh, and solution. Results of these preliminary simulations are presented in the following sections in a qualitative manner.

Case Study

A short column with 1000 monodisperse particles is generated with void spaces of $2d_p$ on either end of the column, where d_p is the particle diameter. The prepared short column packing after the application of the `VolumeCut` algorithm to generate periodic lateral surfaces is shown alongside the full column in Figure 8.6. Particle sizes are set identical to the monodisperse confined case, $d_p = 1 \times 10^{-4} m$, and column width is similarly $10d_p$.

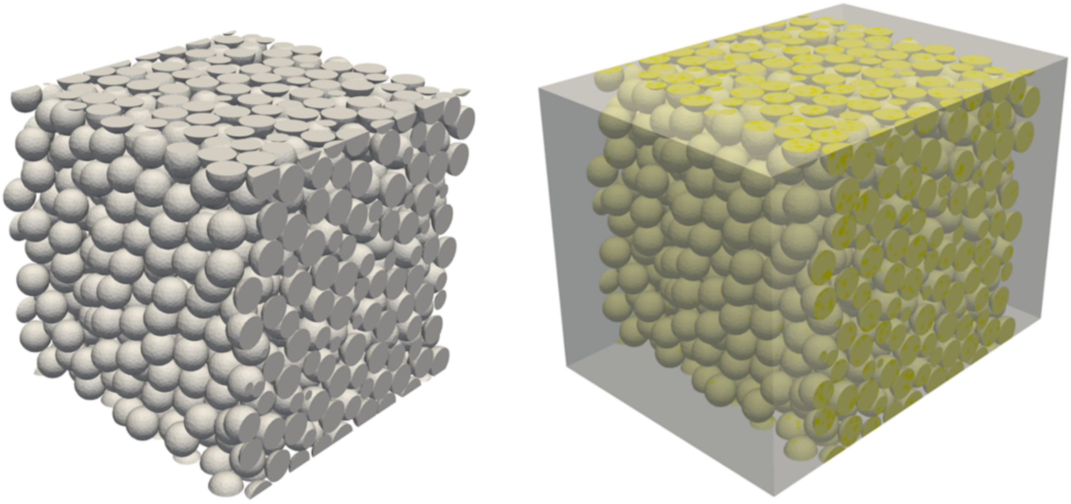

(a) Laterally periodic packed-bed geometry **(b)** Full column

Figure 8.6: Geometric representation of an unconfined small monodisperse column

A uniform mesh with element size of 0.06, corresponding to the medium element size utilized in the confined packing simulations is applied to the geometry. The resulting periodic packed-bed and interstitial meshes are shown in Figure 8.7.

Long columns of unconfined periodic packings were also generated to match the length of the LM unconfined packing geometry. However, due to differences in cross-section shapes, the total geometrical volume of the column and, hence, the total number of mesh elements in the periodic case is larger than that in the non-periodic case of identical width.

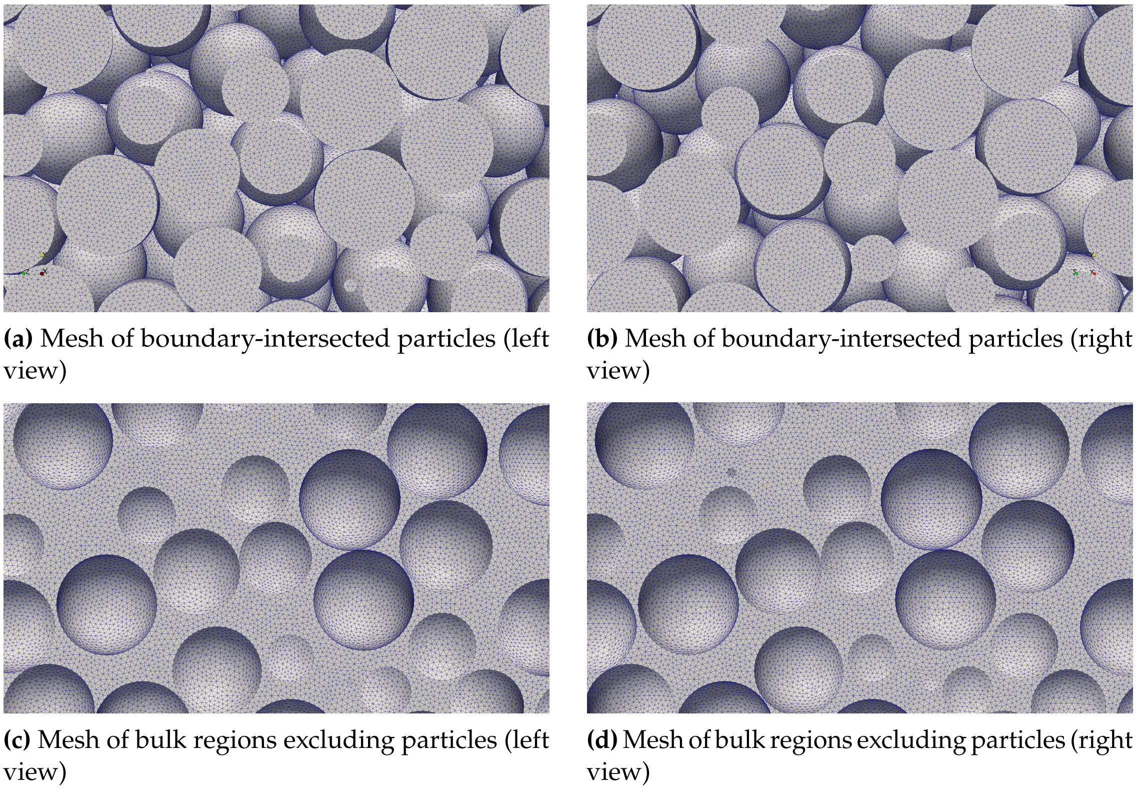

(a) Mesh of boundary-intersected particles (left view)

(b) Mesh of boundary-intersected particles (right view)

(c) Mesh of bulk regions excluding particles (left view)

(d) Mesh of bulk regions excluding particles (right view)

Figure 8.7: Magnified periodic meshes of monodisperse packings

In order to sidestep current limitations in the number of elements that are able to be simulated, the column width in this case was restricted to $8d_p$, resulting in 10 240 particles. Averaged porosity profiles for the x and y directions for the long column are shown in Figure 8.8. As opposed to the porosity profiles in columns of similar sizes with confined packings, no oscillations due to geometric wall effects are observed.

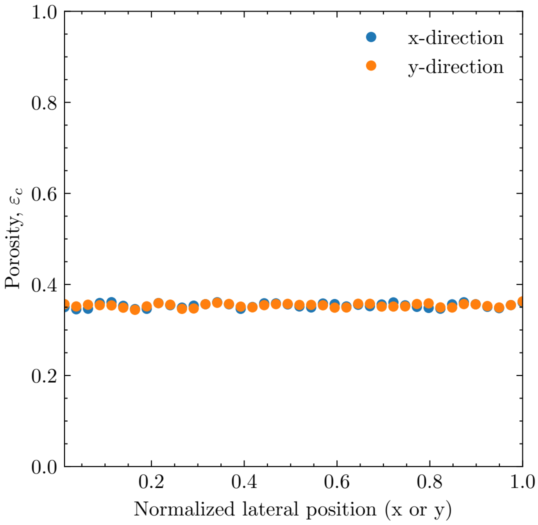

Figure 8.8: Porosity profile in large-scale periodic packing is devoid of geometric wall effects.

Fluid flow simulation

The flow simulation was configured with identical parameters to the cylindrical confinement case with the exception of the treatment of periodic boundaries. In the absence of geometric wall effects due to solid container boundaries, the radial porosity and velocity profiles are homogeneous within the packed bed. This homogenization of the porosity profile, resulting from the lack of interstitial channels at the walls, also results in the homogenization of the axially-averaged velocity profile. However, local velocity is still highly non-linear in interstitial pockets, reaching peaks of $6.8 \times 10^{-3}\,\mathrm{m\,s^{-1}}$. Visualizations of axial velocity and pressure are shown in Figure 8.9.

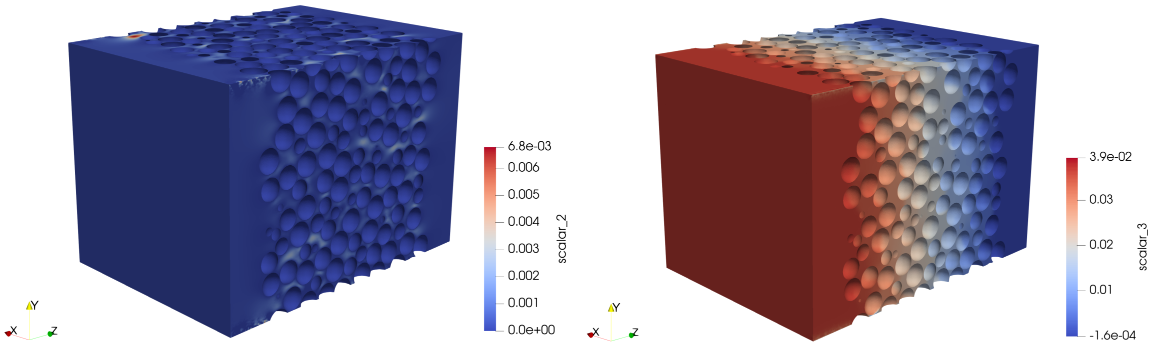

(a) Axial velocity distribution **(b)** Pressure field distribution

Figure 8.9: Profiles of axial velocity and pressure in the small monodisperse column

Mass transport and adsorption simulation

Concentration profiles in the liquid (c^b in Ω_1, and c^p in Ω_2) and solid (c^s in Ω_2) phases for the short column simulation are shown in Figure 8.10 and Figure 8.11. In the absence of channeling due to wall effects, it is observed that tortuousity in flow and transport create locally non-uniform concentration fields across particle surfaces throughout the entire packed bed, leading to non-concentric loading for all particles. In other words, although the homogeneity in porosity, velocity, and average bulk phase concentration fronts conforms with the assumptions of existing reduced-order models of chromatography, the inhomogeneity in particle loading that is evident in unconfined HD simulations cannot be modeled directly by ROMs.

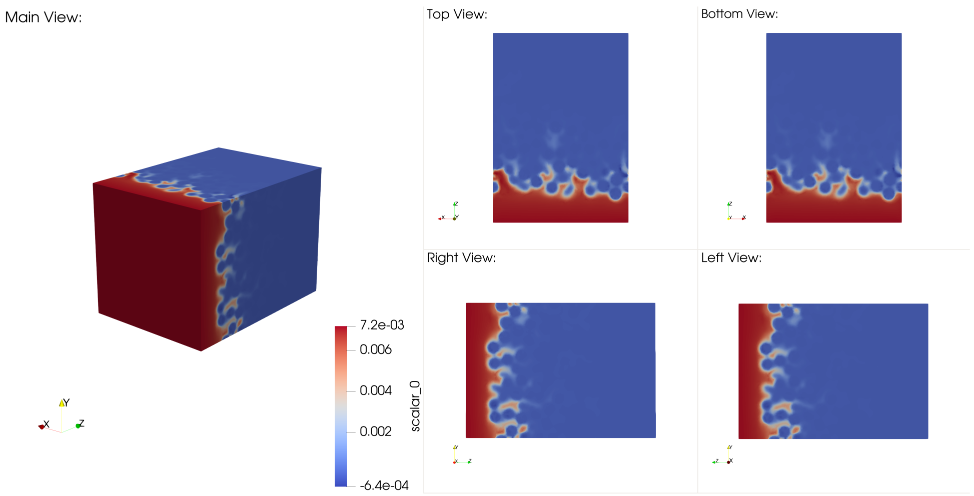

(a) Liquid concentration at $t \approx 100s$

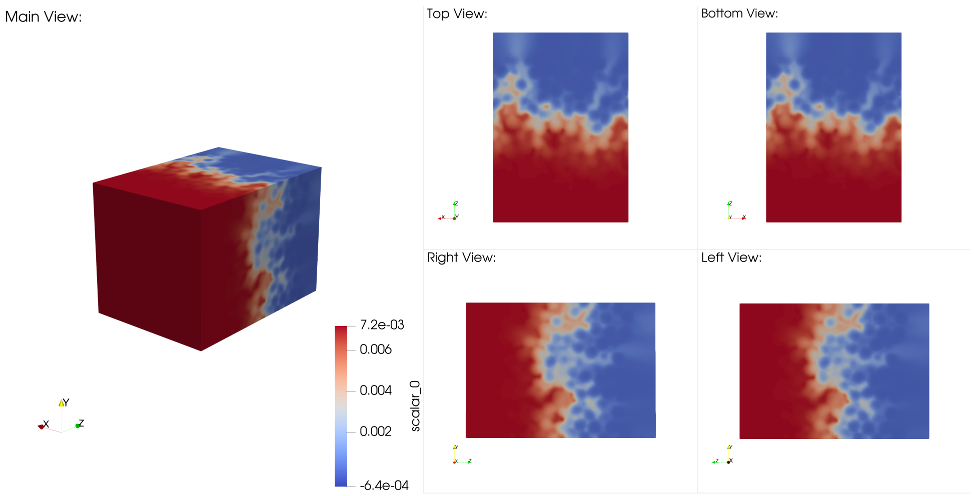

(b) Liquid concentration at $t \approx 8000s$

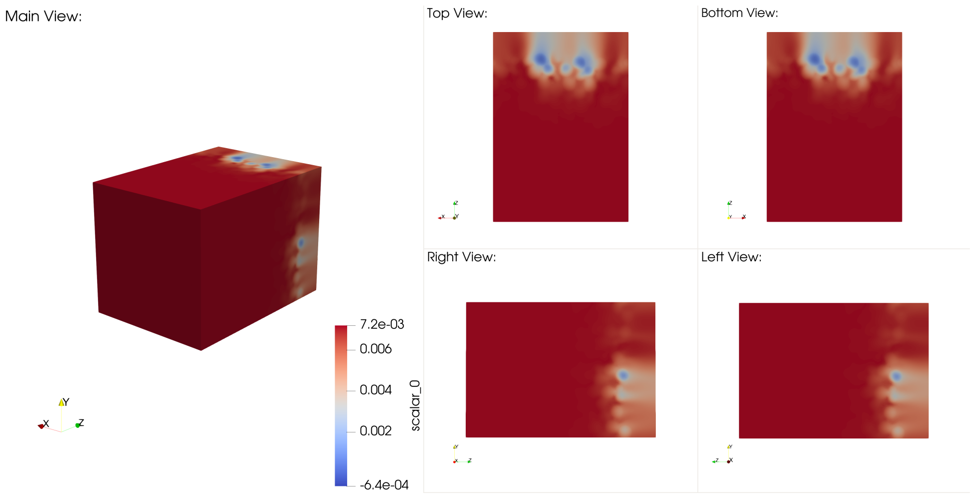

(c) Liquid concentration at $t \approx 16000s$

Figure 8.10: Profiles of liquid concentration in the small monodisperse column at different times. No wall effects are observed. Concentration front is locally tortuous, while progressing evenly along the column.

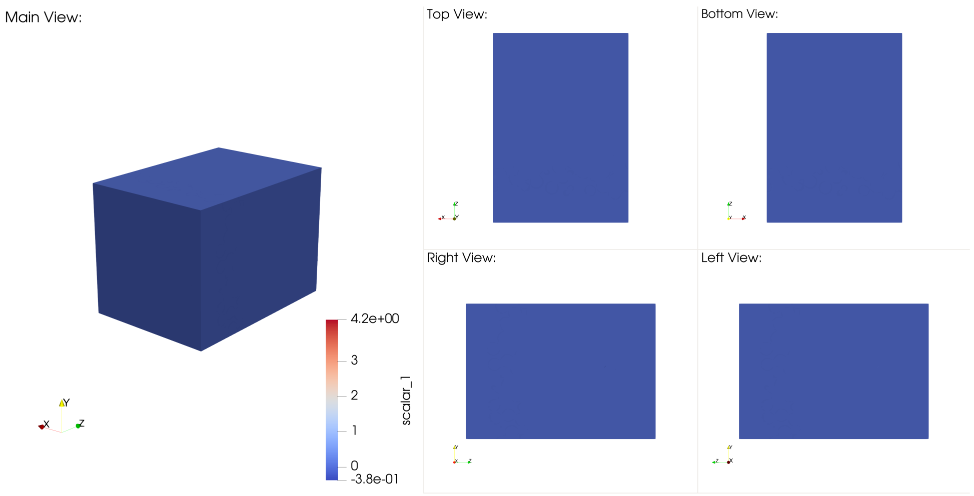

(a) Solid concentration at $t \approx 100s$

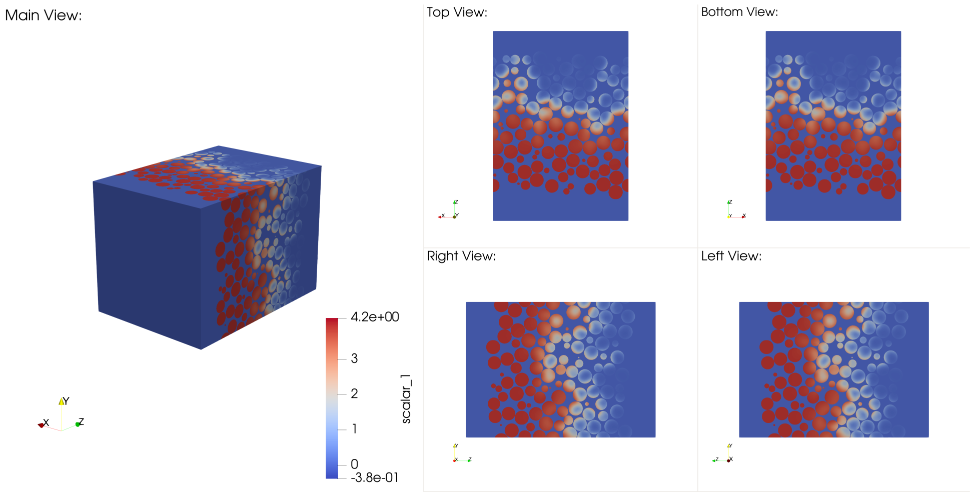

(b) Solid concentration at $t \approx 8000s$

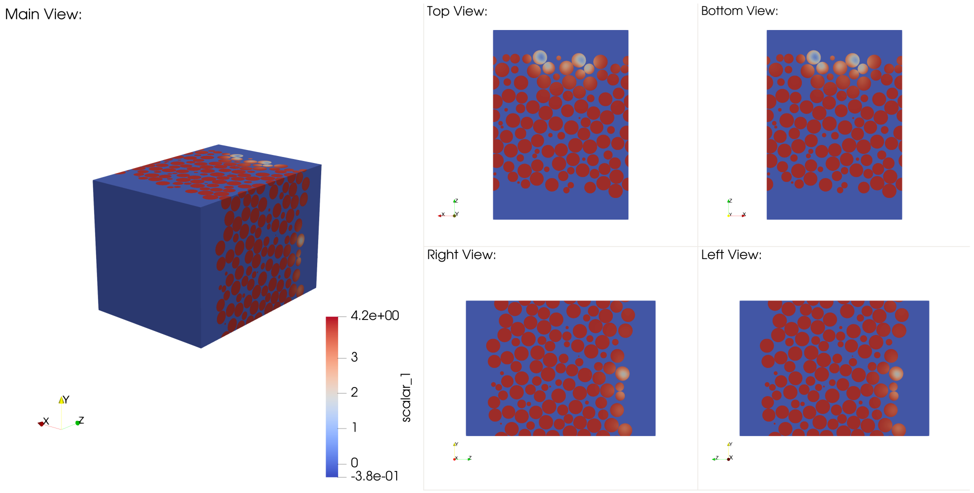

(c) Solid concentration at $t \approx 16000s$

Figure 8.11: Profiles of solid concentration in the small monodisperse column at different times. All particles are loaded asymmetrically due to locally tortuous concentration front in the bulk region.

Large scale simulations

Concentration profiles in the liquid (c^b in Ω_1, and c^p in Ω_2) and solid (c^s in Ω_2) phases for the long column simulation are shown in Figure 8.12. The laterally constant local porosity profile results in a constant rate of axial dispersion across the cross section in the absence of geometric wall effects. Results show a concentration front that is relatively even across the cross-section geometry, as opposed to the inverted parabolic concentration front in confined packing simulations.

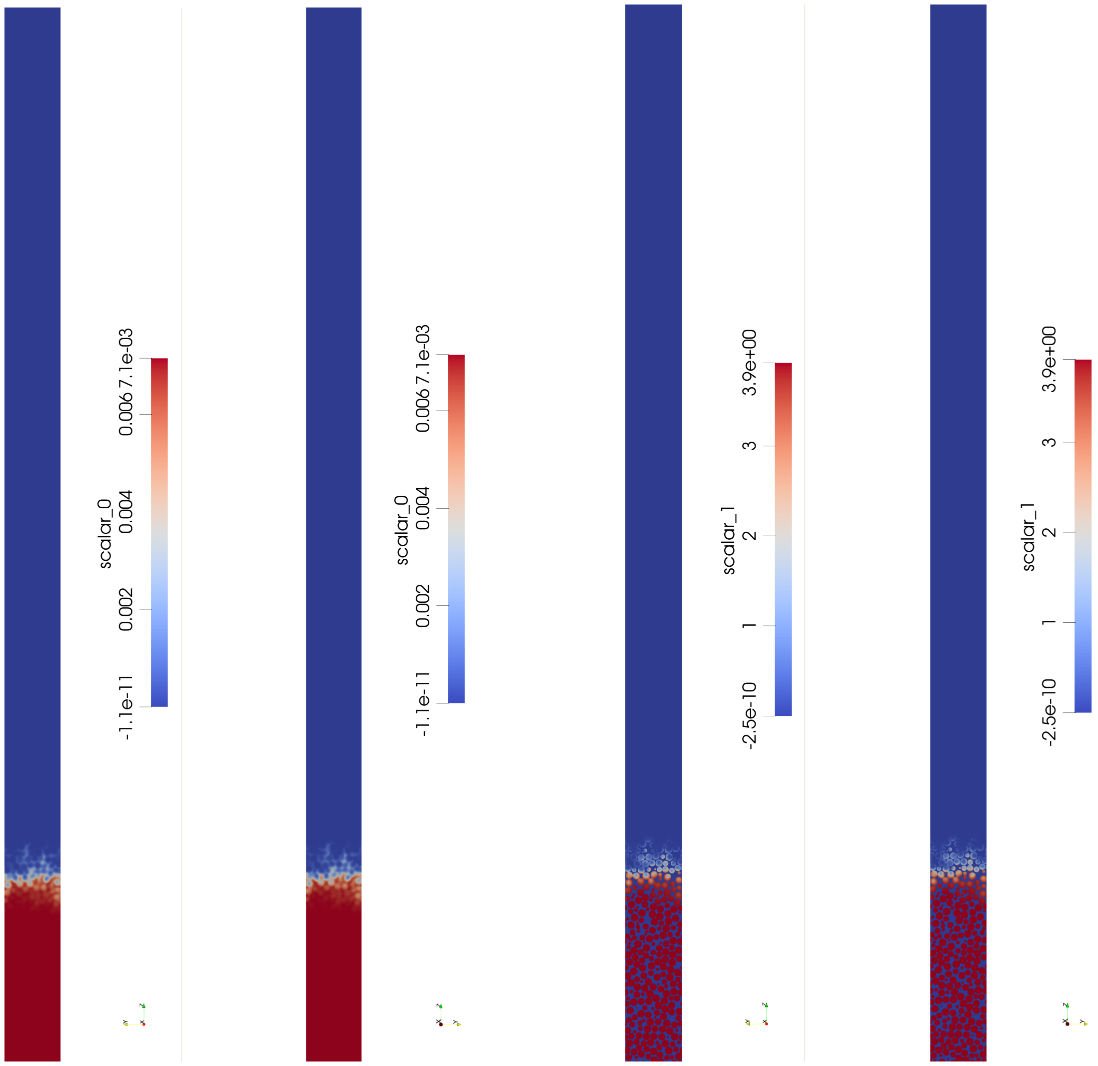

(a) Liquid concentration at $t \approx 11000s$ **(b)** Solid concentration at $t \approx 11000s$

Figure 8.12: Concentration profiles of liquid and solid phases on periodic boundaries at $t \approx 11000s$ in the large monodisperse column

These simulations were not able to achieve full breakthrough. Upon further examination, it was observed that they were affected by a severe and progressive loss in axial flowrate along the column length. This is shown in Figure 8.13.

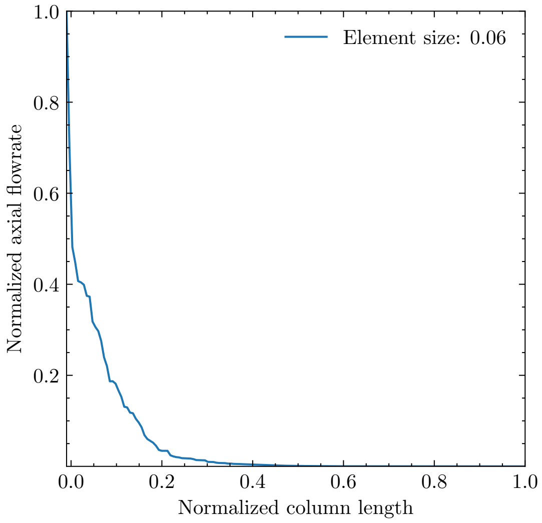

Figure 8.13: Loss of axial flowrate along column length in long column with 10,000 particles.

Volume flux conservation

Simulations with double-periodic boundary conditions showed progressive loss in volume flux (axial flowrate) along the column length. For the short column test case, the volume flux in the flow simulation is averaged across the cross-section area, and plotted along the column length as shown in Figure 8.14a. The axial flowrate is observed to be significantly reduced along the column length. The same test case was subjected to single-periodicity along the x and y directions separately. Results, shown in Figure 8.14b, indicate proper conservation of volume flux, outside those limitations imposed by numerical errors originating from inadequate boundary layer resolution within the packed-bed region.

This suggests an issue with handling double-periodic boundary conditions. Upon further investigation, it is clear that results at edges of the domain geometry, where two surfaces of periodicity overlap, were not periodic for the y-component of the velocity. This is shown for the short column simulation in Figure 8.15. As XNS is currently only able to handle one-to-one nodal correspondence for periodic boundary conditions, periodicity at the corner nodes is only applied in one direction, leading to inconsistent solutions and loss of conservation.

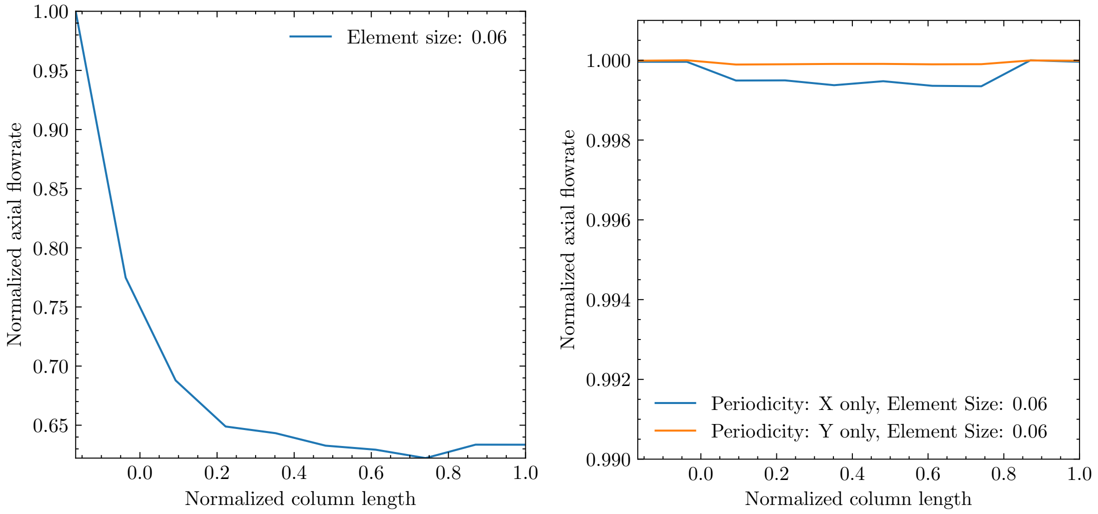

(a) Application of double periodicity results in a drop in axial flowrate.

(b) Single periodicity applied individually results in no substantial drop in flowrate.

Figure 8.14: Normalized axial flowrates along column length for short column case with double and single periodicity applied.

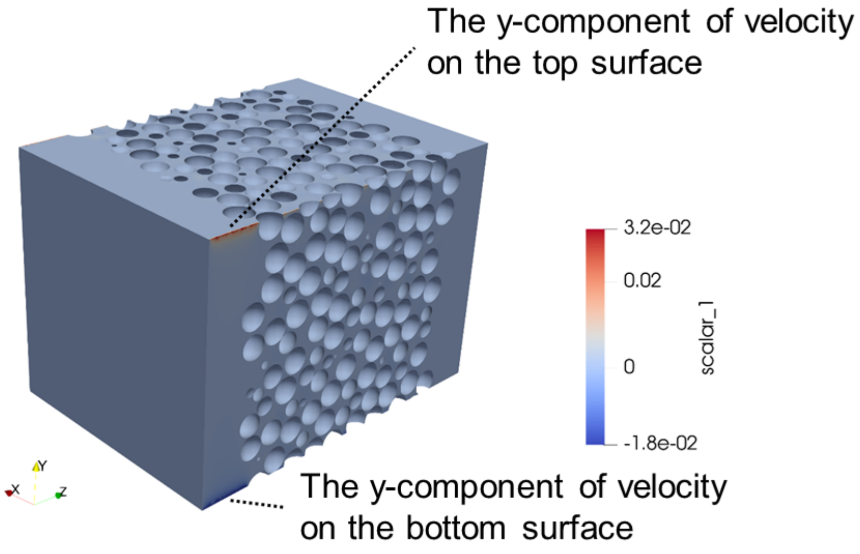

Figure 8.15: Non-periodic behavior of the y-component of velocity at corners with double-periodicity.

8.4 Conclusions and outlook

High-definition simulation infrastructure was updated to handle simulations with periodic boundary conditions. Periodic packings were generated using the open-source `packing-generation` tool. The mesh generation tool, `pymesh`, was updated to handle periodic geometries and meshes. Finally, the implementation of periodic boundary conditions in XNS was updated for this work.

Simulations of small and large-scale columns consisting of 1000 and 10 000 particles respectively with double-periodic boundary conditions were conducted. While the handling of double-periodicity in XNS requires further work, preliminary simulations show great potential for simulating unconfined columns without wall effects. Simulations of otherwise identical confined and unconfined columns for monodisperse and polydisperse cases could be used in the calibration of ROMs, leading to isolation of the effects of particle size distribution and wall effects on the column dispersion and film-diffusion coefficients.

Summary, conclusions, and outlook 9

In this chapter, work done during the course of this project is summarized, conclusions are drawn, and potential future work is explored.

9.1 Summary

Improvements in high-definition simulation accuracy were achieved through multi-faceted enhancements in geometry, meshes, and numerical methods.

Local and global contact-point modeling techniques such as capping, bridging, and reduction were implemented and tested. Although local modifications to contact points resulted in improved element quality near contact point regions, their effect on simulation results were not substantial enough to justify their computational cost and increased chance of failure in mesh generation. Ultimately, global particle size reduction by a negligible amount of 0.03 % (compared to the previously used 2 %) was applied to all geometries in this work, essentially the lowest amount permitted by numerical precision to avoid numerical overlap of particles. As global reduction maintained particle shapes, a new mesh generation strategy was developed that exploited the geometric similarity in all particles of the packed bed. Whereas in the original method, meshes are generated for every individual entity, the new method copied a reference mesh onto all the particles of the bed, resulting in speedup by a factor of 10.

The so-called metric stabilization method was applied, leading to substantial reduction in the generalized holdup volume error by up to a factor of up to 3. This method calculates the finite element stabilization factor by taking into account the contravariant metric tensor of the given element, providing robust and accurate stabilization to deformed elements.

Small and large scale simulations of loading with approximately 1000 and 10 000 particles were conducted with both monodisperse and polydisperse packings. Hotspots in the flow field were visualized and analyzed for a range of mesh element sizes. The resulting data showed higher sensitivity to element sizes in regions with lower velocities, such as near particle walls. As velocity peaks are confined to a very small portion of the interstitial volume, improvements in meshes in these regions showed no substantial benefit. Consequently, new meshes were generated with highly refined element sizes near particle and wall surfaces. For short column simulations, anisotropic meshes resulted in 54.90 %

and 65.20 % reductions in the number of elements in the interstitial and particle domains respectively when compared to the finest uniform mesh. The generalized holdup volume error in these cases was reduced to 3 %. In simulations of large-scale columns with uniform meshes, an error of 8 % was observed. These results could be further improved with the application of anisotropic meshes.

High-definition simulation infrastructure was updated with a focus on robustness, interoperability, scalability, and support for potential future requirements. The newly-developed packed-bed chromatography column meshing tool is able to mesh confined and unconfined (periodic) geometries using high-level meshing methods that offer order-of-magnitude speedups and reduced resource utilization, providing a basis for scalability for future geometries. With built-in support for anisotropic meshes, inlet surface splitting, second-order meshes, and triple-periodicity, this tool is readily applicable for future simulations, without substantial modifications. The post-processing stage of the workflow was also updated to use distributed parallelism using MPI. Several other tools were parallelized to support shorter wait times between simulation deployments.

Reduced-order models of packed-bed liquid chromatography, specifically 1D and 2D general rate models, were calibrated using a novel multi-objective optimization framework. The internal states of the column, i.e., masses in bulk, particle pore, and solid phases, were used as objective metrics and reference data to estimate coefficients of axial and radial dispersions, and thin-film diffusion. HD simulation results were appropriately reduced, i.e., averaged, to generate reference data for the calibration. Results showed that neglecting particle sized distribution can have adverse effects on the calibration of ROMs, with the film diffusion coefficient reducing in value by 37 % in the ROM without PSD. Results show exceptional fits for the polydisperse packing, whereas some discrepancy in fit was observed for the monodisperse packing. This is attributed to the fact that the given monodisperse packing still exhibits substantial oscillation in porosity caused by geometric wall effects even at the center of the column, whereas the oscillations in the polydisperse case are damped quicker. Such thin columns violate assumptions of homogeneity inherent in reduced-order models, leading to incompatibilities between the ROM and HD model that drive minor discrepancies in the fit. Nonetheless, the use of internal solute masses was shown to be not only useful, but, in the case of 2D GRM, also necessary in calibrating ROMs. With future improvements in HD simulation infrastructure leading to simulations of unconfined packings without wall effects, this method of calibration will enable the resolution of the various geometric and phenomenological causes of dispersion by calibration and comparison with an array of reference HD simulations.

Groundwork for simulating columns with unconfined packings via periodic boundary conditions was set up. The HD simulation toolchain and workflow were adapted to work with laterally double-periodic (i.e., xy-periodic) geometries and meshes. Validation and testing strategies were developed to ensure correctness at every stage. The chromatography module in XNS itself was updated to work with single periodicity in a given direction. Implementing double-periodicity, however, is still pending, and will be pursued in the continuation of this project. The resulting unconfined periodic HD simulations shown in this work are, in effect, non-conservative due to this inability of the current system to handle double-periodic boundary conditions. They are, nevertheless, already insightful in a qualitative manner. Transport-adsorption simulation results show a uniformly progressing concentration front as opposed to the inverted parabolic profile seen in the previous thin, confined-packing simulations due to wall effects. Such a front still shows tortuousity at the inter-particle scale, resulting in varied gradients around the particle surfaces that lead to asymmetric loading. A comprehensive analysis of this phenomenon is deferred until after the implementation of double-periodicity.

9.2 Conclusions and Outlook

This work advances the state-of-the-art in high-definition simulation of packed-bed chromatography by reducing simulation error through the use of accurate model geometry, targeted anisotropic meshes based on analysis, and improved stabilization methods. The efficacy of high-definition simulations was demonstrated through development and successful application of a novel reduced-order model calibration workflow, which used the column's internal state obtained from HD simulation results as reference data. This workflow was successfully applied to 2D GRM, which presents difficulty in calibration due to the radial resolution of parameters and objectives. Substantial progress was also made towards the simulation of wider columns using periodic boundary conditions, with the implementation of periodic mesh generation and several validation strategies showcased in this work. Shortcomings in the existing implementation of periodicity in XNS have been identified. Proper implementation of double-periodicity is considered out of scope of this work, and will be addressed in the continuation of this project. Nevertheless, even in the absence of double-periodicity, preliminary results of periodic simulations show huge potential in resolving the effects of geometric wall effects on column dispersion coefficients when used in conjunction with simulations of confined packings and the new ROM calibration setup.

In future work, complexity of the simulated chromatography process can be increased in several ways to model realistic situations with multi-component separation. Complex binding models such as the Steric Mass Action model, that are already implemented in the XNS solver, could be applied to simulate ionic binding with steric hindrances. Surface diffusion and reactions can also be incorporated if necessary.

Another aspect of realistic simulations in packed-bed chromatography involves properly modeling sample injection only at the center of the inlet. Such a scenario can be easily simulated with no further modifications with the current toolchain.

Confined HD simulations of chromatography can presently be conducted for approximately 10 000-15 000 particles. Future improvements in the parallelism and performance of the solver using hybrid parallelism, GPU acceleration, and additive schwarz decomposition techniques promise scalability up to realistic column sizes. In such a scenario, it would also be ideal to generate the packing geometry from 3D imaging techniques applied to experimental columns. This would also pave the way for studies on the effects various packing techniques and packing defects such as channels and low-density regions. While 3D imaging techniques naturally pair with HD simulations, they are crucial with regards to generating CAD geometries for monolithic stationary phases.

With HD simulations of unconfined packings using double-periodicity, it will be possible to isolate the effects of wall-effects for a given geometry and particle size distribution on the column dispersion coefficients (axial and radial), and film diffusion coefficient. Columns with identical PSD, bed lengths, can be separately simulated using confined and unconfined geometries, and used to independently calibrate two separate instances of GRM, either 1D or 2D. With all other model parameters being equal, assuming no violation of the homogeneity assumptions in ROMs, the disparity in the calibrated model coefficients must be due to wall effects.

Another avenue of future work that is especially viable for loading simulations is triple-periodicity, i.e., periodicity in all three spatial directions. A toy geometry is provided in Figure 9.1 as an example, which shows the inlet, core, and outlet regions decomposed.

In simulations of single-component loading of unconfined columns, the region of prime interest is the concentration front and its vicinity. As the front progresses linearly along the column axis, a majority of the computational domain is of no interest. Such loading simulations could be vastly sped up by repeatedly simulating only a small region around the concentration front. This could be possible with such a triply-periodic setup, where, after initial simulation in the inlet region, the concentration front is repeatedly simulated in a series of translated core region compartments until the desired bed length is achieved. This is depicted in Figure 9.2. The breakthrough curve can be obtained by finally connecting the outlet region to the end of the core region.

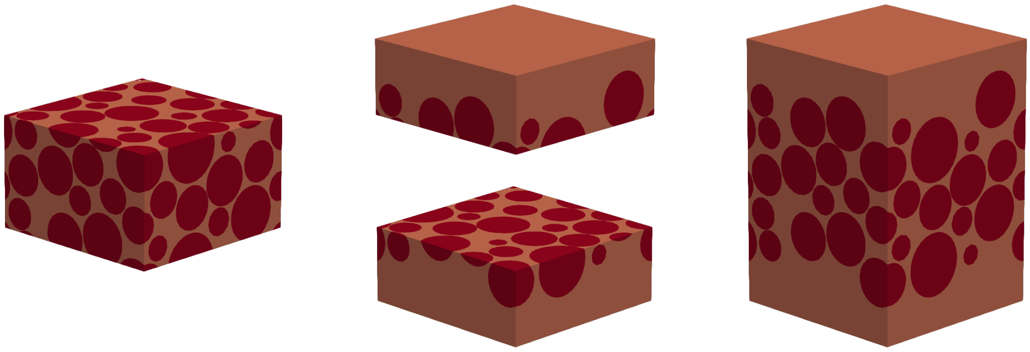

(a) Core **(b)** Inlet and outlet **(c)** Full column

Figure 9.1: Axially and laterally periodic packing compartmentalized into inlet, core, and outlet regions.

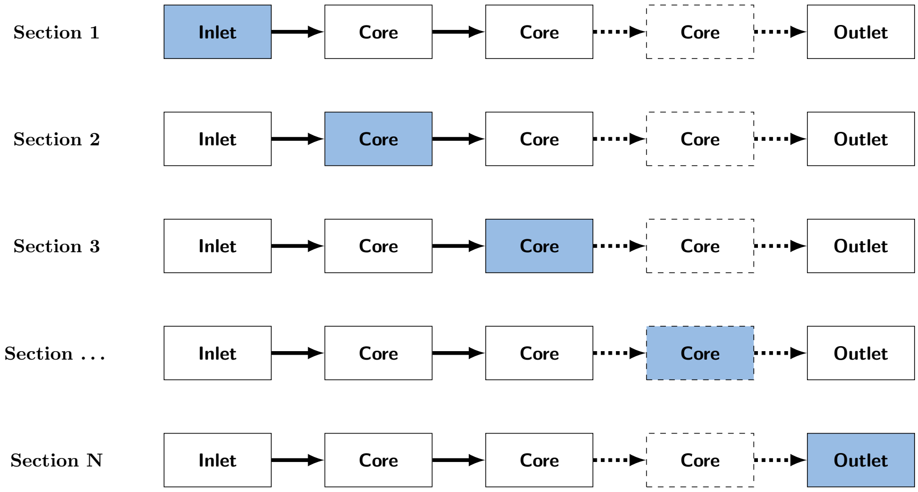

Figure 9.2: Serial connectivity of compartmentalized triple-periodic system. Column loading simulation is divided in to sections, with only the highlighted compartment actively simulated in the given section.

Triple-periodic meshes are already supported by the mesh generator, and rudimentary external tools for boundary coupling have also been developed. However, the instrumentation of such a system requires further effort in order to simulate longer columns in a consistent manner. Testing and validation of boundary coupling mechanisms between regions is currently pending. Nevertheless, this technique holds promise for lowering the cost of high-definition simulations, potentially enabling their deployment on smaller workstations without compromising dimensional accuracy.

Bibliography

[1] Jayghosh Subodh Rao et al. 'High-definition simulation of packed-bed liquid chromatography'. In: *Computers & Chemical Engineering* 178 (2023), p. 108355. DOI: `https://doi.org/10.1016/j.compchemeng.2023.108355` (cited on page xvii).

[2] Jayghosh Subodh Rao et al. 'Two-dimensional general rate model with particle size distribution in CADET calibrated with high-definition CFD simulated intra-column data'. In: *Separation and Purification Technology* 379 (2025), p. 134409. DOI: `https://doi.org/10.1016/j.seppur.2025.134409` (cited on page xvii).

[3] Jayghosh Rao. *cadet/CADET-HD-pymesh: v1.0.0*. Version v1.0.0. June 2025. DOI: `10.5281/zenodo.15579995` (cited on page xvii).

[4] Jayghosh Rao. *cadet/CADET-HD-chromoo: v1.0.0*. Version v1.0.0. June 2025. DOI: `10.5281/zenodo.15580015` (cited on page xvii).

[5] Jayghosh Rao. *cadet/CADET-HD-paravision: v1.0.0*. Version v1.0.0. June 2025. DOI: `10.5281/zenodo.15580000` (cited on page xvii).

[6] Jayghosh Rao. *cadet/CADET-HD-mixdtools: v1.0.0*. Version v1.0.0. June 2025. DOI: `10.5281/zenodo.15579993` (cited on page xvii).

[7] Jayghosh Rao. *cadet/CADET-HD-genmesh: v1.0.0*. Version v1.0.0. June 2025. DOI: `10.5281/zenodo.15579985` (cited on page xvii).

[8] Jayghosh Rao. *cadet/CADET-HD-scripts: v1.0.0*. Version v1.0.0. June 2025. DOI: `10.5281/zenodo.15580004` (cited on page xvii).

[9] G. Guiochon et al. *Fundamentals of Preparative and Nonlinear Chromatography*. Second. Amsterdam: Elsevier Academic Press, 2006 (cited on pages 4, 83).

[10] M.D. Mantle, A.J. Sederman, and L.F. Gladden. 'Single- and two-phase flow in fixed-bed reactors: MRI flow visualisation and lattice-Boltzmann simulations'. In: *Chemical Engineering Science* 56.2 (Jan. 2001), pp. 523–529. DOI: `10.1016/s0009-2509(00)00256-6` (cited on page 5).

[11] Magnus Schröder, Eric Von Lieres, and Jü rgen Hubbuch. 'Direct quantification of intraparticle protein diffusion in chromatographic media'. In: *The Journal of Physical Chemistry B* 110.3 (2006), pp. 1429–1436 (cited on page 5).

[12] S.P. Sullivan et al. 'Simulation of packed bed reactors using lattice Boltzmann methods'. In: *Chemical Engineering Science* 60.12 (June 2005), pp. 3405–3418. DOI: `10.1016/j.ces.2005.01.038` (cited on page 5).

[13] Dzmitry Hlushkou, Stefan Bruns, and Ulrich Tallarek. 'High-performance computing of flow and transport in physically reconstructed silica monoliths'. In: *Journal of Chromatography A* 1217.23 (June 2010), pp. 3674–3682. DOI: `10.1016/j.chroma.2010.04.004` (cited on page 5).

[14] Dzmitry Hlushkou et al. 'Morphology-transport relationships for silica monoliths: From physical reconstruction to pore-scale simulations'. In: *Journal of Separation Science* 34.16-17 (June 2011), pp. 2026–2037. DOI: `10.1002/jssc.201100158` (cited on page 5).

[15] Dzmitry Hlushkou and Ulrich Tallarek. 'Analysis of microstructure–effective diffusivity relationships for the interparticle pore space in physically reconstructed packed beds'. In: *Journal of Chromatography A* 1581-1582 (Dec. 2018), pp. 173–179. DOI: `10.1016/j.chroma.2018.11.003` (cited on page 5).

[16] Anders Ljunglöf and Rolf Hjorth. 'Confocal microscopy as a tool for studying protein adsorption to chromatographic matrices'. In: *Journal of Chromatography A* 743.1 (Aug. 1996), pp. 75–83. DOI: `10.1016/0021-9673(96)00290-7` (cited on page 5).

[17] Anders Ljunglöf and Jörg Thömmes. 'Visualising intraparticle protein transport in porous adsorbents by confocal microscopy'. In: *Journal of Chromatography A* 813.2 (July 1998), pp. 387–395. DOI: `10.1016/s0021-9673(98)00378-1` (cited on page 5).

[18] Jürgen Hubbuch et al. 'Dynamics of protein uptake within the adsorbent particle during packed bed chromatography'. In: *Biotechnology and Bioengineering* 80.4 (Sept. 2002), pp. 359–368. DOI: `10.1002/bit.10500` (cited on page 5).

[19] S. R. Dziennik et al. 'Nondiffusive mechanisms enhance protein uptake rates in ion exchange particles'. In: *Proceedings of the National Academy of Sciences* 100.2 (Jan. 2003), pp. 420–425. DOI: `10.1073/pnas.0237084100` (cited on page 5).

[20] Jürgen Hubbuch et al. 'Mechanism and kinetics of protein transport in chromatographic media studied by confocal laser scanning microscopy'. In: *Journal of Chromatography A* 1021.1–2 (Dec. 2003), pp. 105–115. DOI: `10.1016/j.chroma.2003.08.092` (cited on page 5).

[21] Kun Yang, Qing-Hong Shi, and Yan Sun. 'Modeling and simulation of protein uptake in cation exchanger visualized by confocal laser scanning microscopy'. In: *Journal of Chromatography A* 1136.1 (Dec. 2006), pp. 19–28. DOI: `10.1016/j.chroma.2006.09.036` (cited on page 5).

[22] Kun Yang, Shu Bai, and Yan Sun. 'Protein adsorption dynamics in cation-exchange chromatography quantitatively studied by confocal laser scanning microscopy'. In: *Chemical Engineering Science* 63.16 (Aug. 2008), pp. 4045–4054. DOI: `10.1016/j.ces.2008.05.013` (cited on page 5).

[23] Guofeng Zhao et al. 'Analysis of hydrophobic charge induction displacement chromatography by visualization with confocal laser scanning microscopy'. In: *Separation and Purification Technology* 82 (Oct. 2011), pp. 138–147. DOI: `10.1016/j.seppur.2011.09.002` (cited on page 5).

[24] S.S. Bu et al. 'On contact point modifications for forced convective heat transfer analysis in a structured packed bed of spheres'. In: *Nuclear Engineering and Design* 270 (Apr. 2014), pp. 21–33. DOI: `10.1016/j.nucengdes.2014.01.001` (cited on page 5).

[25] G. M. Karthik and Vivek V. Buwa. 'Effect of particle shape on fluid flow and heat transfer for methane steam reforming reactions in a packed bed'. In: *AIChE Journal* 63.1 (Oct. 2016), pp. 366–377. DOI: `10.1002/aic.15542` (cited on page 5).

[26] Dmitry Pashchenko, Igor Karpilov, and Ravil Mustafin. 'Numerical calculation with experimental validation of pressure drop in a fixed-bed reactor filled with the porous elements'. In: *AIChE Journal* 66.5 (Feb. 2020). DOI: `10.1002/aic.16937` (cited on page 5).

[27] Sebastian Schnittert, Remo Winz, and Eric von Lieres. 'Development of a 3D Model for Packed Bed Liquid Chromatography in Micro-columns'. In: *2009 Third UKSim European Symposium on Computer Modeling and Simulation* (Nov. 2009). DOI: `10.1109/ems.2009.62` (cited on page 5).

[28] Spyridon Gerontas, Michael S. Shapiro, and Daniel G. Bracewell. 'Chromatography modelling to describe protein adsorption at bead level'. In: *Journal of Chromatography A* 1284 (Apr. 2013), pp. 44–52. DOI: `10.1016/j.chroma.2013.01.102` (cited on page 5).

[29] Long Li et al. 'Computational Study of Chromatography Performance in Ordered Packed Beds with Spherical or Ellipsoidal Particles'. In: *Energy Procedia* 75 (Aug. 2015), pp. 3322–3327. DOI: `10.1016/j.egypro.2015.07.719` (cited on page 5).

[30] Long Li et al. 'Numerical investigation on band-broadening characteristics of an ordered packed bed with novel particles'. In: *Applied Energy* 185 (Jan. 2017), pp. 2168–2180. DOI: `10.1016/j.apenergy.2016.03.045` (cited on page 5).

[31] T. Eppinger, K. Seidler, and M. Kraume. 'DEM-CFD simulations of fixed bed reactors with small tube to particle diameter ratios'. In: *Chemical Engineering Journal* 166.1 (Jan. 2011), pp. 324–331. DOI: `10.1016/j.cej.2010.10.053` (cited on page 5).

[32] Nico Zobel et al. 'Influence of the wall structure on the void fraction distribution in packed beds'. In: *Chemical Engineering Science* 71 (Mar. 2012), pp. 212–219. DOI: `10.1016/j.ces.2011.12.029` (cited on page 5).

[33] Gregor D. Wehinger, Thomas Eppinger, and Matthias Kraume. 'Detailed numerical simulations of catalytic fixed-bed reactors: Heterogeneous dry reforming of methane'. In: *Chemical Engineering Science* 122 (Jan. 2015), pp. 197–209. DOI: `10.1016/j.ces.2014.09.007` (cited on page 5).

[34] Gregor D. Wehinger, Carsten Fütterer, and Matthias Kraume. 'Contact Modifications for CFD Simulations of Fixed-Bed Reactors: Cylindrical Particles'. In: *Industrial & Engineering Chemistry Research* 56.1 (Dec. 2016), pp. 87–99. DOI: `10.1021/acs.iecr.6b03596` (cited on page 5).

[35] Thomas Eppinger and Gregor D. Wehinger. 'A Generalized Contact Modification for Fixed-Bed Reactor CFD Simulations'. In: *Chemie Ingenieur Technik* (Dec. 2020). DOI: `10.1002/cite.202000182` (cited on page 5).

[36] Siarhei Khirevich et al. 'Impact of Conduit Geometry and Bed Porosity on Flow and Dispersion in Noncylindrical Sphere Packings'. In: *Analytical Chemistry* 79.24 (Dec. 2007), pp. 9340–9349. DOI: `10.1021/ac071428k` (cited on page 5).

[37] Ferdaous Dorai et al. 'Fully resolved simulations of the flow through a packed bed of cylinders: Effect of size distribution'. In: *Chemical Engineering Science* 129 (June 2015), pp. 180–192. DOI: `10.1016/j.ces.2015.01.070` (cited on page 5).

[38] Nico Jurtz, Matthias Kraume, and Gregor D. Wehinger. 'Advances in fixed-bed reactor modeling using particle-resolved computational fluid dynamics (CFD)'. In: *Reviews in Chemical Engineering* 35.2 (Feb. 2019), pp. 139–190. DOI: `10.1515/revce-2017-0059` (cited on page 5).

[39] Anthony G. Dixon, Michiel Nijemeisland, and E. Hugh Stitt. 'Packed Tubular Reactor Modeling and Catalyst Design using Computational Fluid Dynamics'. In: *Advances in Chemical Engineering* (2006), pp. 307–389. DOI: `10.1016/s0065-2377(06)31005-8` (cited on page 5).

[40] Andreas Püttmann et al. 'Stabilized space–time finite elements for high-definition simulation of packed bed chromatography'. English. In: *Finite Elements in Analysis and Design* 86.C (2014), pp. 1–11. DOI: `10.1016/j.finel.2014.03.001` (cited on page 6).

[41] Andreas Püttmann. *High Performance Finite Element Methods for Three-Dimensional Chromatography Models*. Berichte aus der Verfahrenstechnik. Aachen: Shaker Verlag, 2015 (cited on page 6).

[42] P.V. Danckwerts. 'Continuous flow systems: Distribution of residence times'. In: *Chemical Engineering Science* 2.1 (1953), pp. 1–13. DOI: `10.1016/0009-2509(53)80001-1` (cited on page 16).

[43] Shamsul Qamar et al. 'Analysis of linear two-dimensional general rate model for chromatographic columns of cylindrical geometry'. In: *Journal of Chromatography A* 1496 (2017), pp. 92–104. DOI: `10.1016/j.chroma.2017.03.048` (cited on page 18).

[44] Y. Saad and M. H. Schultz. *GMRES: A Generalized Minimal Residual Algorithm for Solving Nonsymmetric Linear Systems*. 1986. DOI: `10.1137/0907058` (cited on page 23).

[45] Y. Saad. *A Flexible Inner-Outer Preconditioned GMRES Algorithm*. 1993. DOI: `10.1137/0914028` (cited on page 23).

[46] Lutz Pauli. *Stabilized Finite Element Methods for Computational Design of Blood-Handling Devices*. July 2016 (cited on pages 25, 27).

[47] Gary E. Mueller. 'Numerically packing spheres in cylinders'. In: *Powder Technology* 159.2 (Nov. 2005), pp. 105–110. DOI: `10.1016/j.powtec.2005.06.002` (cited on page 32).

[48] Eduardo M. B. Campello and Kamila R. Cassares. 'Rapid Generation of Particle Packs at High Packing Ratios for DEM Simulations of Granular Compacts'. In: *Latin American Journal of Solids and Structures* 13.1 (Jan. 2016), pp. 23–50. DOI: `10.1590/1679-78251694` (cited on page 32).

[49] Maciej Marek. 'Numerical modeling of random packed beds of various packing densities with a sequential deposition algorithm'. In: *AIP Conference Proceedings*. Vol. 2078. Author(s), 2019, p. 020015. DOI: `10.1063/1.5092018` (cited on page 32).

[50] J. Mościński et al. 'The Force-Biased Algorithm for the Irregular Close Packing of Equal Hard Spheres'. In: *Molecular Simulation* 3.4 (May 1989), pp. 201–212. DOI: `10.1080/08927028908031373` (cited on pages 32, 89).

[51] Boris D Lubachevsky and Frank H Stillinger. 'Geometric properties of random disk packings'. In: *Journal of statistical Physics* 60 (1990), pp. 561–583 (cited on pages 32, 89).

[52] W. S. Jodrey and E. M. Tory. 'Computer simulation of close random packing of equal spheres'. In: *Physical Review A* 32.4 (Oct. 1985), pp. 2347–2351. DOI: `10.1103/physreva.32.2347` (cited on page 32).

[53] W.I. Salvat et al. 'An algorithm to simulate packing structure in cylindrical containers'. In: *Catalysis Today* 107–108 (Oct. 2005), pp. 513–519. DOI: `10.1016/j.cattod.2005.07.108` (cited on page 32).

[54] Elyas M. Moghaddam et al. 'Rigid Body Dynamics Algorithm for Modeling Random Packing Structures of Nonspherical and Nonconvex Pellets'. In: *Industrial &; Engineering Chemistry Research* 57.44 (Oct. 2018), pp. 14988–15007. DOI: `10.1021/acs.iecr.8b03915` (cited on page 32).

[55] K. Han, Y.T. Feng, and D.R.J. Owen. 'Sphere packing with a geometric based compression algorithm'. In: *Powder Technology* 155.1 (July 2005), pp. 33–41. doi: `10.1016/j.powtec.2005.04.055` (cited on page 32).

[56] Jean-François Jerier et al. 'A geometric algorithm based on tetrahedral meshes to generate a dense polydisperse sphere packing'. In: *Granular Matter* 11.1 (Oct. 2008), pp. 43–52. doi: `10.1007/s10035-008-0116-0` (cited on page 32).

[57] Jean-François Jerier et al. 'Packing spherical discrete elements for large scale simulations'. In: *Computer Methods in Applied Mechanics and Engineering* 199.25–28 (May 2010), pp. 1668–1676. doi: `10.1016/j.cma.2010.01.016` (cited on page 32).

[58] S. Torquato and F. H. Stillinger. 'Jammed hard-particle packings: From Kepler to Bernal and beyond'. In: *Reviews of Modern Physics* 82.3 (Sept. 2010), pp. 2633–2672. doi: `10.1103/revmodphys.82.2633` (cited on page 32).

[59] N. Chernov, Yu. Stoyan, and T. Romanova. 'Mathematical model and efficient algorithms for object packing problem'. In: *Computational Geometry* 43.5 (July 2010), pp. 535–553. doi: `10.1016/j.comgeo.2009.12.003` (cited on page 32).

[60] G. A. Georgalli and M. A. Reuter. 'A particle packing algorithm for packed beds with size distribution'. In: *Granular Matter* 10.4 (Mar. 2008), pp. 257–262. doi: `10.1007/s10035-008-0097-z` (cited on page 32).

[61] Mhand Hifi, Amir Mohamed-Youssouf, and Labib Yousef. 'A threshold search-based population algorithm for the sphere packing problem'. In: *Knowledge-Based Systems* 261 (Feb. 2023), p. 110177. doi: `10.1016/j.knosys.2022.110177` (cited on page 32).

[62] R. Caulkin et al. 'An investigation of packed columns using a digital packing algorithm'. In: *Computers &; Chemical Engineering* 30.6–7 (May 2006), pp. 1178–1188. doi: `10.1016/j.compchemeng.2006.02.019` (cited on page 32).

[63] S. Khirevich et al. 'Impact of conduit geometry and bed porosity on flow and dispersion in noncylindrical sphere packings.' In: *Analytical chemistry* 79.24 (2007), pp. 9340–9349. doi: `10.1021/ac071428k` (cited on page 32).

[64] R. Montesinos et al. 'Analysis and simulation of frontal affinity chromatography of proteins'. In: *Separation and Purification Technology* 42.1 (2005), pp. 75–84. doi: `10.1016/j.seppur.2004.03.014` (cited on pages 32, 48).

[65] George Karypis. 'METIS and ParMETIS'. In: *Encyclopedia of Parallel Computing*. Ed. by David Padua. Boston, MA: Springer US, 2011, pp. 1117–1124. doi: `10.1007/978-0-387-09766-4_500` (cited on page 40).

[66] C. Chevalier and F. Pellegrini. 'PT-SCOTCH: a tool for efficient parallel graph ordering.' In: *Parallel Computing* 34 (2008), pp. 318–331 (cited on page 40).

[67] Giorgio Carta and Antonio Ubiera. 'Particle-size distribution effects in batch adsorption'. In: *AIChE Journal* 49.12 (2003), pp. 3066–3073. DOI: `10.1002/aic.690491208` (cited on page 47).

[68] J.J. van Deemter, F.J. Zuiderweg, and A. Klinkenberg. 'Longitudinal diffusion and resistance to mass transfer as causes of nonideality in chromatography'. In: *Chemical Engineering Science* 5.6 (Sept. 1956), pp. 271–289. DOI: `10.1016/0009-2509(56)80003-1` (cited on page 63).

[69] K. Deb et al. 'A fast and elitist multiobjective genetic algorithm: NSGA-II'. In: *IEEE Transactions on Evolutionary Computation* 6.2 (Apr. 2002), pp. 182–197. DOI: `10.1109/4235.996017` (cited on page 74).

[70] Kalyanmoy Deb and Himanshu Jain. 'An Evolutionary Many-Objective Optimization Algorithm Using Reference-Point-Based Nondominated Sorting Approach, Part I: Solving Problems With Box Constraints'. In: *IEEE Transactions on Evolutionary Computation* 18.4 (Aug. 2014), pp. 577–601. DOI: `10.1109/tevc.2013.2281535` (cited on page 74).

[71] Haitham Seada and Kalyanmoy Deb. 'A Unified Evolutionary Optimization Procedure for Single, Multiple, and Many Objectives'. In: *IEEE Transactions on Evolutionary Computation* 20.3 (June 2016), pp. 358–369. DOI: `10.1109/tevc.2015.2459718` (cited on page 74).

[72] Julian Blank et al. 'Generating Well-Spaced Points on a Unit Simplex for Evolutionary Many-Objective Optimization'. In: *IEEE Transactions on Evolutionary Computation* 25.1 (2021), pp. 48–60. DOI: `10.1109/TEVC.2020.2992387` (cited on page 74).

[73] Kalyanmoy Deb, Karthik Sindhya, and Tatsuya Okabe. 'Self-adaptive simulated binary crossover for real-parameter optimization'. In: *Proceedings of the 9th Annual Conference on Genetic and Evolutionary Computation*. GECCO '07. London, England: Association for Computing Machinery, 2007, pp. 1187–1194. DOI: `10.1145/1276958.1277190` (cited on page 75).

[74] Waqas Haider Bangyal et al. 'Comparative Analysis of Low Discrepancy Sequence-Based Initialization Approaches Using Population-Based Algorithms for Solving the Global Optimization Problems'. In: *Applied Sciences* 11.16 (Aug. 2021), p. 7591. DOI: `10.3390/app11167591` (cited on page 75).

[75] Vasili Baranau and Ulrich Tallarek. 'Random-close packing limits for monodisperse and polydisperse hard spheres'. In: *Soft Matter* 10.21 (2014), p. 3826. DOI: `10.1039/c3sm52959b` (cited on pages 88, 89).